INTERFACIAL ELECTROCHEMISTRY OF CU/AL ALLOYS FOR IC PACKAGING AND CHEMICAL BONDING CHARACTERIZATION OF BORON DOPED HYDROGENATED AMORPHOUS SILICON FILMS FOR INFRARED CAMERAS

Nick Ross, B.A.

Dissertation Prepared for the Degree of

DOCTOR OF PHILOSOPHY

UNIVERSITY OF NORTH TEXAS

May 2016

APPROVED:

Oliver M. R. Chyan, Major Professor
Teresa D. Golden, Committee Member
William E. Acree, Jr., Committee Member
Mohammad Omary, Committee Member
Michael Richmond, Chair of the Department of Chemistry
Costas Tsatsoulis, Dean of the Toulouse Graduate School

Ross, Nick. *Interfacial Electrochemistry of CU/AL Alloys for IC Packaging and Chemical Bonding Characterization of Boron Doped Hydrogenated Amorphous Silicon Films for Infrared Cameras.* Doctor of Philosophy (Chemistry-Analytical Chemistry), May 2016, 141 pp., 3 tables, 69 figures, references, 20 titles.

We focused on a non-cooling room temperature microbolometer infrared imaging array device which includes a sensing layer of p-type *a*-Si:H component layers doped with boron. Boron incorporation and bonding configuration were investigated for *a*-Si:H films grown by plasma enhanced chemical deposition (PECVD) at varying substrate temperatures, hydrogen dilution of the silane precursor, and dopant to silane ratio using multiple internal reflection infrared spectroscopy (MIR-IR). This study was then confirmed from collaborators via Raman spectroscopy. MIR-IR analyses reveal an interesting counter-balance relationship between boron-doping and hydrogen-dilution growth parameters in PECVD-grown *a*-Si:H. Specifically, an increase in the hydrogen dilution ratio (H_2/SiH_4) or substrate temperature was found to increase organization of the silicon lattice in the amorphous films. It resulted in the decrease of the most stable SiH bonding configuration and thus decrease the organization of the film. The new chemical bonding information of *a*-Si:H thin film was correlated with the various boron doping mechanisms proposed by theoretical calculations. The study revealed the corrosion morphology progression on aluminum alloy (Al, 0.5% Cu) under acidic chloride solution. This is due to defects and a higher copper content at the grain boundary. Direct galvanic current measurement, linear sweep voltammetry (LSV), and Tafel plots are used to measure corrosion current and potential. Hydrogen gas evolution was also observed (for the first time) in Cu/Al bimetallic interface in areas of active corrosion. Mechanistic insight that leads to effective prevention of aluminum bond pad corrosion is explored and discussed.

Copyright 2016

by

Nick Ross

ACKNOWLEDGEMENTS

First, I would like to thank God, whose many blessings have made me who I am today. Secondly, I am truly appreciative of all the people in my life that have invested their time, wisdom, and love in my journey thus far. This dissertation is the result of a group effort in my academic and professional upbringing. I would especially like to thank my hardworking parents for teaching me through their words, lessons, and actions the value of education, hard work, and determination in reaching one's goals. Thank you Louise DeRusseau (Mom), Mark Ross (Dad), family, and friends for your support, love, and patience throughout my long educational venture. My deepest appreciation goes to Dr. Chyan for his guidance and teachings in my personal development in both academics and in the technology research industry. I am also grateful for my committee members for their time and support which have encouraged me and provided me with a well-rounded education during my PhD career. A hearty appreciation goes to all the wonderful personnel at the stockroom, the glass shop, the machine shop, the administrative offices, and the instrumentation lab for always being helpful and providing what is needed for my education and research. The Department of Chemistry at the University of North Texas (UNT) deserves a special thank you for their continued employment in the form of teaching assistant positions. A thank you to all involved in the advancement of the UNT as a Tier 1 research university, way to go! Thank you past and current members of Dr. Chyan's group for their intellectual help, encouragement, and support throughout these years. I acknowledge the USA Army, L-3, the Department of Physics at UNT, Intel, SRC, and Freescale for their generous support and guidance. Thank you Alpha Chi Sigma (AXS) chemistry fraternity for the networking and opportunities to further help the chemistry department. Again, thank you, and may God bless you all.

TABLE OF CONTENTS

Page

ACKNOWLEDGEMENTS ... iii

LIST OF TABLES ... ix

LIST OF FIGURES ... x

CHAPTER 1: INTRODUCTION OF INSTRUMENTS ... 1

1.1 Introduction to Dissertation ... 1

1.2 Introduction to Multiple Internal Reflection Infrared Spectroscopy (MIR-IR) ... 2

1.3 X-ray Photoelectron Spectroscopy (XPS) ... 6

1.4 Chemical Deposition ... 8

1.5 Physical Vapor Deposition (Sputtering) ... 11

1.6 Micropattern Corrosion Screening Technique ... 13

1.7 Quartz Crystal Microbalance (QCM) ... 14

1.8 Introduction to Packaging Corrosion ... 16

1.9 Electrochemistry ... 18

1.9.1 Tafel Plot ... 20

1.9.2 Cyclic Voltammetry (CV) ... 21

1.9.3 Linear Sweep Voltammetry (LSV) ... 22

1.10 Surface Analysis via Microscopy with Time Lapse Software 23

1.11 Gas Chromatography Mass Spectrometry 25

1.12 Contact Angle Measurement 27

1.13 References 28

CHAPTER 2: CHEMICAL BONDING CHARACTERIZATION OF BORON DOPED HYDROGENATED AMORPHOUS SILICON FILMS VIA MULTIPLE INTERNAL REFLECTANCE INFRARED SPECTROSCOPY 31

2.1 Introduction to Hydrogenated Amorphous Silicon Films 31

2.2 Introduction to Microbolometer 33

2.3 Experimental Information 38

2.4 Hydrogen Dilution and Boron Doping Effect On a-Si:H(B) Deposited On Si_xN_y:H Substrate 39

2.5 Silicon Nitrogen Layer Removal 41

2.6 Hydrogen Dilution And Boron Doping Effect On a-Si:H(B) Film 42

2.7 Deposition Condition Effects On Chemical Bonding Structure 46

2.8 X-ray Photoelectron Spectroscopy Analyzation On a-Si:H(B) Films 49

2.9 Conclusion 50

2.10 References 51

CHAPTER 3: CHEMICAL BOND CHARACTERIZATION OF BORON DOPED AMORPHOUS SILICON FILMS BY MULTIPLE INTERNAL REFLECTION INFRARED AND RAMAN SPECTROSCOPY AT 275ºC AND 365ºC SUBSTRATE TEMPERATURE ...53

3.1 Introduction To Boron Doped Hydrogenated Amorphous Silicon 53

3.2 Experimental Information 55

3.3 Organization Ratio Of *a*-Si:H(B) Films 57

3.4 Boron Concentration Effect On Resistance On *a*-Si:H(B) Films 59

3.5 Substrate Temperature Effect On Organization Of *a*-Si:H(B) Films By MIR-IR Analysis....60

3.6 Raman Analysis On *a*-Si:H(B) Films 69

3.7 Conclusion 74

3.8 References 75

CHAPTER 4: INVESTIGATION OF COPPER-ALUMINUM BIMETALLIC CORROSION IN HUMID CHLORIC RELATED ENVIRONMENTS..78

4.1 Introduction..78

4.2 Experimental 82

4.2.1 Micropattern Corrosion Sputtering Metrology 82

4.2.2 Industry Wire-Bonded Samples 83

4.2.3 Time Lapse Screening Metrology 85

4.24 Tafel plots, SEM, EDX, and XPS 87

4.3 Al Corrosion Progression....87

4.4 Al Corrosion Variables....92

4.4.1 Chloride Concentration, pH Of Solution, And Time References....92

4.4.2 Temperature And Pressure....97

4.5 Cu/Al Bimetallic Effect On Corrosion....100

4.6 Cu-Wire Bonded Devices....103

4.7 Pd Coated Cu-Wire Bonded Devices....104

4.8 Bimetallic Interface Versus Intermetallic Compound....107

4.9 Direct Current Measurements....108

4.10 Linear Sweep Voltammetry (LSV)....110

4.11 Tafel Plot....113

4.12 Cu/Al Bimetallic Corrosion Mechanism....114

4.13 Cu/Al Bimetallic Corrosion Inhibition....118

4.14 Au Wire Bonded Devices....122

4.15 Effect of Fluoride....123

4.16 Conclusion....124

4.17 References....125

CHAPTER 5: SUMMARY AND PROPOSED FUTURE STUDIES....129

5.1 Summary Of New Research Findings......129

5.1.1 MIR-IR Characterization Of Amorphous Silicon......129

5.1.2 Cu/Al Bimetallic Interface Corrosion......130

5.2 Proposed Future Studies......133

5.2.1 Deposition Of Amorphous Silicon Via Hot-Wire Chemical Vapor Deposition (HWCVD)......133

5.2.2 Cu-Al Alloy Corrosion Proposed Study......136

5.3 References......139

LIST OF TABLES

Table 4.1: Excel sheet of samples tested in Immersion Corrosion Screening experiment at room temperature. Explanation from left column to the right. # Tested is the total number of 12 kÅ Al/ 500 Å Ta/ 2000 Å SiN samples tested at the certain pH and ppm of chloride shown on the following two columns. Percentage of samples with 10% surface area corrosion on Al surface of the sample within Day 1 to Day 15. 94

Table 4.2: Excel sheet of samples tested in Pressure Cooker Screening experiment. Samples were subjected to 121°C for 2 days. The pressure is increased by about 1 atm at this temperature totaling to 2 atm of pressure total. 98

Table 4.3: Linear Sweep voltammograms (LSV) of Aluminum, Copper and Copper dot on Aluminum. 110

LIST OF FIGURES

Figure 1.1: Schematic representation of MIR-IR setup.[1] Optically denser medium has refractive index n_1 whereas optically rarer medium has refractive index n_2. Also the radiation angle of incidence is designated by symbol θ and the critical angle is given by θ_C. 3

Figure 1.2: Background cancelation methodology for MIR-IR..4

Figure 1.3: MIR-IR (top) and TIR (bottom) spectra of a 50 nm *a*-Si:H thin film deposited on Si_xN_y:H...5

Figure 1.4: Display of compare and contrast of the diamond ATR-IR, external ATR-IR and MIR-IR metrology and attachment...6

Figure 1.5 (A) XPS chamber in (B) PHI 5000VersaProbe™ Scanning XPS.................................8

Figure 1.6: CVD system in Dr. Chyan's laboratory. 9

Figure 1.7: HWCVD system blue print. 11

Figure 1.8: Dual magnetron desktop pro sputtering machine. 13

Figure 1.9: Micropattern corrosion screening structure...14

Figure 1.10: QCM system setup. 15

Figure 1.11: Thin quartz crystal sandwiched between two metal electrodes. 15

Figure 1.12: Schematic of electrochemical cell showing anodic and cathodic sites. 16

Figure 1.13: Cu wire-bonded device..18

Figure 1.14: Schematic of a three electrode system electrochemical cell. 19

Figure 1.15: Tafel plot showing E_{corr}, I_{corr}, cathodic and anodic curves. 21

Figure 1.16: Tafel plot showing E_{corr}, I_{corr}, cathodic and anodic curves. 22

Figure 1.17: LSV with scan rate of 20 mV/s. Polarization curves were cathodic scanned from OCP and stop at potential where the cathodic current was significantly increased. Potential has been converted to SHE. LSV scan of Al (0.5%Cu), 100nm Cu dot/Al (0.5%) and Cu in pH 5 H_2SO_4 solutions. 23

Figure 1.18: (A) 16 mega pixal web cam set up, (B) Cannan EOS Rebel T5i DSLR camera set up (C) DXM 1200 Optical Microscope Nikon microscope set up (D) FEI Quanta 200 ESEM with EDS set up. 25

Figure 1.19: Finnegan TraceGC ultra Trace DSQ Mass Spectrometer used in Cu/Al bimetallic corrosion analysis..26

Figure 1.20: Diagram of contact angle of liquid droplet. 28

Figure 2.1: (A) Crystalline structure. (B) Amorphous structure...31

Figure 2.2: Diagram of the atom pair distribution for crystalline, amorphous solid, and gas phases, showing the difference in average separation of the nearest neighboring atom (R_{av}). 32

Figure 2.3: Amorphous, micro-crystalline and crystalline silicon in terms of film thickness and hydrogen dilution $[H_2]/[SiH_4]$..35

Figure 2.4: Attenuated total reflectance (ATR) wave guide for FT-IR analysis. 36

Figure 2.5: MIR-IR (top) and TIR (bottom) spectra of a 50 nm *a*-Si:H thin film deposited on Si_xN_y:H...37

Figure 2.6: Hydrogenated amorphous silicon structure example with the main chemical bonds with an example MIR-IR spectra for reference. 38

Figure 2.7: MIR-IR spectra of 50 nm *a*-Si:H thin films deposited with different PECVD grown parameters (A) boron doping [BCl_3]/[SiH_4] ratio 0.02 to 0.32, (B) hydrogen dilution [H_2]/[SiH_4] ratio 30:1 to 100:1. (C) Si-H (1990cm^{-1}) and B-H (2465cm^{-1}) peak height values from Figure 2.7 (A). (D) Si-H (1990cm^{-1}) and B-H (2465cm^{-1}) peak height values from Figure 2.7 (B). 41

Figure 2.8: MIR-IR spectra of an *a*-Si:H thin film a) with a Si_xN_y:H underlying layer b) without a Si_xN_y:H underlying layer to reveal important SiH_2 and O-SiH_x peaks of *a*-Si:H 42

Figure 2.9: MIR-IR spectra set of an *a*-Si:H(B) thin film verifying in boron concentration and hydrogen dilution. 43

Figure 2.10: Effects of PECVD grown parameters of boron doping [BCl_3]/[SiH_4] ratio and hydrogen dilution [H_2]/[SiH_4] ratio on IR absorption peaks heights of (A) B-H and SiH_2 and (B) Si-H peak heights in *a*-Si:H thin films...44

Figure 2.11: MIR-IR spectra set of an *a*-Si:H thin film varying in (A) boron concentration and (B) hydrogen dilution. (C) Si-H and B-H peak height values from Figure 2.11 (A). (D) Si-H and B-H peak height values from Figure 2.11 (B). 46

Figure 2.12: (A&B) XPS spectra of an a-Si:H(B) film with 0.32 BCl3/SiH4 boron concentration and 60:1 [H2]/[SiH4] hydrogen dilution. (C&D) XPS spectra of an a-Si:H(B) film with 0.12 BCl3/SiH4 boron concentration and 60:1 [H2]/[SiH4] hydrogen dilution..................................50

Figure 3.1: 1000 angstrom thick *a*-Si:H(B) layer on top of silicon substrate. Two infrared spectra using two different techniques (MIR and TIR) on the same sample. Peak height is in micro-absorbance units (mabs)....57

Figure 3.2: Amorphous, micro-crystalline and crystalline silicon in terms of film thickness and hydrogen dilution $[H_2]/[SiH_4]$....58

Figure 3.3: Hydrogenated amorphous silicon structure example with the main chemical bonds with an example MIR-IR spectra for reference. 59

Figure 3.4: (A) resistivity vs boron concentration (r) = $[BCl_3/ SiH_4]$. (B) Active and non-active boron doping configurations with a MIR-IR spectrum of an *a*-Si:H(B) sample. 60

Figure 3.5: MIR-IR spectra of two *a*-Si:H(B) films grown at 365°C and 275°C substrate temperature. Intensity is reduced by a factor of 2 for the MIR-IR spectrum of the 275°C sample due the film having a film thickness double than the 365°C sample. 62

Figure 3.6: Ten MIR-IR spectra of *a*-Si:H(B) films grown at 275°C substrate temperature. Hydrogen dilution values of 4/1, 10/1, 16/1 and 40/1 $[H_2/SiH_4]$ and with boron concentration values of 0.12, 0.27 and 0.32 $[BCl_3/SiH_4]$. 63

Figure 3.7: (A) Four *a*-Si:H(B) samples grown at substrate temperature 275°C and analyzed by MIR-IR spectroscopy. These samples have a boron concentration value of 0.32 $[BCl_3/SiH_4]$ and hydrogen dilution values of 4/1, 10/1, 16/1, and 40/1 $[H_2/SiH_4]$. (B) Seven *a*-Si:H(B) samples were grown at substrate temperature 365°C and analyzed by MIR-IR spectroscopy. These samples have a boron concentration value of 0.32 $[BCl_3/SiH_4]$ and hydrogen dilution values of 16/1, 30/1, 45/1, 49/1, 55/1, 70/1, and 100/1 $[H_2/SiH_4]$....64

Figure 3.8: (A-C) Three *a*-Si:H(B) samples grown at substrate temperature 275ºC and analyzed by MIR-IR spectroscopy. These films have boron concentration values of 0.12, 0.27, and 0.32 [BCl_3/ SiH_4] and hydrogen dilution value of (A) 4/1, (B) 10/1, and (C) 16/1 [H_2/SiH_4] 66

Figure 3.9: MIR-IR analysis of hydrogen dilution dependent line graph showing normalized peak height of B-H, SiH_2, and SiH bonds on *a*-Si:H(B) films with varying hydrogen dilution values and boron concentration 0.32 [BCl_3/ SiH_4] at (A) 275ºC (B) 365ºC substrate temperature 68

Figure 3.10: Raman analysis showing normalized peak height of Transvers acoustic (TA) at 154cm^{-1}, Longitudinal acoustic (LA) at 310cm^{-1}, Longitudinal optical (LO) at 405cm^{-1}, and Transverse optical (TO) at 475cm^{-1} on *a*-Si:H(B) films at (A) 275ºC (B) 365ºC substrate temperature. 71

Figure 3.11: Displays values of (A) [Si:H2]/[[Si:H]+ [Si:H2]] ratio and (B) ITA/ITO ratio from MIR-IR and Raman analysis respectfully. 73

Figure 4.1. Standard reduction potentials of selected metals...79

Figure 4.2: Micropattern corrosion screening product metrology. 83

Figure 4.3: Wire-bonded sample structure...84

Figure 4.4: SEM image of wire-bonded sample dimensions. 85

Figure 4.5: Morphological Progression of Corrosion. Left to right SEM images of; As is, initial surface roughness, dendrite formation and mudcrack (severe corrosion). All samples are of 1.2 micron thick of Al (0.5% Cu by wt.)/ 5 nm Ta/ SiN substrate. 89

Figure 4.6: 12 kÅ Al/ 500 Å Ta/ 2000 Å SiN (A) as is. (B) in 5ppm Cl^- 5pH for 2 hours. 91

Figure 4.7: All three images are of the same sample: 12 kÅ Al/ 500 Å Ta/ 2000 Å SiN in a 20ppm Cl^- solution at 4pH (H_2SO_4) for 96 hours. Image on the left is taken at 50X maginification by a DXM 1200 Nikon Optical Microscope. Middle image is taken via Nikon microscope at 500X magnification. Image at the right is taken by Nova NanoSEM 230. 92

Figure 4.8: 3D graph of the data shown in Figure 4.7 (excel sheet of the Immersion Corrosion Screening.) X-Axis = pH, Y-Axis = ppm Chloride, and Z-Axis = Percent of Occurrence of Corrosion at 10% or higher. 3D graph (A) is at the 2 day mark and the 3D graph (B) is at the 10 day mark..96

Figure 4.9: 3D graph of the data shown in Figure 4.10 X-Axis = pH, Y-Axis = ppm Chloride, and Z-Axis = Percent of Occurrence of Corrosion at 10% or higher. (A) Shows the full system, (B) shows only ≥5 ppm Cl^- and 4-5pH system. 99

Figure 4.10: Corrosion progression comparison of 100 nm thick Cu microdot sputtered on 1.2 micron Al (0.5% Cu) versus only Al (0.5% Cu) placed into a 2ppm Cl^- solution at 5 pH using sulfuric acid. 101

Figure 4.11: 30 second hydrogen evolution on Al/Cu interface area analyzation with; (A) Nikon microscope, (B) SEM and (C) EDX. Al/Cu sample was submerged in 1ppm Cl^- 5pH solution.102

Figure 4.12: Cu-wire bonded on Al pad device submerged in 5ppm Cl- 5pH solution for (A) 0 mins, (B) 22 mins, (C) 4 hours 12 mins..104

Figure 4.13: (A) Corrosion screening via microscopic time lapse experiment of a Pd-coated Cu wire bonded on Al pad sample fully submerged in a 5ppm Cl^- 5pH solution. (B) Gas Chromatography Mass Spectrometry (GC-MS) analysis in situ of a wire-bonded sample submerged in a 5ppm Cl^- solution at 5 pH for over 42 hours in a closed vial. 106

Figure 4.14: (A) As is Pd-coated Cu wire bonded on Al pad. (B) Pd-coated Cu wire bonded on Al pad Corrosion screening via microscopic time lapse experiment in in 5ppm Cl^- 5pH solution for 48 hours....107

Figure 4.15: DC measurements with using platinum as the anode and (A) Al, (B) 50nm Cu dot on Al (C) Al (0.5% Cu by wt.) (D) Cu dot on Al (0.5% Cu by wt.) samples as the cathodes in varying concentrations of chloride solution, all at pH of 5....109

Figure 4.16: LSV with scan rate of 20 mV/s. Polarization curves were cathodic scanned from OCP and stop at potential where the cathodic current was significantly increased. Potential has been converted to SHE. (A) LSV scan of Al (0.5%Cu), 100nm Cu dot/Al (0.5%) and Cu in pH 5 H_2SO_4 solutions (B) Multiple LSV scan of Al (0.5%Cu). 112

Figure 4.17: Tafel plot of Al (0.5% Cu), Cu dot/Al (0.5% Cu), and 50 nm Cu/Si in a 5ppm Cl^- 5pH solution....114

Figure 4.18: Proposed bimetallic corrosion mechanism of Al pad with Cu ball attachment. 117

Figure 4.19: Proposed inhibition of bimetallic corrosion of Al pad with Cu ball attachment.....118

Figure 4.20: Pd coated on a Cu wire which is bonded with an Al pad. (A) as is. (B) in a 5ppm Cl- 5pH solution for 17 hours. (C) 5ppm Cl- 5pH 0.1% by weight of BTA solution for 12 days. ...120

Figure 4.21: LSV with scan rate of 20 mV/s. Polarization curves were cathodic scanned from OCP and stop at potential where the cathodic current was significantly increased. Potential has been converted to SHE. (A) LSV scan of Al (0.5%Cu) (B) LSV scan of 50nm Cu dot/Al (0.5%).....121

Figure 4.23: Au wire bond to Al pad device (A) as is (B) 6 days 8 hours submerged in 5ppm Cl- 5pH solution (C) 8 days 1 hour in 5ppm Cl- 5pH solution....123

Figure 4.24: (A): Al (0.5% Cu by wt) submerged in a 5 ppm F^- 4pH solution for 48 hours. (B) Al (0.5% Cu by wt) submerged in a 5 ppm Cl^- 4pH solution for 48 hours. (C) 50 nm Cu dot on Al (0.5% Cu by wt) submerged in a 5 ppm F^- 5pH solution for 3 days. (D) 50 nm Cu dot on Al (0.5% Cu by wt) submerged in a 2 ppm Cl^- 5pH solution for 36 hours. 124

Figure 5.1: (A) Hot-wire Chemical Vapor Deposition (HWCVD) system.[2] (B) Visual representation of silane and hydrogen molecules being catalyzed by a tungsten wire and then depositing on a film substrate. 135

Figure 5.2 (A&B) Images via Powerscope imaging of electrodes after 24 minutes of immersion in 5 ppm chloride at 5pH solution. (A) Micropatterned copper on aluminum alloy base metal and (B) micropatterned copper on pure aluminum. (C) Micropatterned copper on aluminum with 0.5% copper electrodes versus platinum. (D) Micropatterned copper on pure aluminum electrodes versus platinum. 138

Figure 5.3 (A) Calibration of aluminum thickness (nm) versus current supplied to the direct current target. (B) Physical vapor deposition process used to sputter thin films of metals. (C) Calibration of copper thickness (nm) versus power (W) supplied to the radio frequency target. 139

CHAPTER 1

INTRODUCTION OF INSTRUMENTS

1.1 Introduction to Dissertation

This dissertation is the cumulative effort of my research work done in my position as a PhD student in the interfacial electrochemistry and materials research lab (IEMR) at University of North Texas Chemistry Department from January 2011 to May 2016. With the guidance and teachings of my adviser, Dr. Oliver Chyan, I have developed a trade to use my knowledge of chemistry to solve problems for the semiconductor industry. Chemistry plays an important role in the development of integrated circuits (IC), and some of the greatest challenges are not in device or design rather the ability to manufacture the components that are reliable and cost effective. With the fast evolution of industry research, and innovation challenges can completely change month to month. One will have to be constantly teaching oneself to reach master level in new areas of research to solve current IC fabrication challenges. Now looking back I see the priceless value of what I have been taught and the trade I have mastered.

The organization of this dissertation is as follows. Chapter 1 discusses the techniques and instruments that have been used in my PhD career to carry out the projects in chapters 2-5. Chapters 2 and 3 contain the work done for the chemical bonding characterization of boron doped hydrogenated amorphous silicon (a-Si:H(B)) using multiple internal reflection infrared spectroscopy (MIR-IR) analytical technique. Chapter 4 highlights key findings in the extensive screening and investigation of copper-aluminum bimetallic corrosion in humid chloric related environments in IC packaging. In chapter 5, I conclude my dissertation with proposing further explorations and future plans for a-Si:H(B) and Cu/Al bimetallic interface research projects.

1.2 Introduction to Multiple Internal Reflection Infrared Spectroscopy (MIR-IR)

MIR-IR is a technique based on internal reflection spectroscopy, pioneered by Harrick and Fahrenfort.[1,2] Total internal reflection occurs at the interface of two media when radiation propagates from the optically denser medium (refractive index n_1) to the optically rarer medium (refractive index n_2, $n_1 > n_2$), and the radiation angle of incidence (θ) is greater than the critical angle (θ_c). The critical angle is a function of refractive indices of two media and is given by:

$$\theta_C = \sin^{-1}\left[\frac{n_2}{n_1}\right] \qquad \text{(eq. 1.1)}$$

An evanescent wave is propagated with every reflection into the adjacent optically rarer medium which is displayed in Figure 1.1. The evanescent wave can be further defined as a standing electric wave normal to the interface of the two media, and it arises due to the superposition of the electric fields of the incident and reflected waves. The amplitude of the evanesant wave (*E*) decays exponentially with distance from the interface, as given by:[1]

$$E = E_0 e^{-\left(\frac{z}{d_p}\right)} \qquad \text{(eq. 1.2)}$$

where d_p is the penetration depth, z is the distance from the interface, λ is the wavelength of the radiation, θ is the incidence angle, and E_0 is the amplitude of the electric field at the interface ($z = 0$). The penetration depth (d_p) is the distance where the amplitude of the electric field is $1/e$ of E_0, which is a function of refractive indices n_1 and n_2.[1]

$$d_p = \frac{\lambda}{2\pi\sqrt{n_1^2 \sin^2\theta - n_2^2}} \qquad \text{(eq. 1.3)}$$

If the optically rarer medium absorbs IR radiation then the attenuated total reflection (ATR) will result at characteristic wavelengths, which corresponds to the vibrational resonant frequency. The principle of MIR-IR is shown schematically in the figure below:

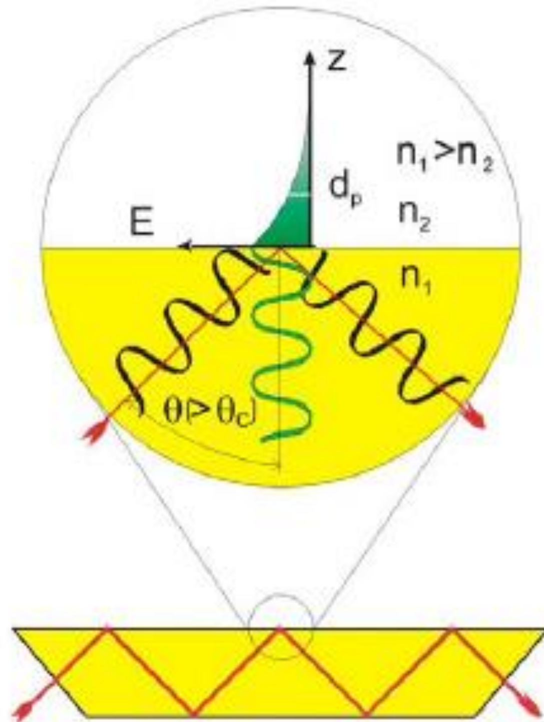

Figure 1.1: Schematic representation of MIR-IR setup.[3] Optically denser medium has refractive index n_1 whereas optically rarer medium has refractive index n_2. Also the radiation angle of incidence is designated by symbol θ and the critical angle is given by θ_C.

ATR waveguide is fabricated in house to facilitate MIR within the wafer itself. The wafer is cut into a 60 x 10 mm rectangle and polished on either side to make a 45° bevel angle by mechanical polishing by a multiprep pro from Allied High Tech. For Si<100> background ATR coupons, a standard cleaning (SC1) solution made of 5 parts deionized water, 1 part aqueous NH_4OH (29% by weight of NH_3), and 1 part aqueous H_2O_2 (30%) was used to remove any organic

contamination from the surface followed by etching in 0.5% HF solution. IR spectra were recorded on a Nicolet IS 50 and Bruker V70 FTIR spectrometer under constantly purged dry air ($CO_2 < 1$ ppm) via a Parker purge generator. Both transmission (TIR) and MIR-IR infrared spectra were measured. All spectra were collected at 2 cm^{-1} resolution and are the average of 100 individual spectra. The detection limit of MIR-IR is ca. 0.2 mabs with an error margin of < 3%.

The MIR metrology is surface sensitive with background cancelation, Figure 1.2. The ratio of the single beam spectrum (sample) and the background spectrum (control) will yield the chemical bonding characterization of the surface chemistry of the sample in question. This is a common practice in the analytical field, however the combination of ultra-high MIR-IR sensitivity with this subtraction technique is what gives this metrology its niche.

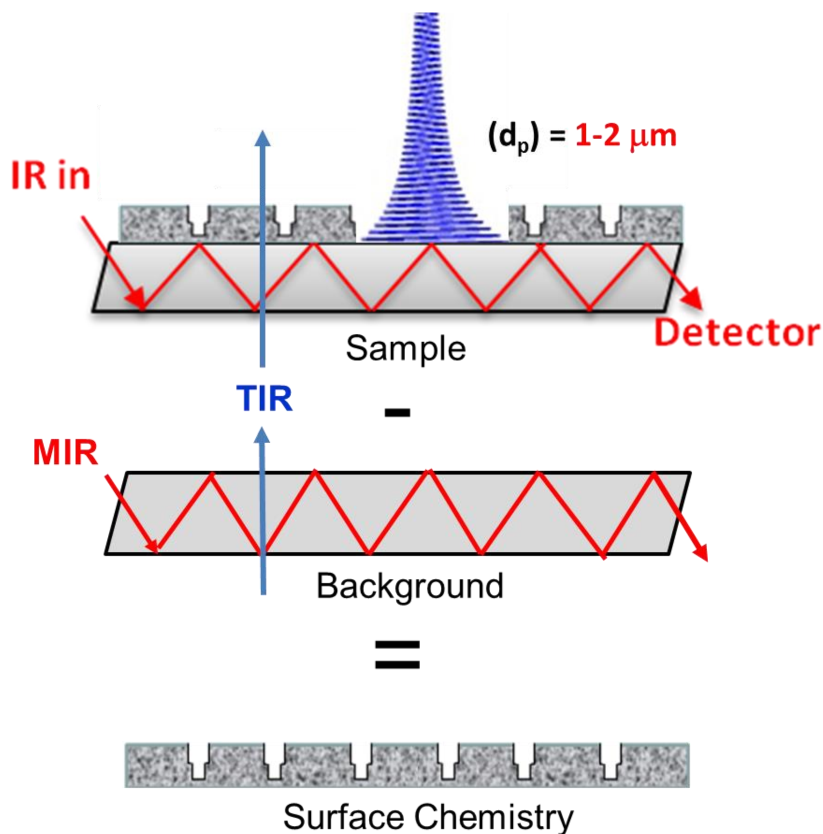

Figure 1.2: Background cancelation methodology for MIR-IR.

The infrared absorption spectra (MIR-IR and TIR) of the same *a*-Si:H thin film sample grown over Si_xN_y:H coated Si<100> substrate are put in the same y and x-axis and are shown in Figure 1.3. The difference in sensitivity of MIR-IR versus TIR is an over 100x increase. The MIR-IR spectrum in Figure 1.3 reveals well-resolved IR absorption peaks associated with Si-H (1989 cm^{-1}) and B-H (2465 cm^{-1}) bonding modes originated from *a*-Si:H thin film.[4] The observed infrared absorption peaks of N-H (3340 cm^{-1}) and SiH_x (2000 cm^{-1}) bonding modes can be assigned to the underlying Si_xN_y:H layer on Si<100> substrate.

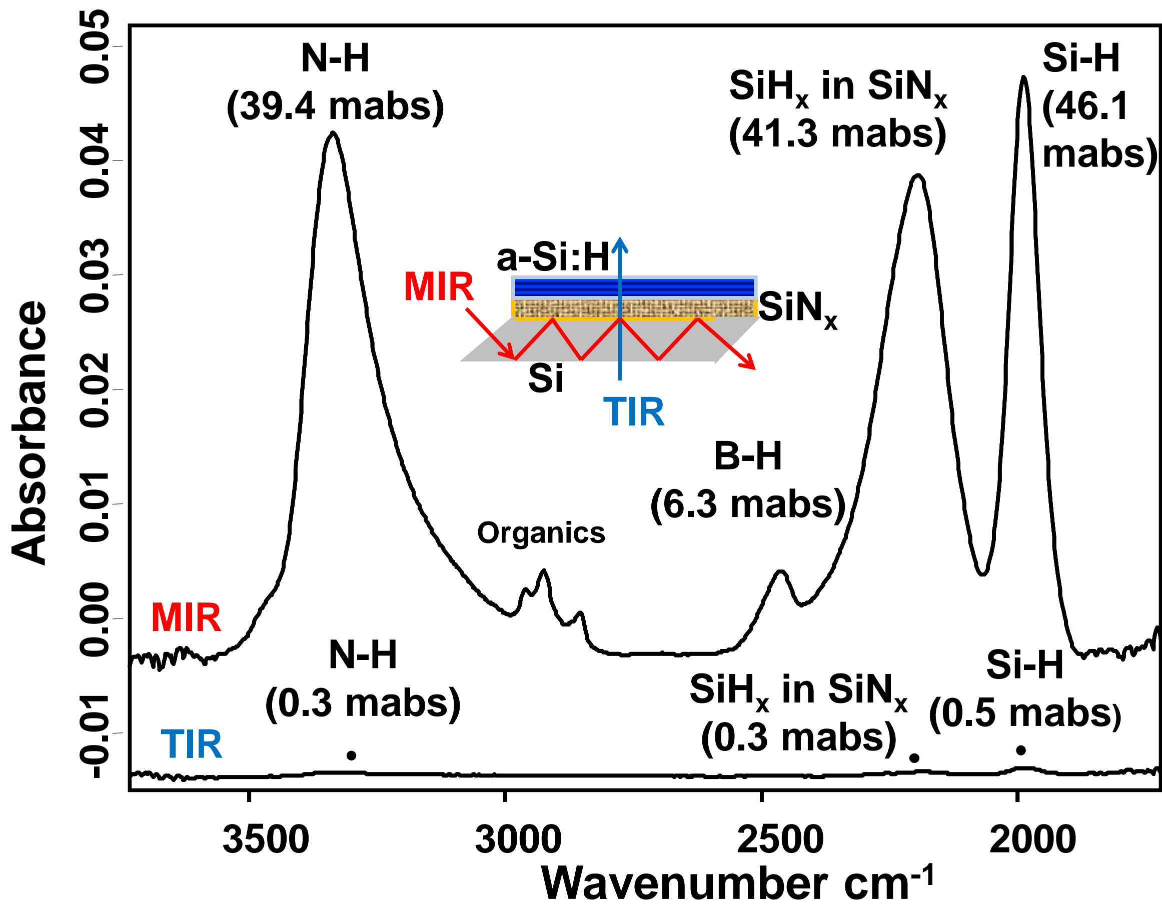

Figure 1.3: MIR-IR (top) and TIR (bottom) spectra of a 50 nm *a*-Si:H thin film deposited on Si_xN_y:H.

The MIR spectra were taken via a MIR accessory installed in an IS50 and V-70 FTIR spectrometer. Diamond and external ATR have a similar set up to MIR, and have a time efficiency advantage in sample prep over MIR metrology, Figure 1.4. However, diamond ATR-IR has a significant decrease in intensity due to less reflections in the sample. Also, diamond and external ATR have issues of direct sample contact to the ATR waveguide whereas this is a non-issue with MIR-IR due to the ATR waveguide is the sample itself, Figure 1.2.

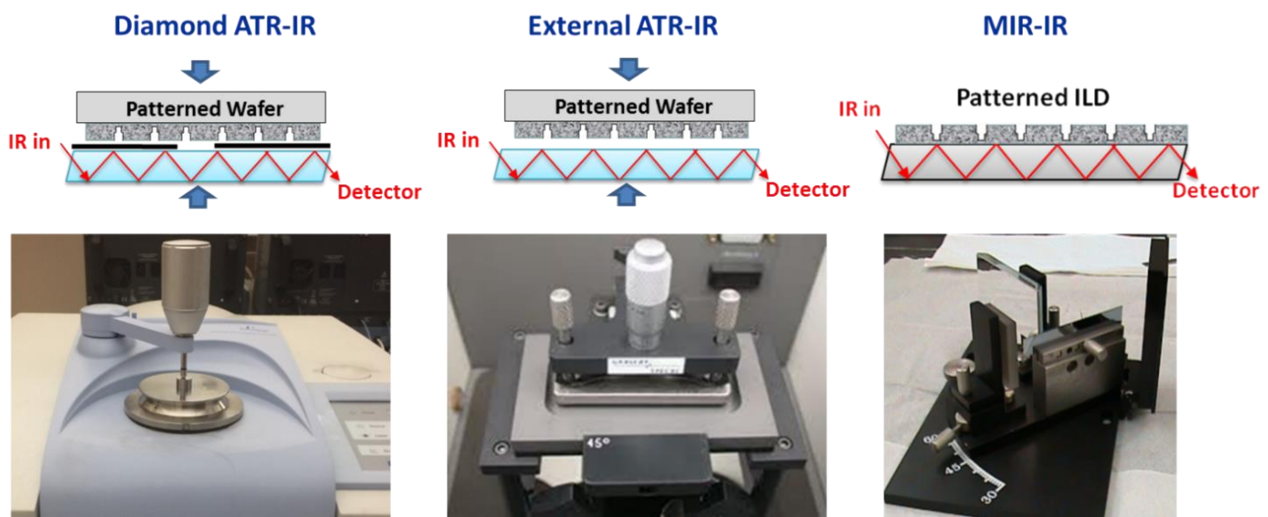

Figure 1.4: Display of compare and contrast of the diamond ATR-IR, external ATR-IR and MIR-IR metrology and attachment.

1.3 X-ray Photoelectron Spectroscopy (XPS)

X-ray photoelectron spectroscopy (XPS) is a technique which is widely used in the field of surface science.[5] The X-ray photon energy ($E = hv$) is the product of Planck's constant ($h= 6.623 \times 10^{-34}$ Joules x Second) with the frequency of the X-ray radiation (v). The X-ray photoemission is generated by a high flux X-ray source with an Aluminum anode and quartz crystal monochrometer in order to focus and scan the beam on the sample. There is a photoemission onto the specimen surface if the core electron is able to overcome the binding

energy (E_B). XPS is under ultra-high vacuum (UHV; < 10^{-9} Torr) due to the fact that emitted photoelectrons must travel a relatively long distance to the detector in order to avoid losing the photoelectron through collisions on its way to the electron energy analyzer. Consequently, the XPS signal counts were collected by the 16 channel detector system. The energy of the photoelectron E_k is related to the atomic and molecular chemical environment where it is emitted. So, XPS can provide qualitative and quantitative information on nearly all elements present on a very top specimen (except H and He) within 7 to 10 nm depth. Photoemission may be viewed such that:

$$E_B = h\nu - E_k \qquad \text{(eq. 1.4)}$$

Where E_B is the binding energy of the electron needed to escape the vacuum energy level where the atom cannot exert influence on the electron. E_k is the kinetic energy of the emitted electron.[6] The emitted photoelectrons are channeled through an electrostatic hemispherical electron energy analyzer onto a large area detector that is measured. The hemispherical analyzer establishes an electrostatic field to allow only those electrons of a given pass energy to arrive onto the detector itself.[7]

Since the X-ray photon energy ($h\nu$) and E_k are known, E_B can be calculated. The binding energy also provides important information about the bonding characteristics of the environment. A chemical shift towards lower binding energy would be seen if a chemical element was to be in an electron donating environment whereas the higher binding energy would be observed when an element was in oxidation state.

The X-ray photoelectron spectroscopy was accomplished using a PHI 5000Versa Probe™ Scanning XPS as shown in Figure 1.5. A standard Al-Kα X-ray source at 280 watts along with electrostatic analysis in constant pass energy mode 19 of 114.7eV for survey scans and 23.5 eV

for detail scans was used. The Versa Probe scanning XPS provides a highly focused (10μm to 100μm) monochromatic X-ray beam, which can precisely focus on the concerned region and even map the chemical composition by scanning X-ray beam. A 100V to 5kV differentially pumped Ar ion gun with regulated leak valve is available for specimen cleaning and sputter depth profiling with monolayer resolution. Also, the Ar ion gun is used to neutralize the insulating materials to prevent the electronic field from emitting photoelectron on local area during the X-ray irradiation.

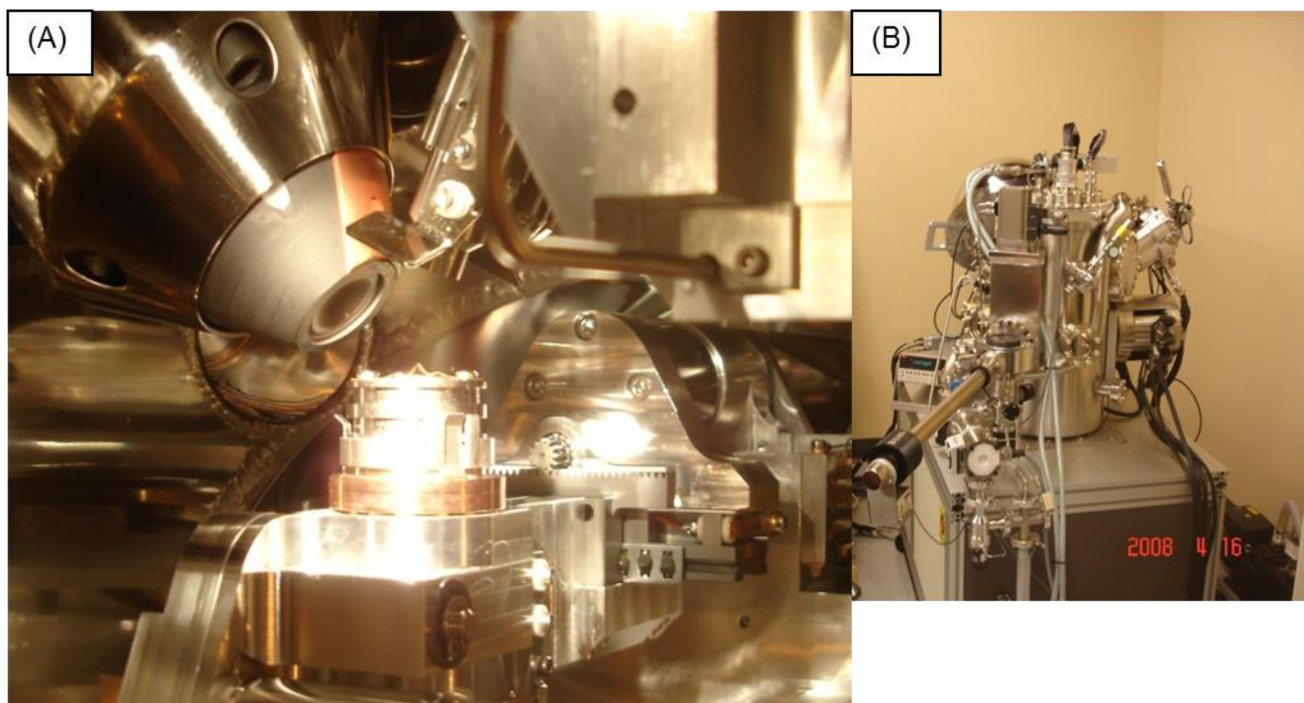

Figure 1.5 (A) XPS chamber in (B) PHI 5000VersaProbe™ Scanning XPS.

1.4 Chemical Deposition

Chemical deposition is a technique in which a fluid (gas or liquid) precursor undergoes a chemical change at the solid surface. Chemical depositions indicate that the process is primarily a chemical reaction during the deposition such chemical vapor deposition (CVD), Figure 1.6. The CVD requires a volatile precursor to react or decompose on the substrate surface. During the

chemical deposition, the gas-phase by-products are produced and then removed by gas flow through the reaction chamber. Atomic layer deposition (ALD) is similar to CVD, but the ALD is a self-limiting thin film deposition. The precursor reacts with a surface one-at-a-time in a sequential manner. By exposing the precursors to the surface repeatedly, atomic layer control of film growth rate can be obtained as fine as ~0.1 Å (10 pm) per monolayer. Recently, there has been a rapidly growing interest in ALD of materials used in microfabrication processes, especially in integrated circuits (ICs).[8,9]

Figure 1.6: CVD system in Dr. Chyan's laboratory.

A hot-wire chemical vapor deposition (HWCVD) system is similar to CVD, but HWCVD has a metal wire filament to catalyze the inlet gas. HWCVD includes a vacuum tight chamber, tungsten wire, electronic feed through, gas inlet valve, heater to heat up the substrate, thermocouple

and vacuum system to make thin films, Figure 1.7.[10] Coiled tungsten wire is most commonly used due to film quality, price, and availability. The tungsten filament is heated between 1900K to 2300K and generate the thermal energy to catalytically decompose the inlet gas molecules to reactive ions that then deposit on the desired film.[11] HWCVD has advantages over CVD in terms of deposition rate and the number of variables to better fine tune film growth. The use of a heated metal filament is necessary in order to provide thermal energy to and cause gas molecules to dissociate into ion fragments.

Currently, plasma enhanced chemical vapor deposition (PECVD) is the industry standard for thin film preparation. HWCVD method is gaining attention mainly due to its several advantages over PECVD. HWCVD has extra variables to better fine-tune the thin films than PECVD. Such variables include temperature, oscillating movement, and chemical element of the hot wire. It has been shown that HWCVD has produced thin films with less defects than PECVD.[11,12] This because ion bombardment is not a problem in HWCVD. HWCVD method uses thermal energy to catalytically decompose the inlet gas while PECVD uses electrical energy with ion bombardment to deposit the process molecules.

For PECVD, the plasma surface interactions involve atoms and molecular fragments such as radicals, ions and energetic photons. Electron energies in the plasma have a Maxellian distribution in the 0.1-20 eV range. These energies are sufficiently high enough to excite molecules or break chemical bonds at the depositing film. Radiative recombination is also a problem with films being deposited via PECVD. Radiative recombination occurs when a free electron combines with a radical atom and emits a photon. For example, $e^- + Ar^+ \rightarrow Ar + h\upsilon$, the photon from argon has an energy of 9.3 eV which is enough energy to break chemical bonds in the depositing film.[13,14] This chemical bond breakage due to ion bombardment and radiative recombination increases

defects within the depositing films and should be avoided. Instead of ion bombardment, HWCVD has small voltages present in the deposition chamber and any ions produced in the HWCVD chamber do not reside in the chamber long enough to become sources of particle formation. When an AC voltage is used to resistively heat the filament for HWCVD, any ions that may be produced are swept to the filament ends as well as the chamber walls due to the 60 Hz voltage oscillation.[15]

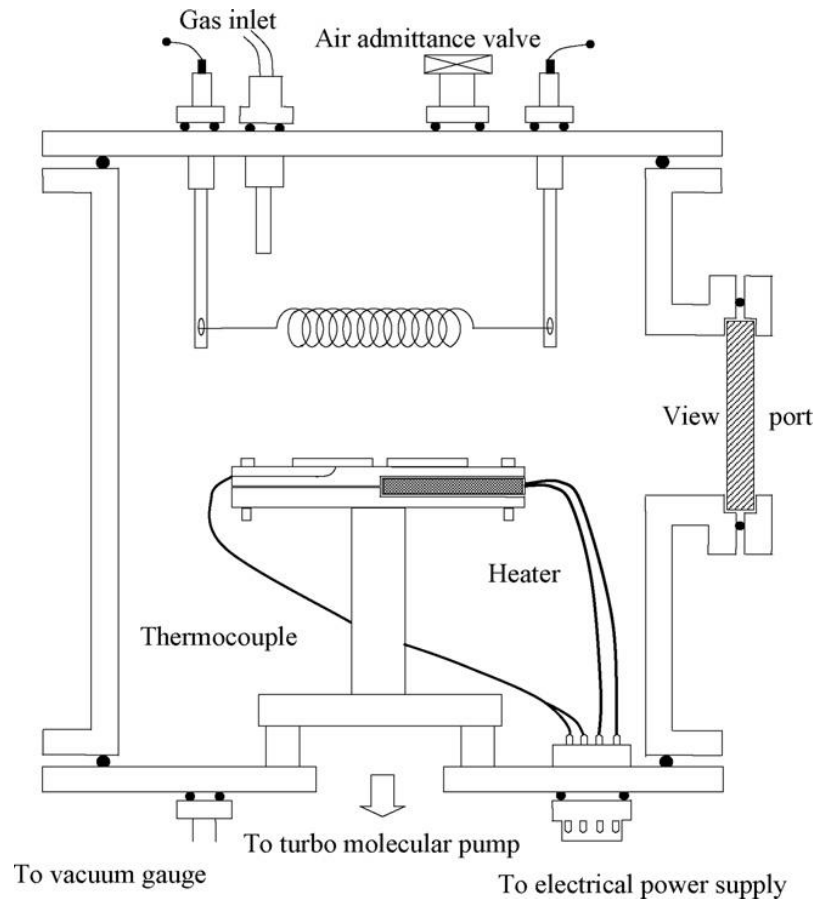

Figure 1.7: HWCVD system blue print.[16]

1.5 Physical Vapor Deposition (Sputtering)

Physical vapor deposition (PVD) uses an entirely physical method versus the chemical bonding method used in CVD. A vacuum is created via a pumping system and a noble gas (usually Argon) is let in to allow for a low pressure noble gas atmosphere. In Dr. Chyan's group, the PVD system uses scientific grade Ar. A magnet array generates a magnetic field. A high voltage is applied to the target along the magnetic field and creates a plasma. This area must be cooled (usually by a water cooling system) to keep the target material from being damaged. The created plasma is comprised of positively charged Ar^+ ions and electrons. The target is negative and attracts the Ar^+ ions. The Ar^+ ions then collide with the target which cause the target's atoms to be ejected and deposited opposite of the target onto the work space. Ar^+ will knock off atoms from the target only when the kinetic energy of the incoming particles is much higher than the conventional thermal energies.[17] The vacuum and concentration of Ar is important. For example, too few atoms of Ar cause are too few collisions to sustain the plasma, where as too many atoms cause an increase in the amount of Ar to Ar collisions and not enough Ar^+ atoms will hit the target due to mean free path.[17]

A dual magnetron Desktop Pro sputtering machine is used in this dissertation and is displayed in Figure 1.8. Desktop Pro sputtering machine can be operated with direct current (DC) and radio frequency (RF) sputtering guns. DC is a direct current where the cathode is the target and the workspace is the anode. Charge build-up (especially on insulating targets) can be avoided with the use of RF sputtering where the sign of the anode-cathode bias is varied at 13.56 MHz.[18]

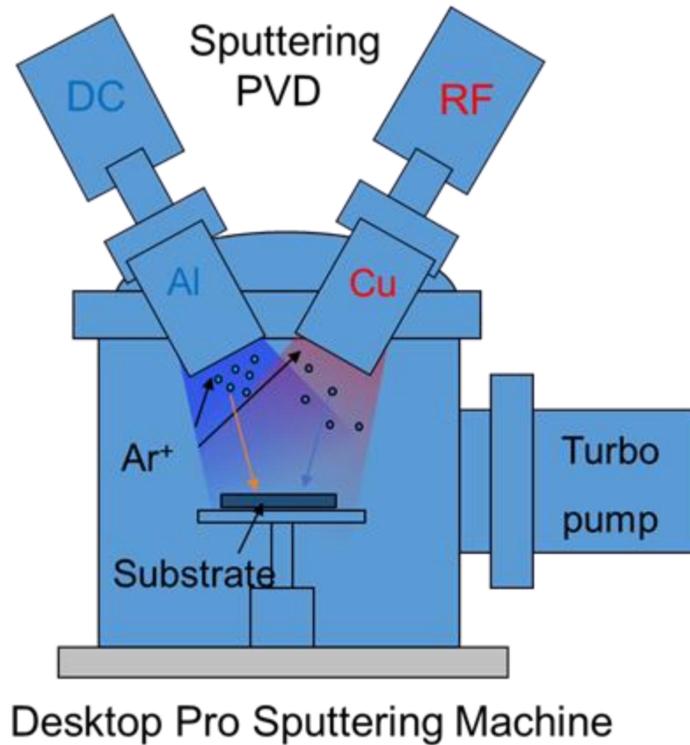

Figure 1.8: Dual magnetron desktop pro sputtering machine.

1.6 Micropattern Corrosion Screening Technique

The micropattern corrosion screening technique is a method that is used to study the result of two different metals being in contact, also called bimetallic corrosion. A microdot mask is place between the sputtering target and the deposit material shown in Figure 1.9. The microdot mask produces microdots 130 microns in diameter with varying varied thickness (depending on experimental needs) that are deposited on various substrates. Previous studies have used other metal combinations but in this dissertation the main bimetallic interface of interest is Al and Cu. The samples are submerged in an acidic chloride solution and an in situ time lapse investigation

via a metallurgical microscope. Figure 1.9 illustrates the micropattern corrosion screening structure.

The micropattern corrosion screening provides a time and cost efficient method for studying bimetallic corrosion and corrosion inhibition. Several variables like thickness of microdots can be controlled to study a range of corrosion rates with reasonable experimental time. Relative corrosion rate and corrosion progression data are collected in real time. Surface chemistry information is gathered by the direct imaging of the micropattern screening metrology. Once corrosion progresses, corrosion rate and corrosion mechanism are identified. Corrosion inhibitors can be identified and tested.[19,20]

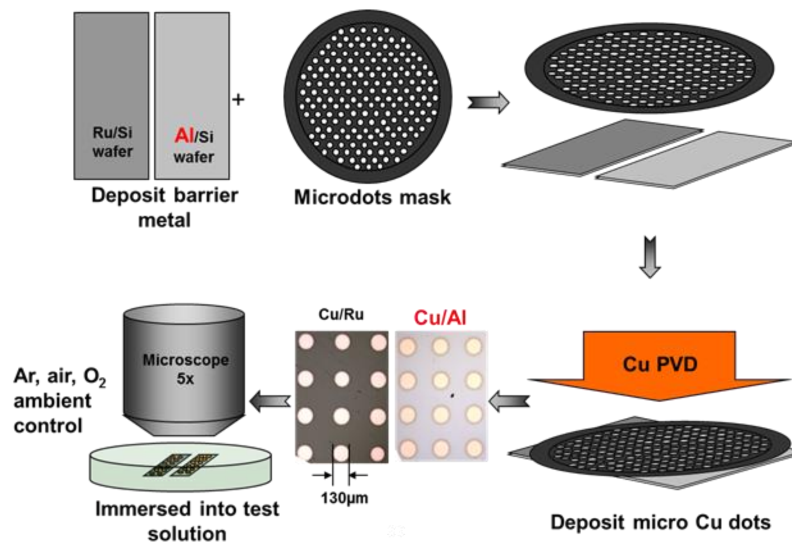

Figure 1.9: Micropattern corrosion screening structure.

1.7 Quartz Crystal Microbalance (QCM)

Quartz crystal microbalance (QCM) is the analytical technique which uses a QCM sensor as shown in Figure 1.10. The QCM is a piezoelectric device with an electric bias, is across an alpha

quartz crystal, which is sandwiched between two metal electrodes as shown in Figure 1.11. ECM is sensitive to mass changes on its electrodes with the electric field and the vibrational motion of the crystal at its resonant frequency. QCM is used to reveal detailed information about the adsorption or desorption process on electrode surface with mass changes before and after the PVD sputtering processes. This is the method to check film and dot thickness for the micropattern screening metrology.[21]

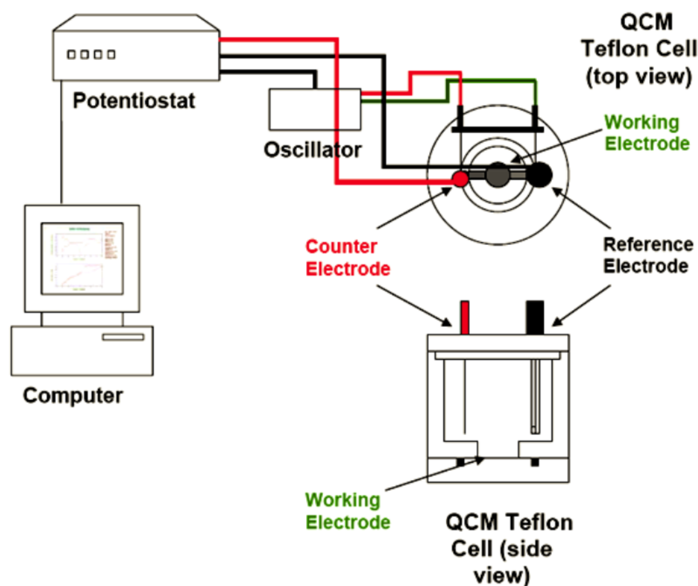

Figure 1.10: QCM system setup.

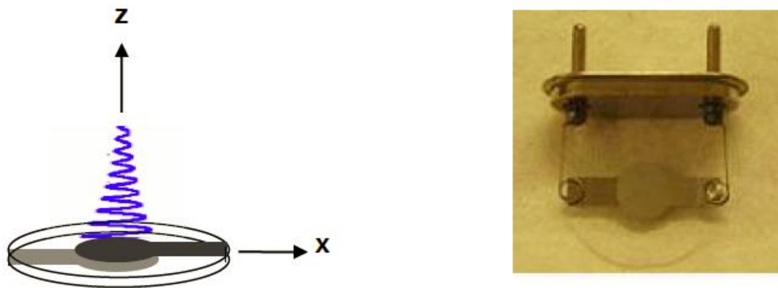

Figure 1.11: Thin quartz crystal sandwiched between two metal electrodes.

1.8 Introduction to Packaging Corrosion

Corrosion is the gradual destruction of a ceramic or metal material by the reaction with the environment.[22] When a metal is in an aqueous solution and corrosion is present the metal corrosion will transfer electrons from a metal surface to the aqueous electrolyte solution hence corrosion is an electrochemical reaction. Metals have a high tendency to react electrochemically with oxygen, water and other substances in an aqueous solution.[23,24] A metal surface usually has oxidation sites that give up its electrons (anodic reaction) in the metal and a reduction site that takes the electrons (cathodic reaction). The anodic reaction results in dissolution of metal which could be soluble ionic products or metal oxide. Several possibilities like reduction of dissolved oxygen or hydrogen evolution of cathodic reactions can occur depending on the reducible species present in the solution. Anodic and cathodic reactions occur simultaneously on a metal surface thereby creating an electrochemical cell as shown in Figure 1.12.[25,26]

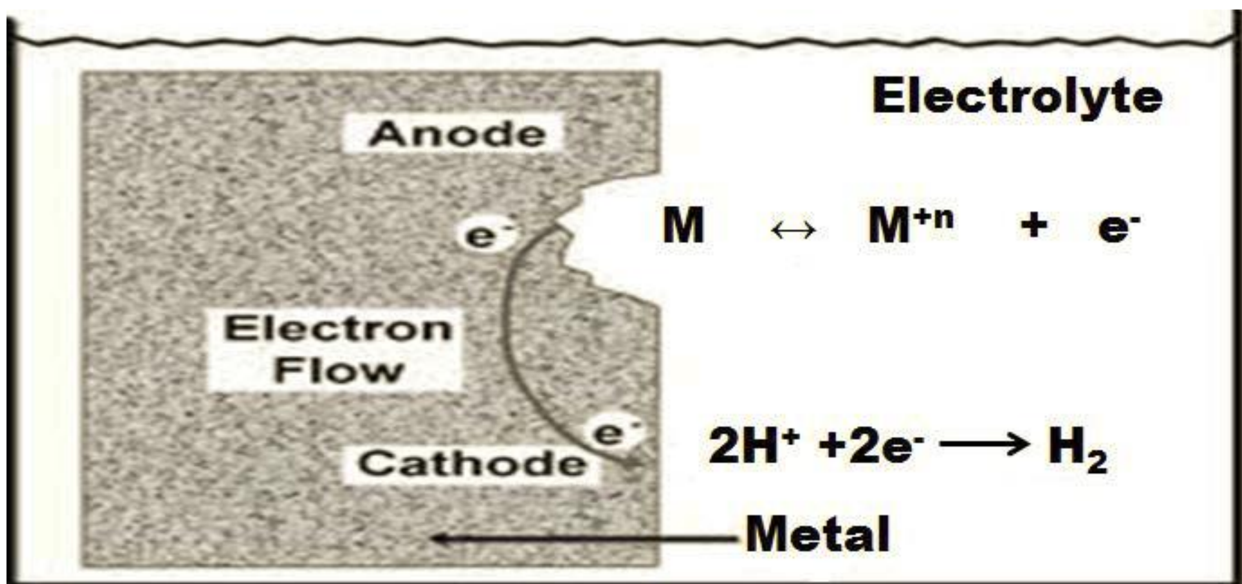

Figure 1.12: Schematic of electrochemical cell showing anodic and cathodic sites.[26]

Cathodic and anodic sites can switch in location, further apart or closer to one another. When one metal is in contact with another, one metal can be the cathode and the other the anode depending on the nobility of the metals. The less noble metal becomes the anode, hence is the metal where oxidation and corrosion takes place. In galvanic corrosion there is a transfer of electrons in which electrons flow from the anode to the cathode and form the corrosion current. The rate of production of electrons by the anode reaction and their consumption by the cathodic reaction determines the corrosion current. This is then used to determine the corrosion rate of the metal.

The estimated 20% of all microelectronic device failure is attributed to corrosion.[27] Corrosion is more of a concern for devices that are commonly used outdoors due to coming into contact with contamination such as chloride and moisture. Using Cu wire instead of Au wire attached in order to Al pads to provide electronic transfer is a common practice to make microelectronics more cost effective Figure 1.13.[28] Cu and Al are both metals with low corrosion resistance. To overcome this, the device is protected by an epoxy capsule, also known as packaging. It has been stated that epoxy resins have contamination of chloride and bromide.[29] If moisture were to get into the device, there would be water, electrolyte (Cl^-), and two dissimilar metals, which is everything needed for an electrochemical cell. This will cause a bimetallic corrosion reaction due to the 2eV difference in slandered reduction potential of Cu (+0.34 eV) and Al (-1.66eV).

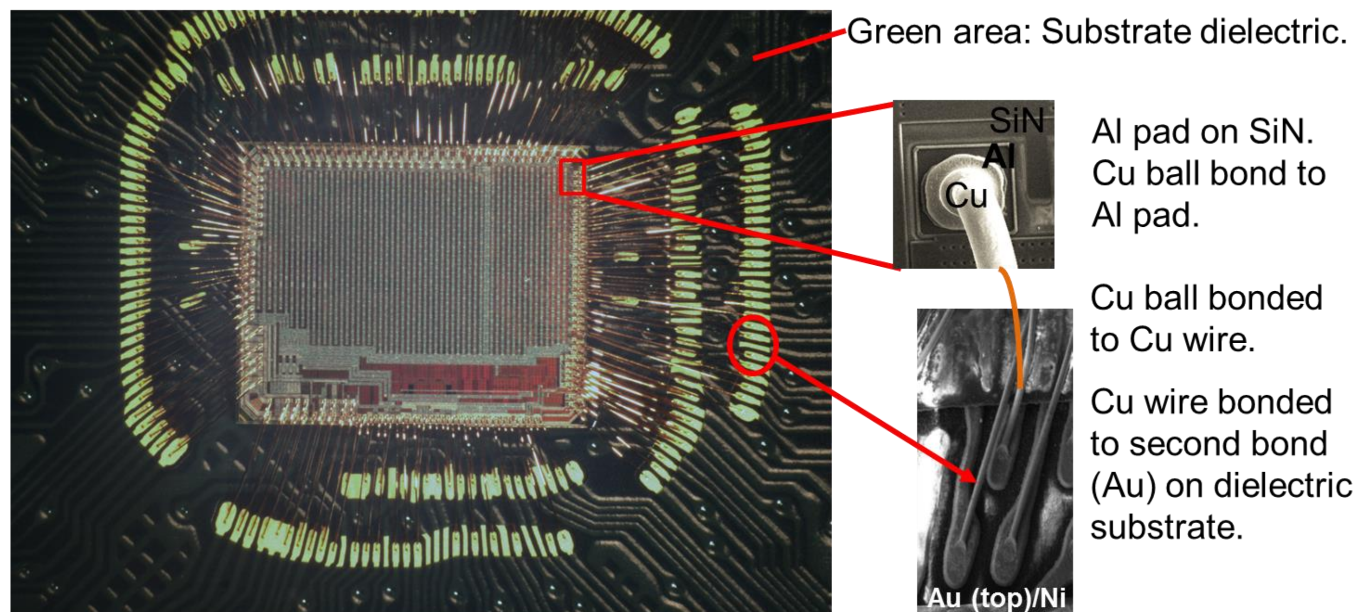

Figure 1.13: Cu wire-bonded device.

1.9 Electrochemistry

Electrochemistry is a branch of physical chemistry that studies chemical reactions taking place at the interface of an electrode, usually a semiconductor or a solid metal, and an ionic conductor, the electrolyte. A driving force is needed for an electron flow and the driving force is the difference in potential between a redox reaction. "Redox" stand for reduction-oxidation electron transfer in an electrochemical cell in which the anodic site is being oxidized and giving an electron to the cathodic site and thus is being reduced.[30] For example, when atomic sodium reacts with fluoride, sodium is oxidized by donating one electron to fluoride and sodium attains an oxidation state of +1. Fluoride is reduced once fluoride accepts the electron and fluoride's oxidation state is reduced to -1. The sign of the oxidation state (positive/negative) corresponds to the value of each ion's electronic charge. The atom or molecule which accepts the electron(s) is called the oxidizing agent, and the atom or molecule that loses electron(s) is known as the reducing

agent. Electrochemistry has various important applications: batteries, coating objects with metal(s) (damascene process), production of ores (ex. Al, Ti), diabetes blood sugar meters, and photosynthesis/solar cells.[30]

One way to measure an electrochemical reaction is displayed in Figure 1.14 which shows a schematic representation of a three electrode system in an electrochemical cell. In this dissertation the electrochemical analysis was done by a three electrode system. In a three electrode system there is a reference electrode, a working electrode and a counter electrode. A precise potential control is the main advantage of the three electrode system during the measurement over a two electrode system and is used widely in electrochemistry.

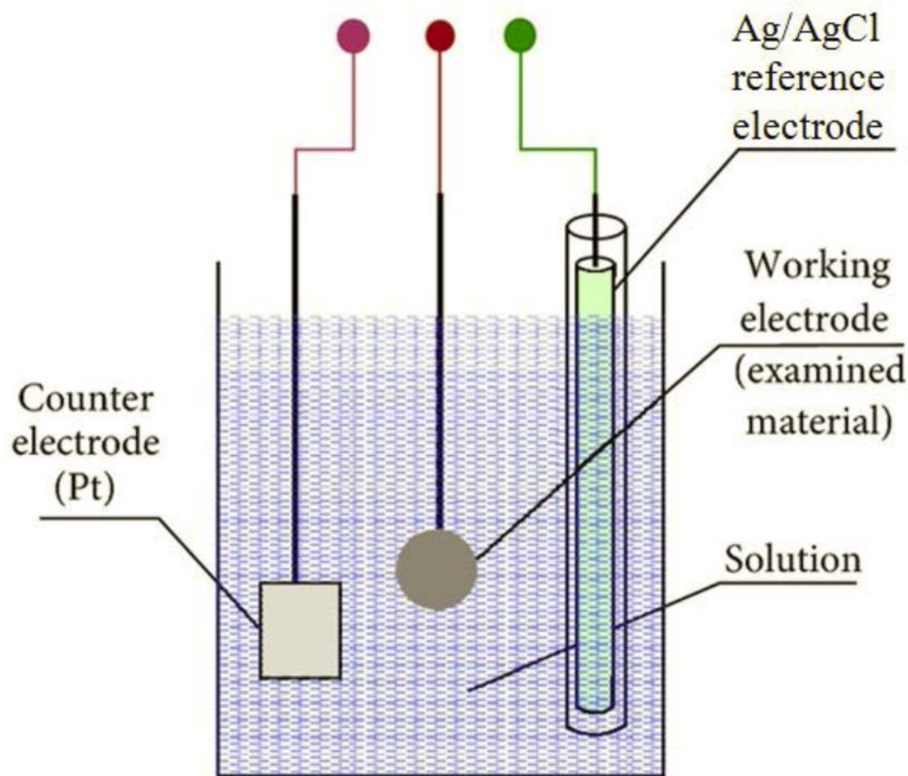

Figure 1.14: Schematic of a three electrode system electrochemical cell.

1.9.1 Tafel Plot

Tafel plot is a common electroanalytical technique to determine the corrosion of metal(s) in an electrolyte. A Tafel plot is a graph of the current density (I) against the overpotential (η) displayed as a logarithm. The Tafel equation relates the electrochemical reaction rate to overpotential. A polarized electrode produces a relationship between potential and current in an area which can be approached by:[31]

$$\eta = \pm B \log (I/I_0) \qquad \text{(eq. 1.4)}$$

Where I is the measured current density and the η is applied overpotential with respect to the open circuit potential. B and I_0 are constants where B is defined as the Tafel slope and I_0 is defined as the equilibrium current density. An example of a Tafel plot is shown in Figure 1.15. When following the correct procedure of collecting Tafel plot data, the potential is scanned from -250mV to +250mV with respect to open circuit potential (OCP) and the initial potential is set to the OCP of metal in the electrolyte. The rate at which a potentiostat changes a test electrode potential is the scan rate and has units of millivolts per second or volts per second. The scan rate used in Tafel plot is usually set to 1mV/s. E_{corr} and I_{corr} of the Tafel plot is extrapolated by the cathodic and anodic curve at the OCP. The more positive the E_{corr} value is, the more noble the metal will be. When two or more metals are compared the least noble metal will most likely oxidize first. When I_{corr} is closer to 0, the material is more resistant to corrosion. The corrosion rate and reaction kinetics of the corrosion or passivation of a metal is extracted from the potential and current information from the Tafel plot.[31]

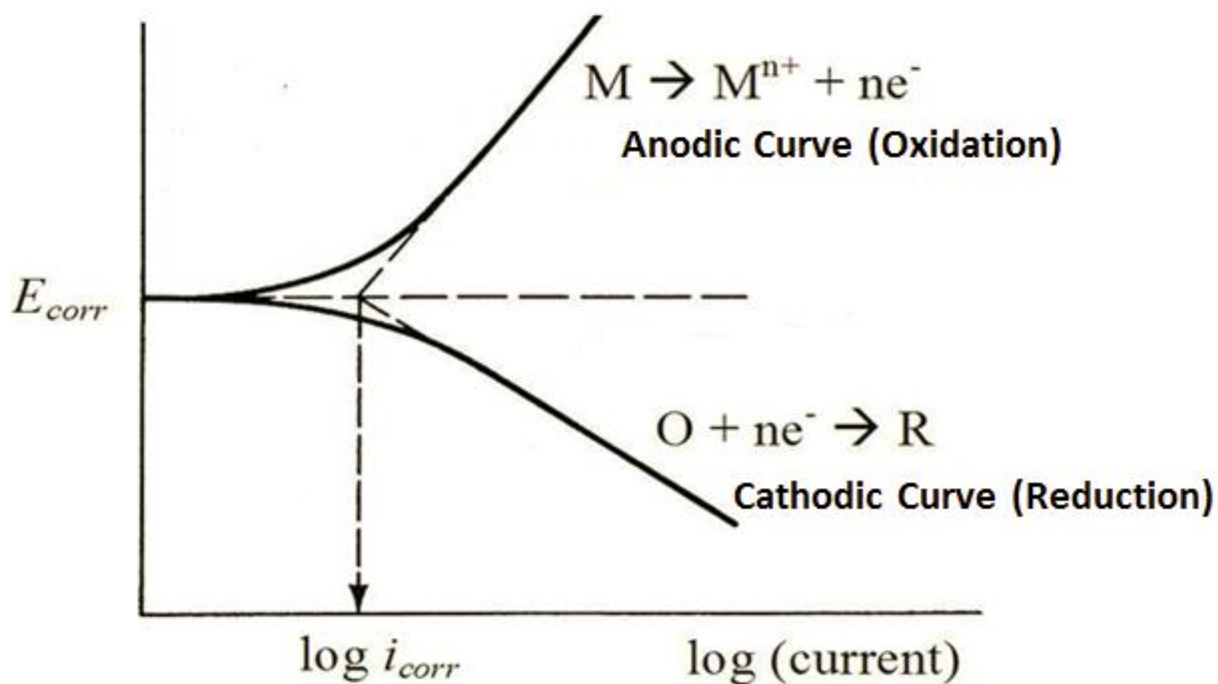

Figure 1.15: Tafel plot showing E_{corr}, I_{corr}, cathodic and anodic curves.[31]

1.9.2 Cyclic Voltammetry (CV)

Cyclic Voltammetry (CV) is a potentio-dynamic electrochemical measurement that can determine the redox properties of chemicals in electrolyte or electrochemical reactivity of a reactive electrode. In CV, the potential is measured between the reference and working electrode, and the current is recorded between the counter and working electrode. The plotted current (i) vs potential (E) from CV provides valuable electrochemical information.[31] The potential sweeps linearly back and forth with time in a predefined range. For example, the anodic forward scan of a reversible redox reaction will reach the potential of oxidation which produces the oxidative current peak. The reverse scan will have a similar reduction current peak which has a symmetrical shape

of oxidation peak. Thus the potentials of each reduction, oxidation, and the rate of electrochemical reaction can be obtained. An example of a CV is shown in Figure 1.16. Where $Fe(CN)6^{3-/4-}$ is represented as two potentials of E_a and E_c.[31]

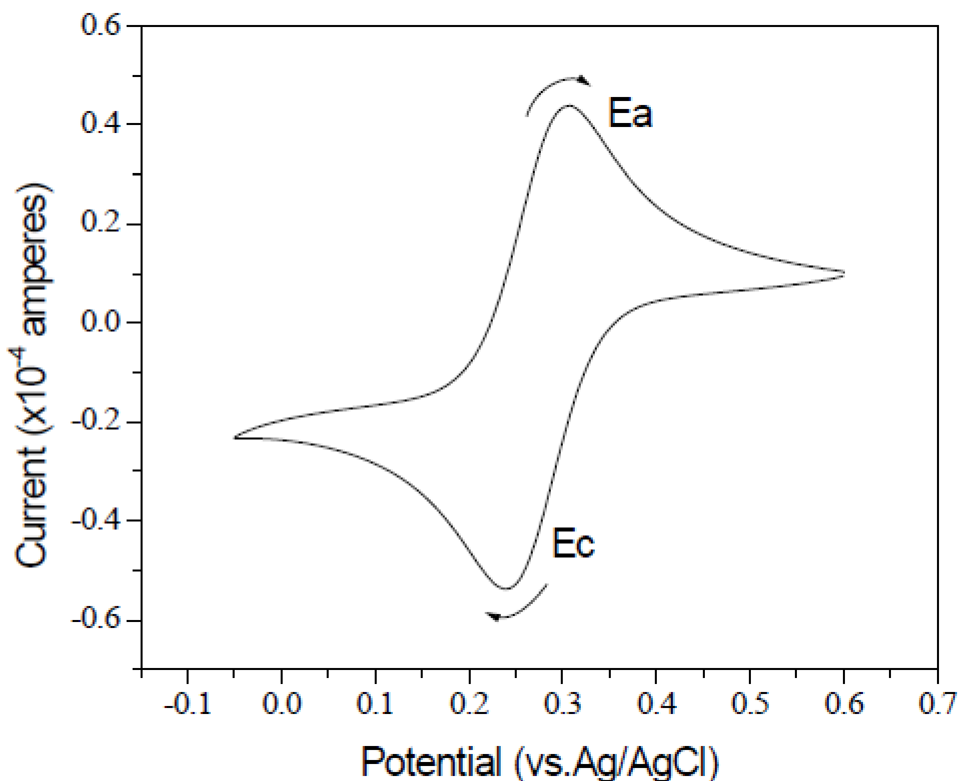

Figure 1.16: Tafel plot showing E_{corr}, I_{corr}, cathodic and anodic curves.[31]

1.9.3 Linear Sweep Voltammetry (LSV)

Linear sweep voltammetry (LSV) is a voltammetry method using a three-electrode setup in which the working electrode is measured while the potential between the reference electrode and working electrode is swept linearly in time. The working electrode is the point in which the oxidation/reduction reaction will occur and is what is being monitored. The flow of electrons out or into the electrode is the current being directly measured. When the rate becomes higher than the rate at which the oxidizing or reducing species can diffuse from the bulk of the electrolyte to the

surface of the electrode, the current reaches a plateau or exhibits a peak. Figure 1.17 shows an example of a LSV specta showing the difference of potential needed to start an oxidation/reduction reaction on an Al (0.5%Cu) and 100nm Cu dot/Al (0.5%) surface in an acidic chloride environment.

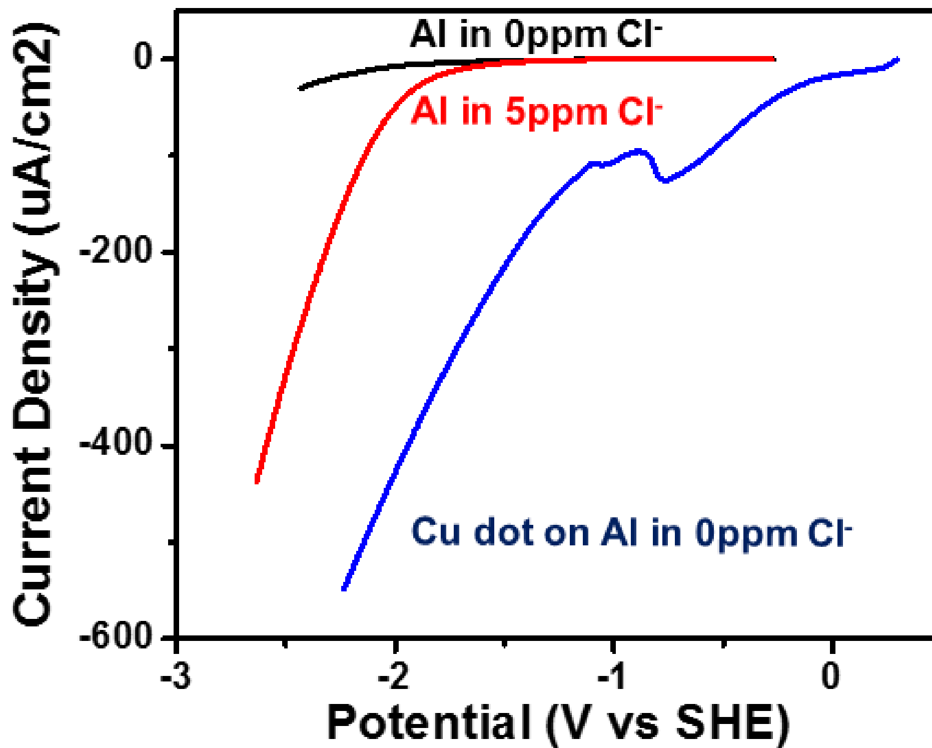

Figure 1.17: LSV with scan rate of 20 mV/s. Polarization curves were cathodic scanned from OCP and stop at potential where the cathodic current was significantly increased. Potential has been converted to SHE. LSV scan of Al (0.5%Cu), 100nm Cu dot/Al (0.5%) and Cu in pH 5 H_2SO_4 solutions.

1.10 Surface Analysis via Microscopy with Time Lapse Software.

In corrosion research it is important to have the corrosion progression and etch/corrosion rate information to define the corrosion issue. First, Immersion Corrosion Screening (ICS) was implemented with time lapse recording software. This ICS set up allows for 15 samples to be

analyzed at a time, giving an efficient method in testing and analyzing large sets at a time. Video Velocity is the time lapse software used with a web cam and a Cannan EOS Rebel T5i DSLR camera to take the optical images. An example of the web cam and DSLR set up are shown in Figure 1.18 (A&B). For an increase in magnification and resolution, a DXM 1200 Optical Microscope Nikon microscope and FEI Quanta 200 Environmental Scanning Electron Microscope (ESEM) with Energy Dispersive Spectroscopy (EDS) was used.

SEM with X-ray analysis (EDS) is considered a relatively inexpensive, time efficient, and non-destructive approach to surface analysis in order to survey surface chemistry and morphology. The surface topography and high resolution images are produced in order a focused scanning (primary) electron beam.[32] The primary electrons penetrate the surface with an energy of 0.5 – 30 kV and generates low energy secondary electrons. The surface topography of the sample determines the intensity by the amount of the secondary election and backscattered electrons. When a secondary electron leaves due to the energy from the incident beam, it leaves an electron “hole” in the inner shells and thus the atom is not in a stable state. An electron from the outer shell will drop into the inner shell to fill this hole in order to stabilize the atom. Since the outer shells are at a higher energy state, the transfer of an electron to a lower shell causes the atom to lose some energy. The energy is released in the form of X-rays. The X-rays emitted from the sample have an energy and wavelength that is characteristic of not only the parent atom but also the specific shell that lost the electron as well as the shell that replaced the lost the electron.[32]

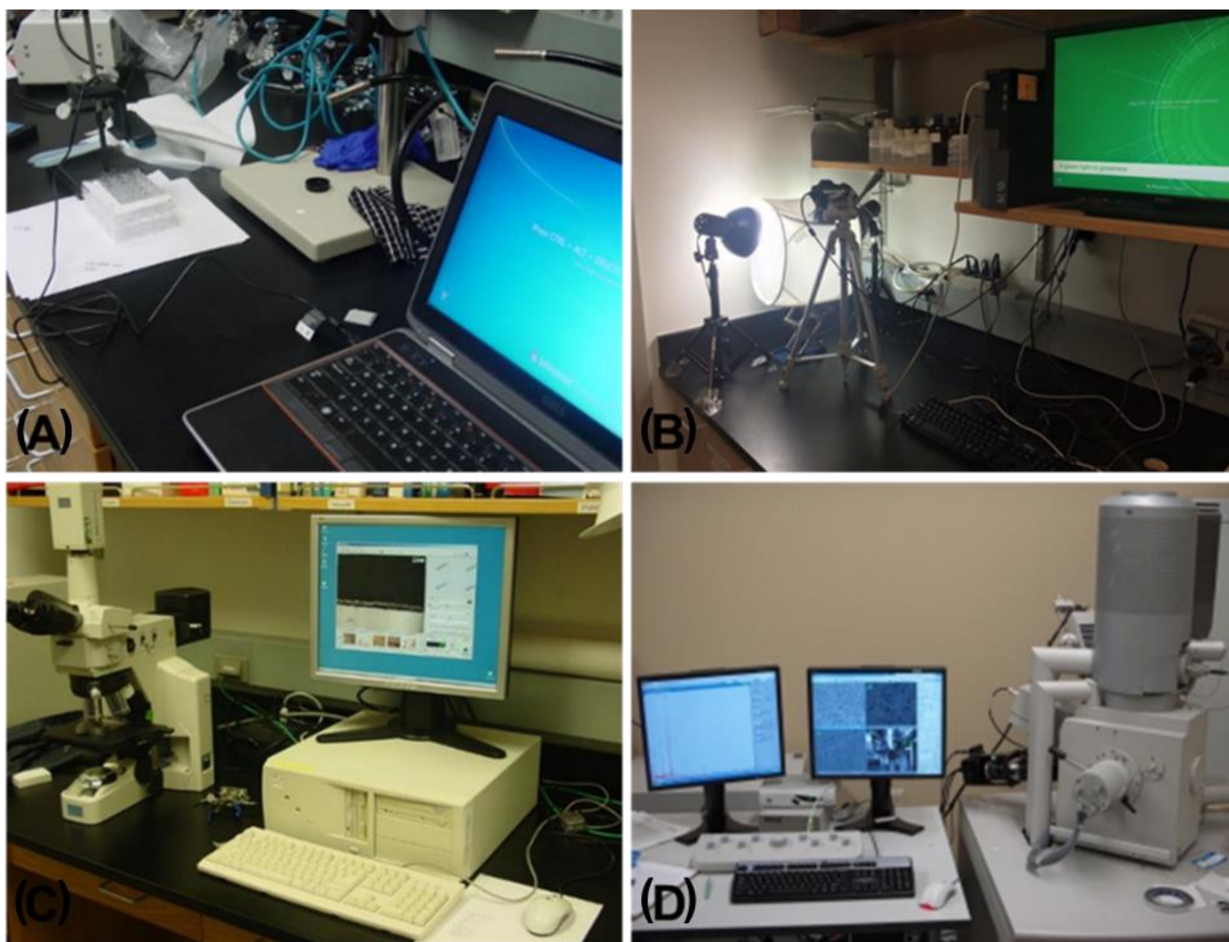

Figure 1.18: (A) 16 mega pixal web cam set up, (B) Cannan EOS Rebel T5i DSLR camera set up (C) DXM 1200 Optical Microscope Nikon microscope set up (D) FEI Quanta 200 ESEM with EDS set up.

1.11 Gas Chromatography Mass Spectrometry

The Finnegan TraceGC ultra Trace DSQ Mass Spectrometer, shown in Figure 1.19, analyzed in situ Cu dot on Al and Cu wired-bonded samples that were fully submerged in acidic chloride solution in order to detect gas by-product of corrosion. Gas chromatography-mass spectroscopy (GC-MS) is an analytical method that uses the combined separation efficiency of the GC with the detection resolution of the quadrupole detector of the MS. GC uses a carrier gas like He, Ar, H_2 or N_2 to push the sample through the capillary column. The speed in which the sample

reaches the end of the GC capillary column depends on capillary column's dimensions (diameter, length and film thickness), temperature of the GC column, and the boiling point of the sample. In a mixture, the different molecules will be separated by the difference in their chemical properties and their relative affinity for the stationary phase of the column. This difference will promote separation of the different molecules of the sample in the column.[33] The retention time is the time it takes for a molecule to reach the sample injector site at the end of the column. The end of the column is the connecting point to the MS and this difference in time allows the MS to capture, ionize, accelerate, deflect, and detect the ionized molecules separately. The MS detects the mass to charge ratio of ionized fragments of the molecules after breaking each "mother" molecule down into "daughter ions".

Figure 1.19: Finnegan TraceGC ultra Trace DSQ Mass Spectrometer used in Cu/Al bimetallic corrosion analysis.

1.12 Contact Angle Measurement

Contact angle quantifies the solid surface's wettability by a liquid, in this case ultra-pure water (UPW). UPW is made by an Integral 3 water purification system by Millipore. UPW has less than 5 ppb of organic contaminates and 18.2 MΩ reading of inorganic contaminates. Contact angle measurement is made by measuring the angle between the tangent to the droplet of liquid placed on a flat surface and the surface of the sample. Figure 1.20 is a schematic of the contact angle of a liquid droplet. The contact angle of a small drop on the surface is a function of surface free energy that is defined by the Young-Dupree equation.[34]

$$\gamma_{SG} = \gamma_{SL} + \gamma_{LG}\cos\theta \quad \text{(eq. 1.5)}$$

Where γ is the interfacial free energy, θ is the angle contact, and SG, SL and LG refer to solid-gas, solid-liquid and liquid-gas interfaces respectively. The angle of a liquid drop on the solid surface forms as a result of balance between the adhesive forces between the solid and the liquid and the cohesive forces in the liquid. When there is no interaction between the solid and the liquid, the contact angle will be 180°. As the interaction increases, the liquid spreads until the angle becomes near 0°.

Hydrophobic and hydrophilic nature of the surface can be determined using water to measure contact angle. In this dissertation, contact angle measurements were utilized to determine the hydrophobicity of the surface before and after treatments in house or at the collaborator's site.

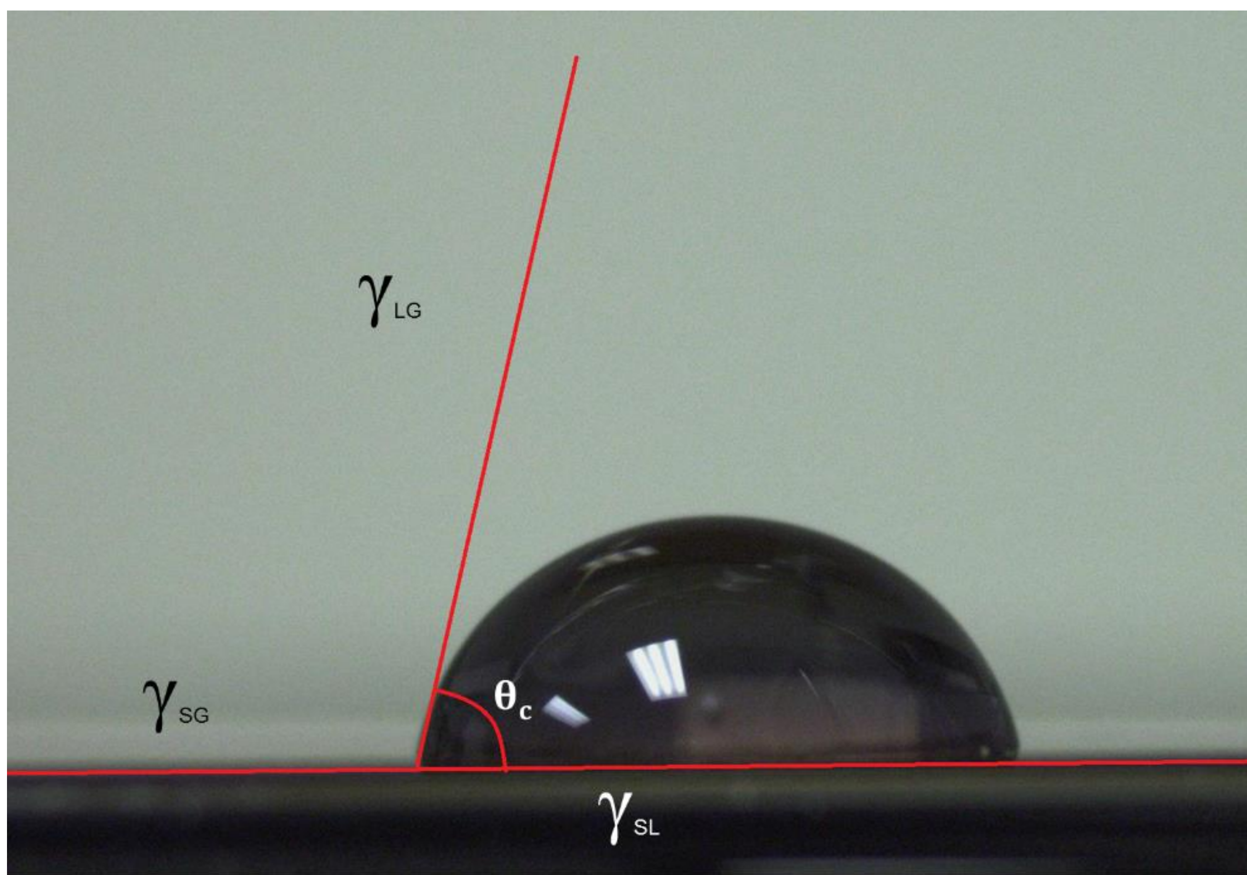

Figure 1.20: Diagram of contact angle of liquid droplet.[34]

1.13 References

1. Harrick, N. J. *Internal Reflection Spectroscopy;* John Wiley &Sons: 1967

2. Fahrenfort, J. Attenuated Total Reflection. A New Principle for the Production of Useful Infrared Reflection Spectra of Organic Compounds. *Spectrochim. Acta* **1961**, *17*, 698-709.

3. Mizaikoff, B. Waveguide-Enhanced Mid-Infrared Chem/Bio Sensors. *Chem. Soc. Rev.* **2013**, *42*, 8683-8699.

4. Guanghua, C.; Chenzhi, Z.; Fangqing, Z.; Jinlong, C.; Wei, C. ESR and IR Studies on B-Doped Hydrogenated Amorphous Silicon-Nitrogen Film. *phys. stat. sol. (a)* **1986**, *96*, K187-K189.

5. Watts, J. F.; Wolstenholme, J., Eds.; In *An introduction to surface analysis by XPS and AES;* Wiley: New York, 2003; .

6. Ebel, M. F. Absolute calibration of an X-Ray photoelectron Spectrometer. *Journal of Electron Spectroscopy and Related Phenomena* **1976***, 8*, 213.

7. Vickerman, J. C., Ed.; In *Surface Analysis - The Principal Techniques;* John Wiley & Sons: New York, 1997; .

8. Suntola, T. Chap. 14. In *Handbook of Crystal Growth*; Hurle, D. T. J., Ed.; Elsevier Science B.V.: Amsterdam 1994; Vol. 3, .

9. Leskela, M.; Ritala, M., Eds.; In *Thin Solid Films;* 2002; , pp 409-138.

10. Wang, Q. Hot-wire CVD Amorphous Si Materials for Solar Cell Application. *Thin Solid Films* **2009***, 517*, 3570-3574.

11. Zheng, W.; Gallagher, A. *Thin Solid Films* **2006***, 501*, 21.

12. Mahan, A. H. *Solar Energy Materials and Solar Cells* **2003***, 78*, 299-327.

13. Ahrenkiel, S. P.; Mahan, A. H.; Ginley, D. S.; Xu, Y. Solid-Phase Crystallization Kinetics and Grain Structure During Thermal Annealing of a-Si:H Grown by Chemical Vapor Deposition. **2001***, 176*, 972-977.

14. Xu, Y.; Nelson, B. P.; Gedvilas, L. M. Improving Narrow Bandgap a-SiGe:H Alloys Grown by Hot-Wire Chemical Vapor Deposition. *Thin Solid Films* **2003***, 430*, 197-201.

15. Schropp, B.; Stannowski, A. M.; Brockhoff, P. A. T. T.; Rath, J. K. Hot-Wire CVD of Heterogeneous and Polycrystalline Silicon Semiconducting Thin Fims for Application in Thin Film Transistors and Solar Cells. *Matter. Phys. Mech* **2000***, 1*, 73-82.

16. Chonga, S. K.; Goha, B. T.; Aspanuta, Z.; Muhamada, M. R. Effect of substrate temperature on gold-catalyzed silicon nanostructures growth by hot-wire chemical vapor deposition (HWCVD) . *Appl. Surf. Sci.* **2011***, 257*, 3320-3324.

17. Behrisch, R., Ed.; In *Sputtering by Partical Bombardment;* Berlin, Ed.; Springer: 1981; .

18. Ohring, M., Ed.; In *Materials Science of Thin Films;* 2nd ed. Academic Press: , pp 215.

19. Yu, K. K.; Pillai, K. S.; Nalla, P. R.; Chyan, O. Study of bimetallic corrosion related to Cu interconnects using micropattern corrosion screening method and Tafel plots. *J. Appl. Electrochem.* **2010***, 40*, 143-149.

20. Goswami, A.; Koskey, S.; Mukherjee, T.; Chyan, O. Study of Pyrazole as Copper Corrosion Inhibitor in Alkaline Post Chemical Mechanical Polishing Cleaning Solution. *ECS Journal of Solid State Science and Technology* **2014**, *3*, P293-P297.

21. Bard, A. J.; Faulkner, L. R., Eds.; In *Electrochemical Methods: fundamentals and applications. 2nd ed;* John Wiley and Sons: New York, 2001; , pp 725.

22. Jones, D. A., Ed.; In *Principles and Prevention of Corrosion;* Upper Saddle River, Ed.; Pretice Hall: 1996; .

23. Shreir, L. L.; Jarman, R. A.; Burstein, G. T. *Corrosion* **1994**.

24. Popova, S. N.; Popov, B. N.; White, R. E. *Corrosion* **1990**, *46*, 1007.

25. Tsuru, T.; Haruyama, S. *Boshoku Gijustsu* **1978**, *27*, 573.

26. Jones, D. A. *Corros. Sci.* **1968**, *8*, 19.

27. Ambat, R.; Jensen, S. G.; Mo/ller, P. Corrosion Reliability of Electronic Systems. *ECS Transactions* **2008**, *6*, 17-28.

28. Kim, H.; Lee, J.; Koh, K.; Won, J.; Chpe, S.; Lee, J.; Moon, J.; Park, Y. Effects of Cu/Al Intermetallics Compound (IMC) on Copper Wire and Aluminum Pad Bondability. *IEEE Trans. Comp and Pack. Tech* **2003**, *26*, 367-374-2.

29. Uno, T. Bond reliability under humid environment for coated copper wire and bare copper wire. *Microelectronics Reliability* **2011**, *51*, 148-156.

30. Trethewey, K. R.; Chamberlain, J. *Corrosion For Students of Science and Engineering;* John Wiley & Sons: New York, NY 10158, 1988; , pp 382.

31. Faulkner, L. R. *J. Chem. Ed.* **1983**, *60*, 262.

32. Skoog, D. A.; Leary, J. J., Eds.; In *Principles of Instrumental Analysis;* Saunders College Publishing: 1992; Vol. 4th, pp 700.

33. Skoog, Douglas A., Holler, F. James., Crouch,Stanley R., *Principles of instrumental analysis;* Brooks/Cole : Thomson Learning: Australia, 2007; .

34. Chow, T. S. *J. Phys. : Condens. Matter* **1998**, *10*, L445.

CHAPTER 2

CHEMICAL BONDING CHARACTERIZATION OF BORON DOPED HYDROGENATED AMORPHOUS SILICON FILMS VIA MULTIPLE INTERNAL REFLECTANCE INFRARED SPECTROSCOPY*

2.1 Introduction to Hydrogenated Amorphous Silicon Films

Crystalline silicon (*c*-Si) films have silicon atoms in a well ordered crystal lattice with a tetrahedral structure that continues over a large range, Figure 2.1(A). Amorphous silicon (*a*-Si) is defined by the absence of an ordered crystal lattice. In *a*-Si the silicon atoms form a continuous random network where there is no long range order, Figure 2.1(B).[1]

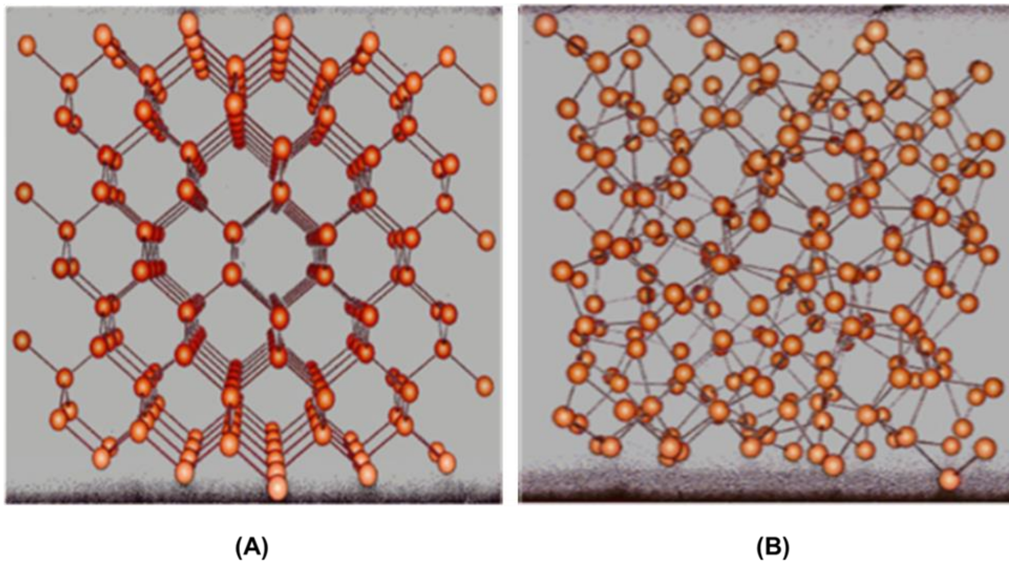

Figure 2.1: (A) Crystalline structure. (B) Amorphous structure.[1,2]

---

*This chapter is presented in its entirety from N. Ross, K. Shrestha, O. Chyan, C. L Littler, V. C. Lopes and A. J. Syllaios. “Characterization of Boron Doped Amorphous Silicon Films by Multiple Internal Reflection Infrared Spectroscopy.” MRS Online Proceedings Library, 2013, 6, with the permission from the Cambridge University Press.

A-Si films are not completely disordered. For example, the covalent bonds between the silicon atoms are similar to *c*-Si, with the same average bond lengths, bond angles, and number of neighbors. The disorder of *a*-Si films is represented by the probability of finding an atom at a distance R from another atom. The structural order of a crystalline, amorphous and gaseous phases are displayed in Figure 2.2.[1]

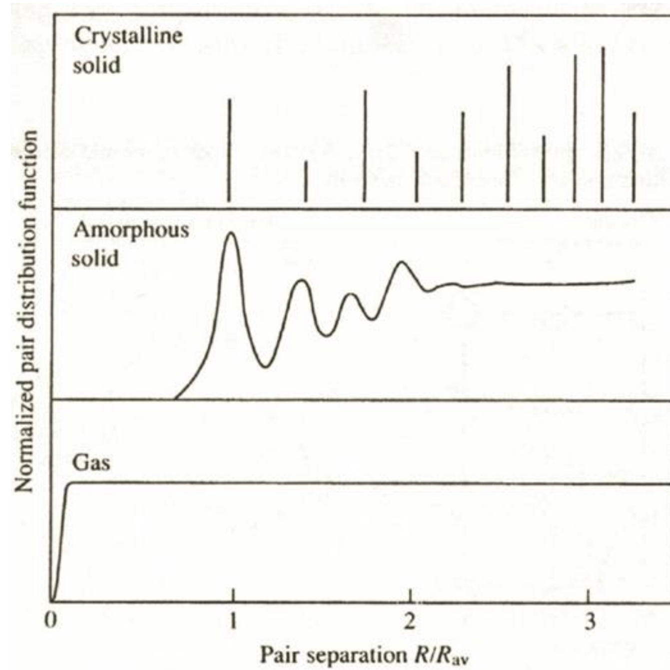

Figure 2.2: Diagram of the atom pair distribution for crystalline, amorphous solid, and gas phases, showing the difference in average separation of the nearest neighboring atom (R_{av}).[1]

In *a*-Si films, not all of the Si atoms are bonded to four neighboring silicon atoms, causing some atoms to have a dangling bond. The dangling bonds are usually considered physical defects in the random silicon network and may cause anomalous electrical behavior. Amorphous silicon can be passivated by hydrogen, which bonds to the dangling bonds and reduces the dangling bond density by about four orders of magnitude. This passivation of dangling bonds with hydrogen

brings the hydrogenated amorphous silicon (*a*-Si:H) film to be used within devices such as solar cells.[1]

a-Si:H films have certain properties such as high band gap energy, low leakage current, and high optical absorption.[1] This enables *a*-Si:H to be applied in a broad range of applications and technology base. *a*-Si:H has the advantage in development because *a*-Si:H can be made thinner and can be deposited over larger areas by plasma enhanced chemical vapor deposition (PECVD) compared to *c*-Si. This allows for *a*-Si to be a more cost effective film than *c*-Si. Another advantage of *a*-Si is that it can be deposited at relatively low temperatures (>200ºC), allowing for simple deposition on glass, metal or plastic substrates. These useful characteristics make *a*-Si an ideal candidate for flexible electronics, roll to roll capability and deposition on already made devices. *a*-Si:H is also used in photo-voltanics, thin film transistors (TFT) for active matrix liquid crystal displays, multi-junction solar cells, metamaterials, large area imaging arrays, micro electro mechanical systems (MEMS) based sensors, and uncooled microbolometer infrared imaging arrays.[1] *a*-Si:H films studied in this chapter are made for hand held and helmet mounted uncooled microbolometers, also known as infrared cameras.

2.2 Introduction to Microbolometer

Boron-doped hydrogenated amorphous silicon (*a*-Si:H(B)) is a material of choice for microbolometer infrared detector array technology due to its high temperature coefficient of resistance (TCR), relatively high optical absorption coefficient and low cost. *A*-Si material does not need to be cooled by a cooling systems like liquid nitrogen, which makes *a*-Si more portable than microbolometer infrared detector based on mercury cadmium telluride (MCT) detectors.[3]

These qualities make *a*-Si:H(B) an ideal material for hand-held and helmet mounted infrared cameras for military and law enforcement personnel. Extensive characterization has been carried out on the effects of PECVD growth conditions on optical and electrical properties of *a*-Si:H films.[1,3-5] However, the chemical bonding structure is less studied.

MIR-IR spectroscopy was used to observe bonding grown by PECVD at varying substrate temperatures, hydrogen dilution of the silane precursor and dopant to silane ratio. The ideal amorphous silicon material for hand-held microbolometer applications is protocrystalline-Si:H which has a Si lattice that is as ordered as possible without any formation of microcrystals. To reach the protocrystalline-Si:H area, one must have careful control of several factors such as of hydrogen dilution, substrate temperature, RF power and frequency of PECVD.[6] Figure 2.3 displays the protocrystalline-Si:H at the blue dotted line starting at the arrow that says "best *a*-Si:H". Notice how the blue dotted line is in the area closest to the microcrystalline crystals but not in the area where crystals are present. The boron doped hydrogenated amorphous silicon (*a*-Si:H(B)) films in this report are about 500 angstrom in thickness. Thus the general hypothesis according to Collins et al.[6] for 500 angstrom thick *a*-Si:H films would be around 60:1 [H_2]/[SiH_4]. However the investigative research proved information that boron doping has an inverse relationship to hydrogen dilution in film development, which is discussed in sections 2.4 to 2.6.

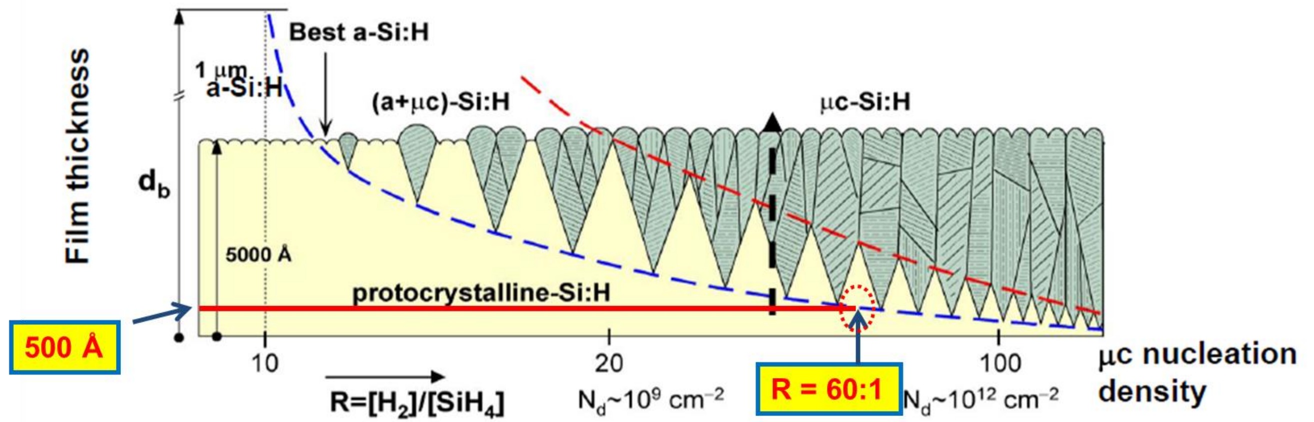

Figure 2.3: Amorphous, micro-crystalline and crystalline silicon in terms of film thickness and hydrogen dilution $[H_2]/[SiH_4]$.[6]

Optical and electrical properties have been studied on these films by collaborators, and chemical bonding characterization was done via IS50 fourier transform infrared spectroscopy (FTIR). In this study, MIR-IR spectroscopy helped guide the development of *a*-Si:H(B) films for microbolometers. The multiple sampling enabled by more than 80 total internal reflections greatly enhances the measuring sensitivity of MIR-IR technique, Figure 2.4.[7] MIR-IR is an analytical tool well suited for this task due to the over 100x increase sensitivity versus normal transmission infrared spectroscopy shown in Figure 2.5. For example, MIR-IR was previously utilized to monitor hydrogen passivation on Si<100> surface with sub-monolayer measuring sensitivity.[7] This increase in sensitivity detected previously unseen chemical bonds and changes in intensity in response to for the change of a processing variable. What gives this metrology its unique advantage in the scientific community is that the films deposited on silicon wafers are fashioned into attenuated total reflection (ATR) waveguides. This gives better repeatability in measurements, and with proper background subtraction, it makes the MIR-IR metrology capable of analyzing the surface chemistry. In Figure 2.4, d_p is the penetration depth of the evanescent wave, n_p is the

refractive index of the crystal, Θ is the angle of incidence, n_s is the refraction index of the sample area, and n_{sp} is the ratio between n_s/n_p.

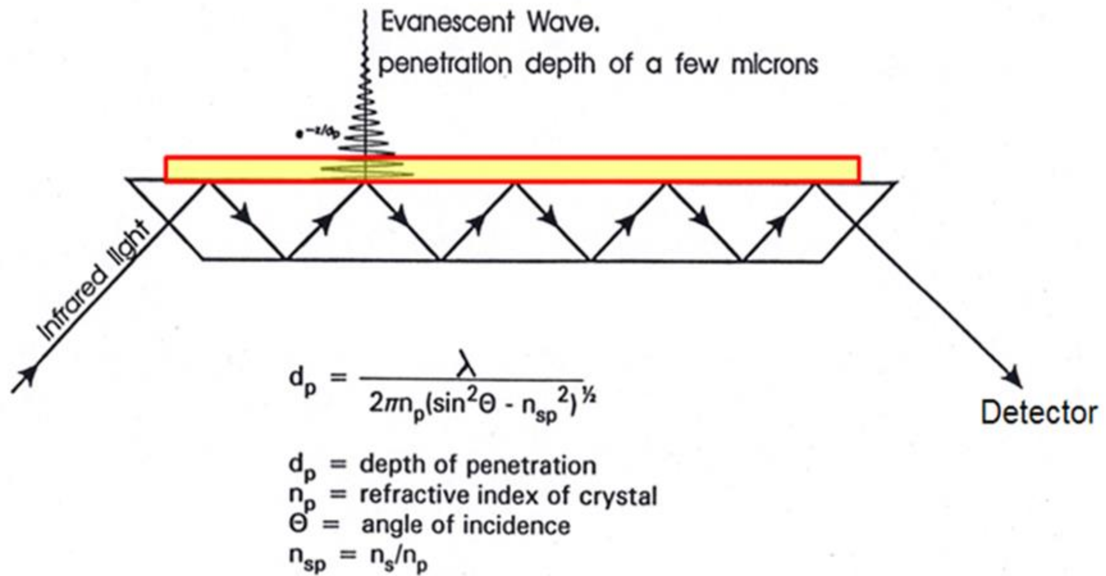

Figure 2.4: Attenuated total reflectance (ATR) wave guide for FT-IR analysis.[8]

The infrared absorption spectra (MIR-IR and TIR) of the same *a*-Si:H thin film sample grown over Si_xN_y:H coated Si<100> substrate are shown in Figure 2.5. The difference in sensitivity of MIR-IR versus TIR is an over 100x increase. The MIR-IR spectrum in Figure 2.5 reveals well-resolved IR absorption peaks associated with Si-H (1989 cm^{-1}) and B-H (2465 cm^{-1}) bonding modes originated from *a*-Si:H thin film.[9] The observed infrared absorption peaks of N-H (3340 cm^{-1}) and SiH_x (2000 cm^{-1}) bonding modes can be assigned to the underlying Si_xN_y:H layer on Si<100> substrate.

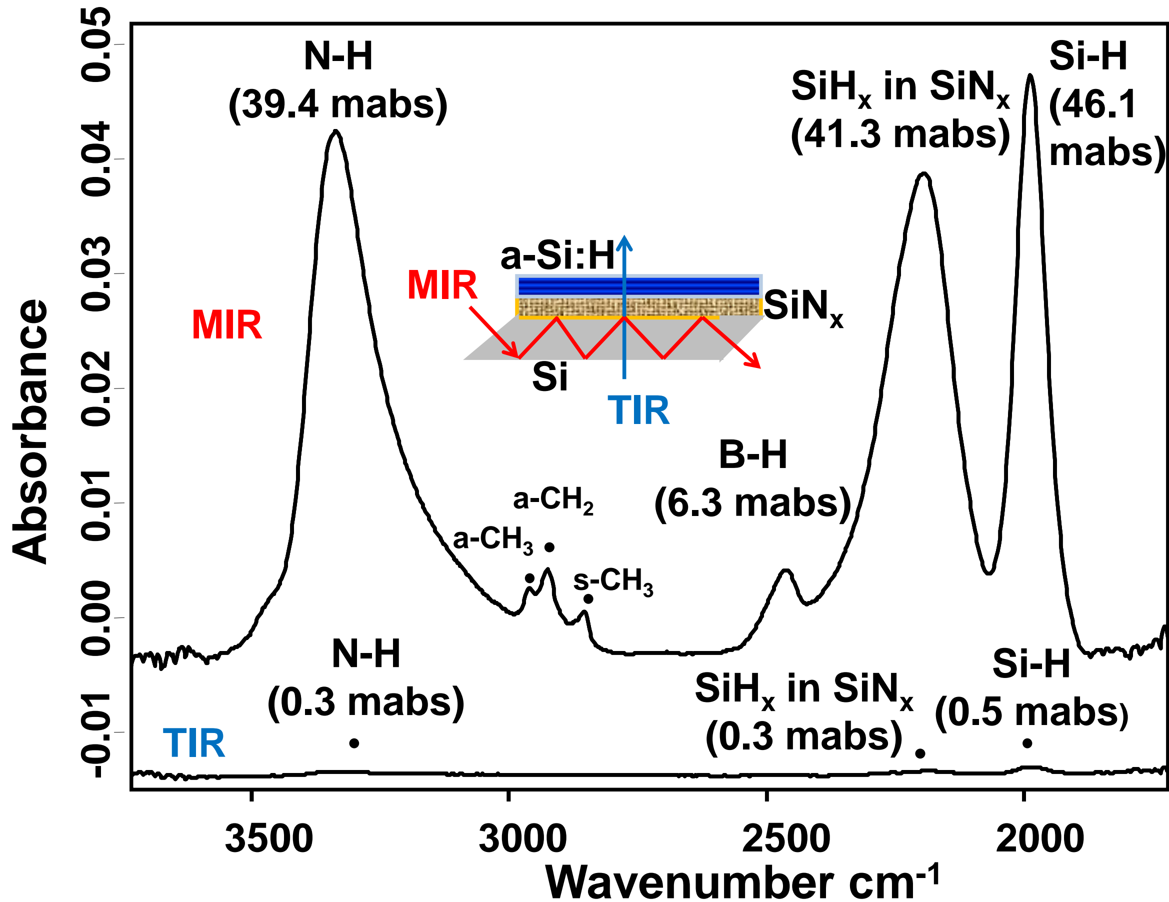

Figure 2.5: MIR-IR (top) and TIR (bottom) spectra of a 50 nm *a*-Si:H thin film deposited on Si_xN_y:H.

MIR-IR metrology is well suited for the task of providing chemical bonding information of *a*-Si:H(B) films due to the fact that the main chemical bonds for *a*-Si:H(B) are located in MIR-IR's main detection range, Figure 2.6 (A). MIR-IR's main range is in the 4000cm^{-1} to 1600cm^{-1}. The type of film the collaborators are looking for is a protocrystalline-Si:H film with a low disorganized ratio ($[SiH_2]_n/([SiH]+[SiH_2]_n)$) using values from Si-$H_2$ and Si-H peak height. An example of this protocrystalline-Si:H film is displayed in Figure 2.6 (B) which is an a-Si:H(B) film with a $[SiH_2]_n/([SiH]+[SiH_2]_n)$ ratio equal to 0.073. A key concept for an *a*-Si:H film is that it is organized maximally without crystallinity and it will have the most silicon atoms in the Si_3-**Si-H** configuration. When silicon atoms get into the Si_4-Si configuration, microcrystals start to form

within the film, and the film is no longer a protocrystalline-Si:H film. Weak links such as Si_2-**Si-H**$_2$ will decrease the organization of the film, and thus the film is no longer protocrystalline-Si:H film. Most of the existing characterization metrology cannot provide a clear bonding picture of a-Si:H thin films. MIR-IR is well suited to analyze Si-H, Si-H_2, O-Si-H_x, and Si-B bonding peaks in order to study the *a*-Si:H(B) films at the chemical bonding level.

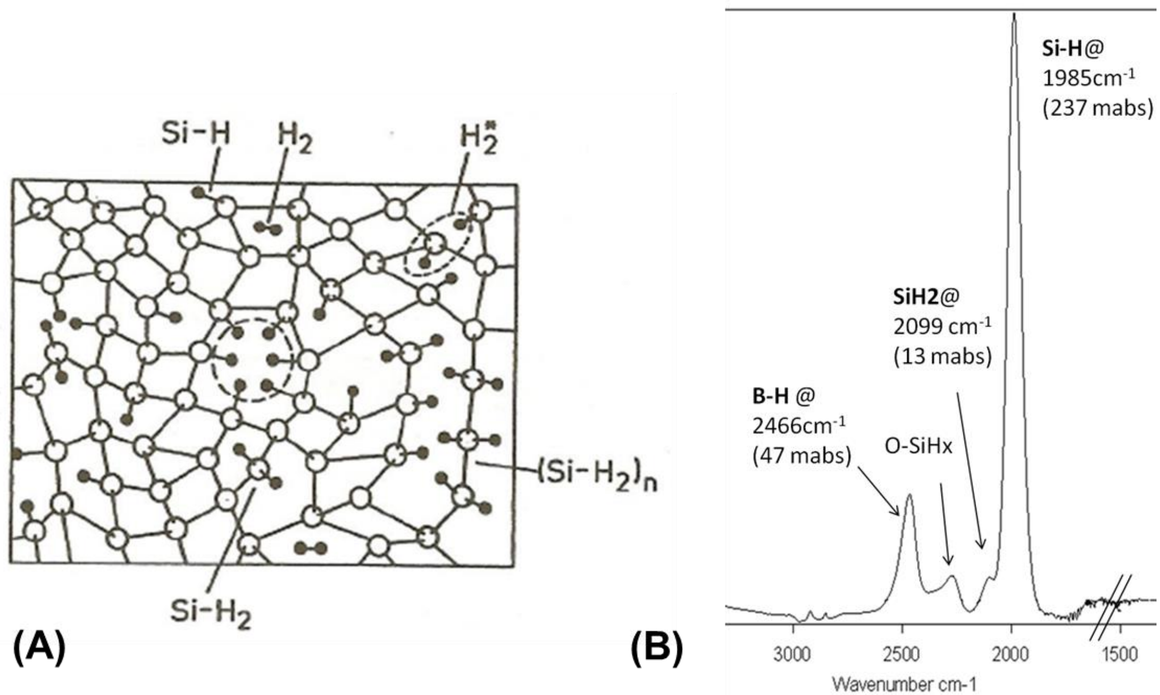

Figure 2.6: Hydrogenated amorphous silicon structure example with the main chemical bonds with an example MIR-IR spectra for reference.[10]

2.3 Experimental Information

Samples of *a*-Si:H thin films were grown in a PECVD system using capacitively coupled 13.56 MHz plasmas with the substrate on the ground electrode. Source gases for p-type *a*-Si:H growth were silane (SiH_4) gas, hydrogen (H_2) gas, argon gas and boron trichloride (BCl_3) gas. The flow rate ratio of boron to silane, defined as "r" = $[BCl_3]/[SiH_4]$, and hydrogen dilution to silane

ratio "R_H"=$[H_2]/[SiH_4]$, were varied to produce films with differing hydrogen and boron concentrations. The samples reported here were grown at R_H values ranging from 16 to 100 and "r" values ranging from 0.02 to 0.32. MIR-IR was used to characterize the chemical bonding structure differences due to variation of H dilution and B doping during PECVD deposition. MIR-IR utilizes the silicon wafer itself as an IR waveguide for attenuated total reflection (ATR) to achieve sub monolayer detection sensitivity.[11] A favorable difference of refractive indices of the Si wafer and its air interface enables multiple total internal reflections (ca. 80 reflections from a 60 mm Si ATR crystal), which greatly enhances IR measuring sensitivity. The *a*-Si:H (ca. 50 nm) coated silicon wafers were fabricated on to an ATR optical element (60 x 10 x 0.7 mm, 45° bevel angle) by mechanical polishing.[11] For Si<100> background ATR coupons, NH_4OH (28%) H_2O_2 (30%) and dionized water in a 1:1:5 ratio at 70ºC (SC1) solution were used to remove any organic contamination from the surface followed by etching in 0.5% HF solution. IR spectra were recorded on a Nicolet IS 50 FTIR spectrometer and was constantly purged under dry air ($CO_2 < 1$ ppm). Both transmission (TIR) and MIR-IR infrared spectra were measured. An average of 100 individual spectra were collected at 2 cm^{-1} resolution. The detection limit of MIR-IR is ca. 0.2 mabs with an error margin of < 3%.

2.4 Hydrogen dilution and Boron Doping Effect on a-Si:H(B) Deposited on Si_xN_y:H Substrate

Effects of boron doping ratio and hydrogen dilution growth parameters on PECVD *a*-Si:H thin film were studied by MIR-IR. Figure 2.7 (A & B) are MIR-IR spectra of 50nm thick *a*-Si:H(B)/SiN/Si sample with an increase in the boron doping ratio ($[BCl_3]/[SiH_4]$) that results in a continued, but more pronounced decrease of SiH bonds displayed in Figure 2.7(A & C). In Figure 2.7(A & C), when the hydrogen dilution ratio ($[H_2]/[SiH_4]$) is increased in the boron doped a-Si:H

deposition process, there is an increase in Si-H bond formation and a decrease in the B-H bond formation.

In section 2.2, a hypothesis was made that an *a*-Si:H film at 500 angstrom thickness with 60:1 hydrogen dilution would produce an a-Si:H film at the protocrystalline line. However, the a-Si:H needs to be doped by boron to increase the conductivity of the a-Si:H film to provide a more responsive microbolometer chip. The boron doping will increase the $[SiH_2]_n/([SiH]+[SiH_2]_n)$ ratio, thus the hydrogen dilution needs to be increased further to reach the protocrystalline area. More fine tuning needs to be done at this point.

Two examples of fine tuning of *a*-Si:H(B) via MIR-IR are shown in Figure 2.7 (A&B). Figure 2.7 displays a 500nm thick *a*-Si:H(B) / silicon nitride / silicon oxide sample with a varying boron concentration ([BCl3] / [SiH4]) in Figure 2.7 (A) and hydrogen dilution ([H2]/[SiH4]) in Figure 2.7 (B). The N-H (3340 cm^{-1}) and SiH_x (2000 cm^{-1}) infrared absorption peaks are from underlying substrate Si_xN_y:H. N-H and SiH_x remain constant as the hydrogen dilution and boron concentration is increased in Figure 2.7 (A&B). Figure 2.7 (C&D) displays peak height values of Si-H (1990cm^{-1}) and B-H (2465cm^{-1}) from Figure 2.7 (A&B). There is an inverse relationship between Si-H and B-H peak height when there is an increase in boron concentration and hydrogen dilution. However, it is difficult to quantitatively determine to what degree each variable effects the *a*-Si:H(B) film due to the fact that N-H and SiH_x over shadows the important peaks associated with the *a*-Si:H(B) film. A new sample set without the silicon nitride layer is needed to proceed with guiding *a*-Si:H(B) film development.

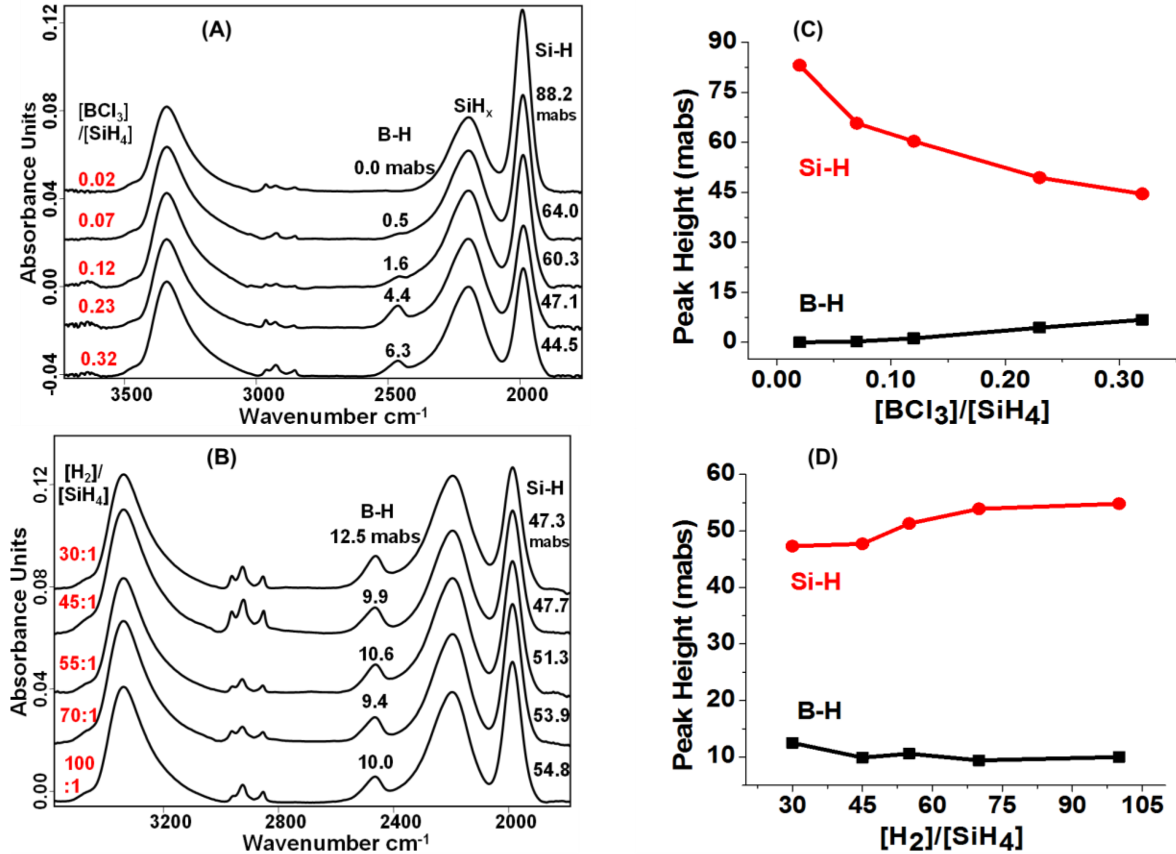

Figure 2.7: MIR-IR spectra of 50 nm *a*-Si:H thin films deposited with different PECVD grown parameters (A) boron doping [BCl_3]/[SiH_4] ratio 0.02 to 0.32, (B) hydrogen dilution [H_2]/[SiH_4] ratio 30:1 to 100:1. (C) Si-H (1990cm^{-1}) and B-H (2465cm^{-1}) peak height values from Figure 2.7 (A). (D) Si-H (1990cm^{-1}) and B-H (2465cm^{-1}) peak height values from Figure 2.7 (B).

2.5 Silicon Nitrogen Layer Removal

As shown in Figure 2.7, the underlying Si_xN_y:H layer exhibits a strong SiH_x absorption peak centered at 2000 cm^{-1} that can mask the important chemical bonding information of PECVD *a*-Si:H film. To examine the IR absorption at the region of 1800-2400 cm^{-1} more closely, *a*-Si:H thin films were deposited directly on Si<100> substrate. As Figure 2.8 shows, by removing the Si_xN_y:H layer, two additional IR peaks at 2105 cm^{-1} and 2260 cm^{-1} were observed on *a*-Si:H(B) thin film, and there peaks can be assigned to SiH_2 and O-SiH_x bonding modes respectively.[12] Having the correct background correction so that the IR spectra is only detecting the surface layer

in question is important. Without correct background correction, peaks can be changed and even hidden from detection.

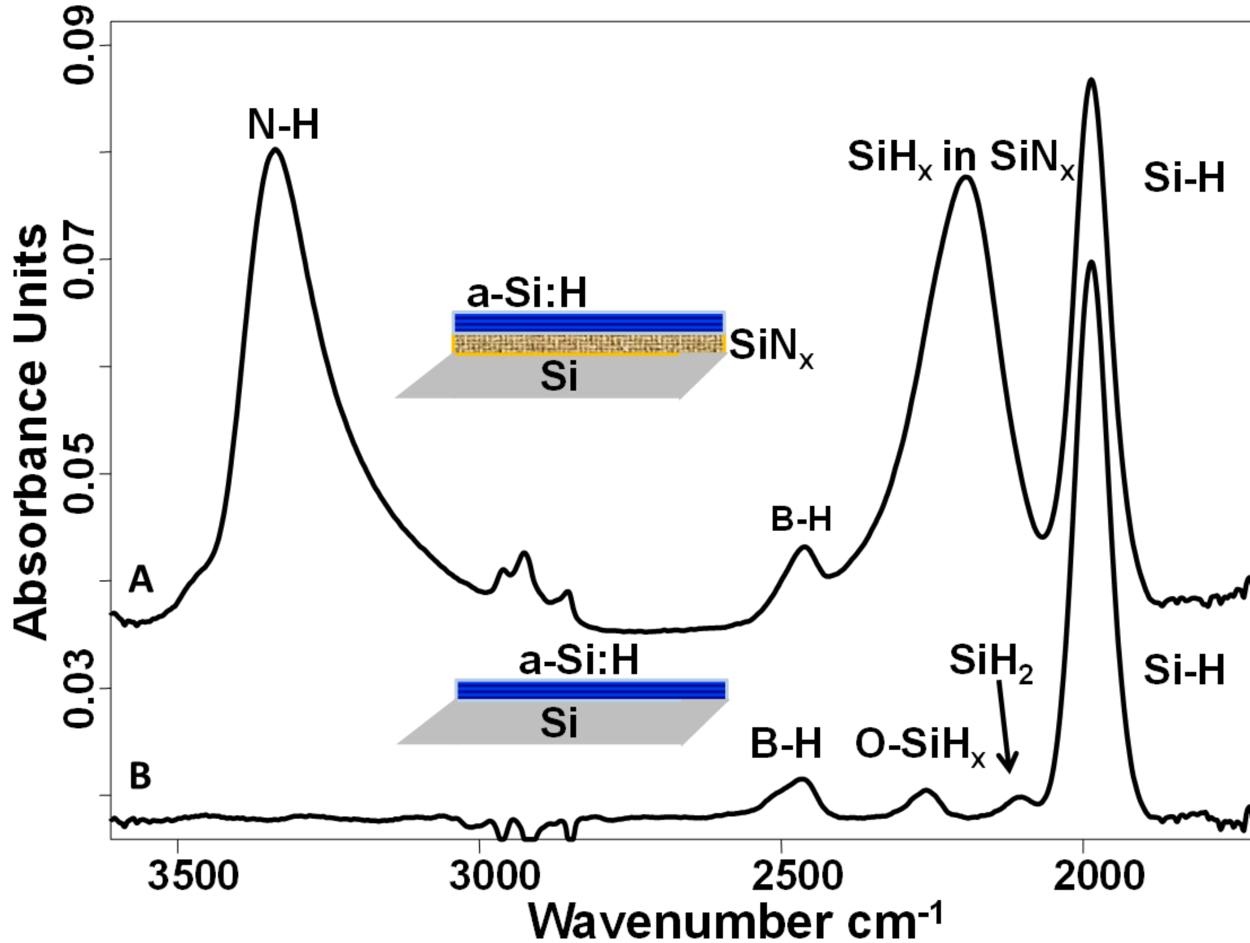

Figure 2.8: MIR-IR spectra of an *a*-Si:H thin film (A) with a Si_xN_y:H underlying layer (B) without a Si_xN_y:H underlying layer to reveal important SiH_2 and O-SiH_x peaks of *a*-Si:H .

2.6 Hydrogen Dilution and Boron Doping Effect on a-Si:H(B) Film

Effects of varying doping ratio and hydrogen dilution on *a*-Si:H thin film deposited on Si<100> substrate were also studied by MIR-IR. With the removal of the Si_xN_y:H layer, an interesting trend with SiH_2 peak was found. Figure 2.9 & 2.10 confirm that an interesting counter-balance relationship exists between boron-doping and hydrogen-dilution growth parameters in

PECVD-grown *a*-Si:H. Specifically, an increase in the hydrogen dilution ratio causes an increase in the Si-H bonding and a decrease in the B-H and SiH_2 bonding. In comparison, an increase in Boron doping ratio results in the increase of B-H and SiH_2 bonding and decrease of Si-H bonding mode. Hydrogen dilution displays an increase in organization of the a-Si:H(B) whereas boron concentration has the opposite effect by making the a-Si:H(B) less organized. This is a key finding since the goal of this project is to guide the development of *a*-Si:H(B) films to be organized maximally without crystallinity.

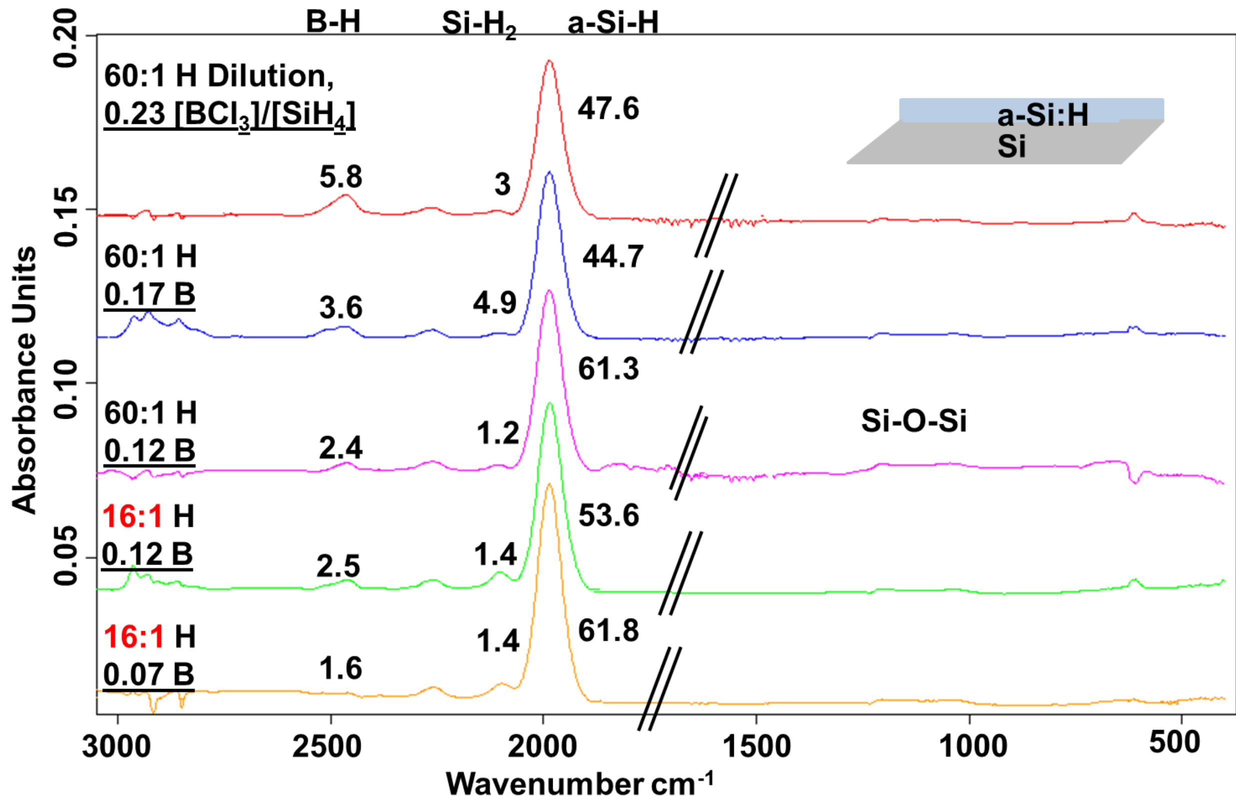

Figure 2.9: MIR-IR spectra set of an *a*-Si:H(B) thin film verifying in boron concentration and hydrogen dilution.

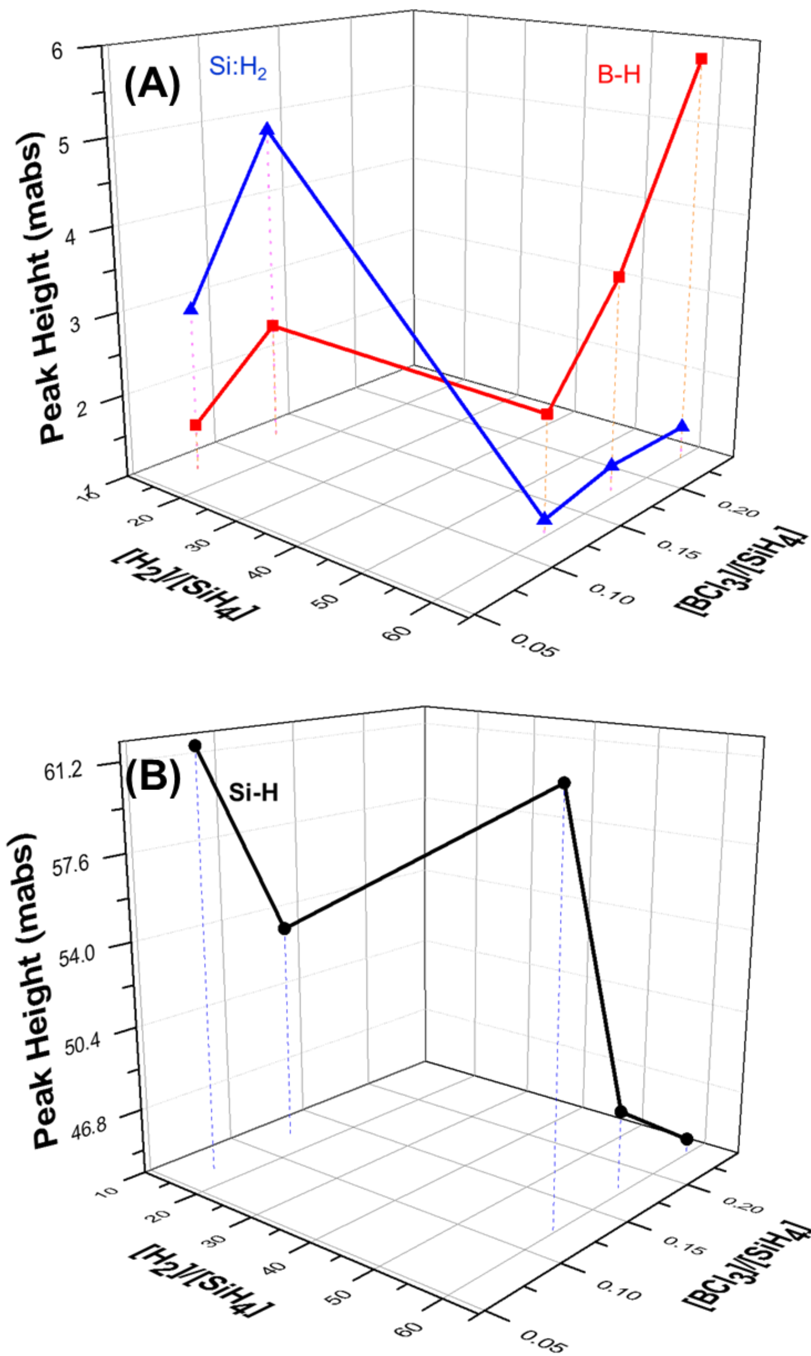

Figure 2.10: Effects of PECVD grown parameters of boron doping $[BCl_3]/[SiH_4]$ ratio and hydrogen dilution $[H_2]/[SiH_4]$ ratio on IR absorption peaks heights of (A) B-H and SiH_2 and (B) Si-H peak heights in *a*-Si:H thin films.

The removal of the silicon nitride layer was proven to aid in the detection of Si-H, SiH_2, and B-H peaks associated with *a*-Si:H(B) film in Figure 2.10. The effects of varying boron doping ratio and hydrogen dilution growth parameters on PECVD *a*-Si:H thin film were continually fine-tuned guided by MIR-IR chemical bonding mapping in order to closer reach the polycrystalline-Si:H. In Figure 2.11 the inverse relationship between hydrogen dilution and boron concentration is still present. Two examples of fine tuning of *a*-Si:H(B) via MIR-IR is shown in Figure 2.11 (A&B). Figure 2.7 displays 500nm thick *a*-Si:H(B) / silicon oxide sample with varying boron concentration ($[BCl_3]$ / $[SiH_4]$) in Figure 2.11 (A) and hydrogen dilution ($[H_2]/[SiH_4]$) in Figure 2.11 (B). Figure 2.11 (C&D) displays Si-H (1990cm^{-1}) and B-H (2465cm^{-1}) peak height values from Figure 2.11 (A&B). There is an inverse relationship between Si-H and B-H peak height when there is an increase in boron concentration and hydrogen dilution.

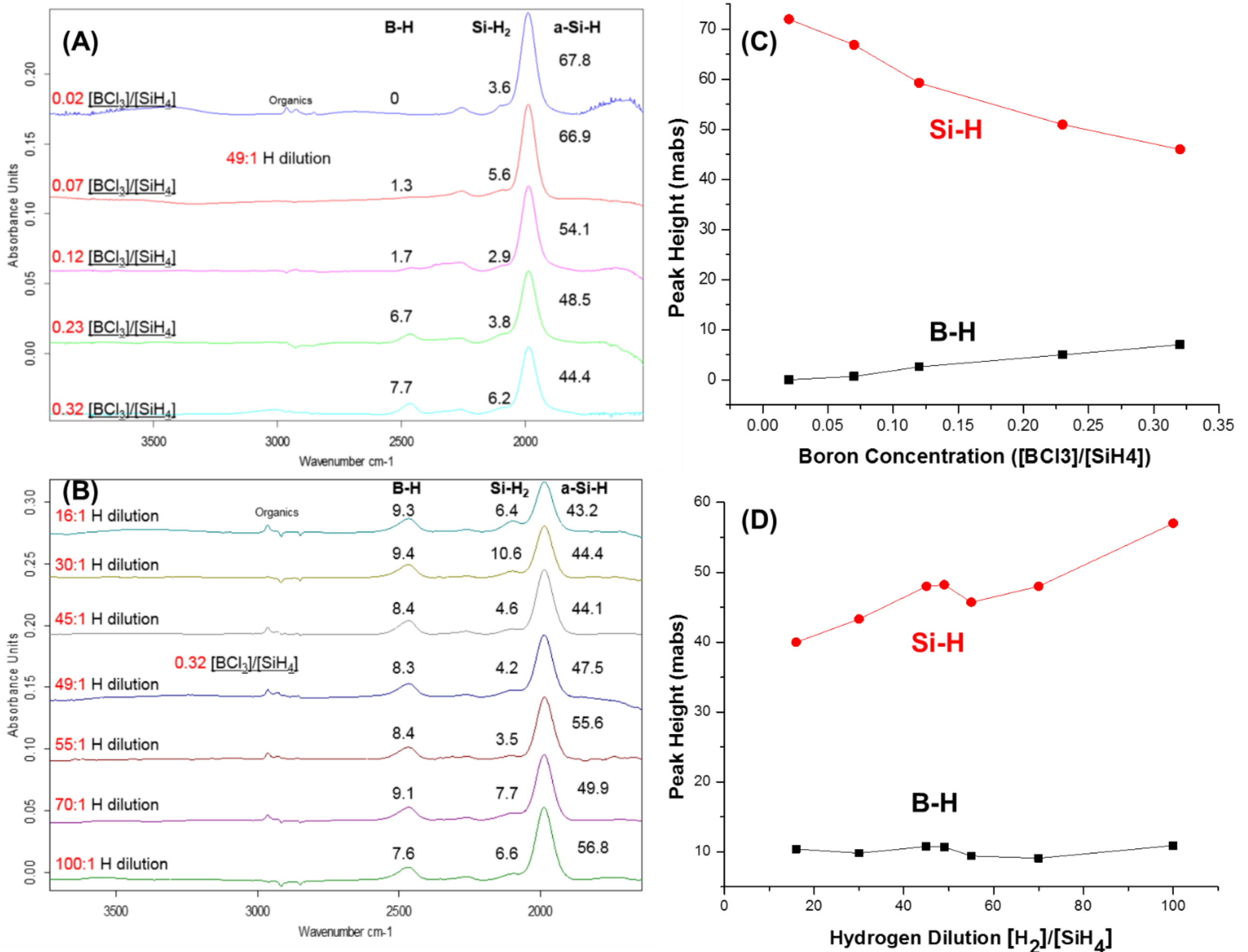

Figure 2.11: MIR-IR spectra set of an *a*-Si:H thin film varying in (A) boron concentration and (B) hydrogen dilution. (C) Si-H and B-H peak height values from Figure 2.11 (A). (D) Si-H and B-H peak height values from Figure 2.11 (B).

2.7 Deposition Condition Effects on Chemical Bonding Structure

PECVD process to deposit *a*-Si:H uses precursors of silane and hydrogen gas and produces fragments such as Si, and H radicals. Electron energies in the plasma have a Maxellian distribution in the 0.1-20 eV range. This energy is high enough to excite molecules or break chemical bonds at the depositing film. The chemical bonding energy for a H-H bond is 432 KJ/mol and 393 KJ/mol in a Si-H bond which makes a hydrogen radical more favorable to bind with another hydrogen

radical, rather than with a silicon radical.[13] When hydrogen dilution is increased there is more H radicals present to take up the hydrogen atoms released from silane radicals. Thus there is a competition between silicon radicals from silane and hydrogen radicals from silane as well as hydrogen gas. It is a simple dilution issue. SiH_3, SiH_2^2, Si_2H_2, SiH_3, and Si_4 radicals will stay as gas until enough Si-Si bonds are made for them to precipitate out of gaseous form on to sample to produce *a*-Si film. Free H radicals will be quickly taken up by other H radicals, and this process will be more likely due to the high dilution of hydrogen gas.

MIR-IR reveals four IR-active bonding modes including B-H, O-SiHx, SiH_2 and Si-H in the 50 nm *a*-Si:H thin film grown by PECVD. An interesting counter-balance relationship between boron-doping and hydrogen-dilution growth parameters was consistently observed in all *a*-Si:H films deposited on Si_xN_y:H or Si<100>. A simplistic explanation can be described as there is a competition between B and Si toward H during PECVD growth process. Based on bond energy calculations, B-H (389 KJ/mole) is more energetically favorable than Si-H (318 KJ/mole).[13] Our MIR-IR data, Figures 2.7 & 2.11, show that an increase in boron-doping ratio gives a more pronounced decrease of Si-H bonds and steady increase of B-H bonds. However, PECVD growth process involves energetic ions, reactive radicals and neutral moieties from precursors that interact with a constantly evolving surface with various active sites. More observation and work is needed to give a reliable account of this counter-balanced relationship. On the other hand, optimization of boron doping in *a*-Si:H films to achieve proper balance between temperature coefficient of resistance and conductivity is critically important for the infrared microbolometer imaging application. Our MIR-IR data brings new insights toward better understanding of the detailed B-doping mechanism.

It is well known that experimentally observed boron doping in *a*-Si is relatively low (ca. 10%) as compared to *c*-Si (ca. 90%).[1] The repeating crystal structure in *c*-Si favors boron atoms to assume the fourfold configuration as its surrounding *c*-Si lattice. The resulting substitutional boron doping provides mobile hole carriers to shift the Fermi-level and achieve active doping. However, relaxation effects in the amorphous matrix can significantly reduce the dominance of the fourfold substitutional doping. Several hypotheses have been proposed for explaining the cause of low doping efficiency of boron in *a*-Si and *a*-Si:H. Most of boron could be incorporated into threefold coordinate sites that are inert and non-doping.[1] In addition, localized midgap states commonly associated with dangling bonds as well as tail states in the valence and conduction bands could contribute to the non-active boron doping configuration.[14] Recently, Santos et al. used *ab initio* simulations to propose the presence of intrinsic hole traps associated with highly distorted angles in the amorphous matrix.[14] Consequently, even the substitutional boron doping in fourfold configuration can lose its hole carriers to these hole traps nearby. Hydrogen is the key compositional ingredient of *a*-Si:H and has been associated with the inactive boron doping. Boyce and Ready[15] used nuclear magnetic resonance spectroscopy (NMR) measurements to show one-half of all boron atoms have neighboring H atoms about 1.4 Å away, and suggested hydrogen passivation on boron is the likely cause of non-active boron doping. Fedders and Drabold proposed, based on simulation, that B(3,1) (a boron atom with three Si and one H neighbors) is the most favorable doping configuration energetically.[16] They also proposed that B-H pair formation, similar to *c*-Si, could disable the boron doping in *a*-Si:H by inserting a H atom between a boron atom and one of its Si nearest neighbors.

Our MIR-IR analyses reveal detailed chemical bonding characteristics of boron doped *a*-Si:H thin film to collaborate with various theoretical predictions. As shown in Figures 2.7 and

2.11, boron doping generates mainly B-H bonding in the *a*-Si:H matrix observed as a vibrational mode at 2465 cm^{-1}. No higher H substitution on boron, like BH_2 and BH_3 vibrational modes at 2500-2565 cm^{-1},[17] were observed. In addition, no three-centered-two-electron Si-H-B bridge formation was observed at 1850 cm^{-1} in the PECVD *a*-Si:H thin films up to a boron doping ratio of 0.32. Therefore, H-passivation via the B-H pair formation is not the main cause of inefficient boron doping in *a*-Si:H thin film. Previously, the resistivity of *a*-Si:H thin film has shown to reach saturation after a boron doping ratio of 0.13. A further increase in boron dopant concentration does not yield lower resistivity;[4] however MIR-IR spectroscopic analyses show B-H bonding in *a*-Si:H continues to increase up to boron doping ratio of 0.32, Figure 2.7(A) The result suggests that the part of the inactive a boron doping coordination configuration should include B-H bonding. It is proposd that the threefold coordination of B (2,1) (a boron atom with two Si and one H neighbors) contributes to the inactive boron doping in PECVD grown *a*-Si:H thin films based on MIR-IR characterization.

2.8 X-ray Photoelectron Spectroscopy Analyzation on a-Si:H(B) Films

X-ray photoelectron spectroscopy (XPS) was performed on *a*-Si:H(B) samples. Figure 2.12 displays four such spectra. XPS confirmed MIR-IR data in the increase in Si-B peak height that was observed when boron concentration was increased from 0.12 to 0.32 [BCl_3/SiH_4] shown in Figure 2.12.

The inverse relationship between boron concentration and hydrogen dilution is also seen in Raman spectroscopy. Kiran Shrestha shows that there is less mid-range order in *a*-Si:H(B) films with low hydrogen dilution or high boron concentration.[18] When the [SiH_2]/([SiH_2]+[SiH]) peak

height ratio is high in MIR-IR spectra, there is a direct relationship in less organization a-Si:H(B) films.

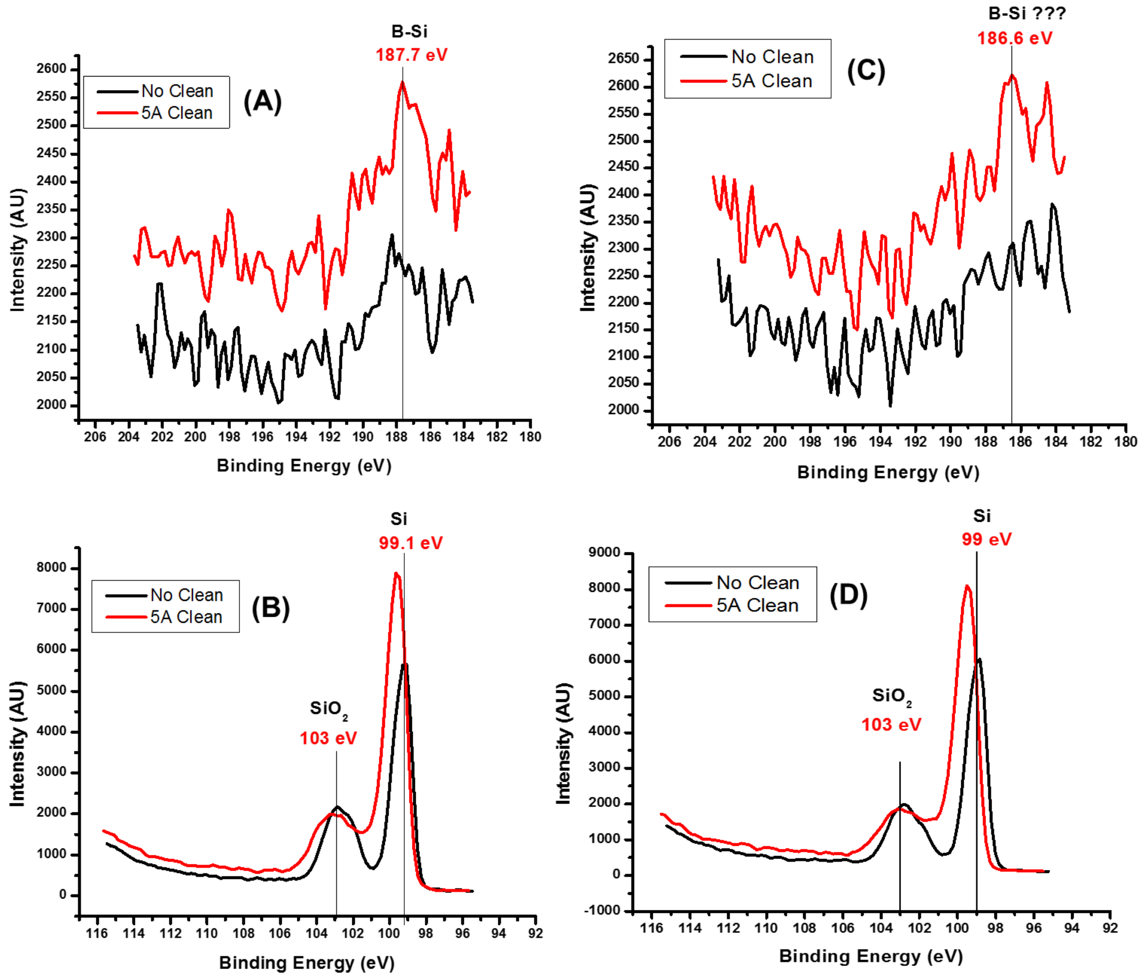

Figure 2.12: (A&B) XPS spectra of an a-Si:H(B) film with 0.32 BCl_3/SiH_4 boron concentration and 60:1 $[H_2]/[SiH_4]$ hydrogen dilution. (C&D) XPS spectra of an a-Si:H(B) film with 0.12 BCl_3/SiH_4 boron concentration and 60:1 $[H_2]/[SiH_4]$ hydrogen dilution.

2.9 Conclusion

MIR-IR characterization of PECVD grown *a*-Si:H thin film shows well-resolved bonding modes of B-H, O-SiHx, SiH_2 and Si-H. An interesting counter-balance relationship between boron-doping and hydrogen-dilution growth parameters was observed. MIR-IR data suggests a competition between boron and silicon to capture hydrogen during the PECVD growth process.

Threefold coordination of B (2,1) (a boron atom with two Silicon atoms and one hydrogen atom neighbors) could contribute to the inactive boron doping in *a*-Si:H thin film. XPS and Raman spectroscopy validated MIR-IR analysis.

2.10 References

1. Street, R. A. Hydrogenated Amorphous Silicon. *Cambridge: Cambridge University Press* **1991**, *1st ed.*

2. Wooten, F.; Winer, K.; Weaire, D. Computer Generation of Structural Models of Amorphous Si and Ge. *Phys. Rev. Lett.* **1985**, *54*, 1392.

3. Syllaios, A. J.; Tyber, G. S.; Taylor, M. F.; Hollingsworth, R. E. - Amorphous silicon thin-films for uncooled infrared microbolometer sensors. *SPIE* **2010**, *7660*, 766012.

4. Ajmera, S. K.; Syllaios, A. J.; Tyber, G. S.; Taylor, M. F.; Hollingsworth, R. E. Amorphous silicon thin-films for uncooled infrared microbolometer sensors. **2010**, *7660*, 766012.

5. Saint John, D. B.; Shin, H. B.; Lee, M. Y.; Ajmera, S. K.; Syllaios, A. J.; Dickey, E. C.; Jackson, T. N.; Podraza, N. J. Influence of Microstructure and Composition on Hydrogenated Silicon Thin Film Properties for Uncooled Microbolometer Applications. *J. Appl. Phys.* **2011**, *110*, 033714.

6. Collins, R. W.; Ferlauto, A. S.; Ferreira, G. M.; Chen, C.; Koh, J.; Koval, R. J.; Lee, Y.; Pearce, J. M.; Wronski, C. R. Evolution of microstructure and phase in amorphous, protocrystalline, and microcrystalline silicon studied by real time spectroscopic ellipsometry. *Solar Energy Mater. Solar Cells* **2003**, *78*, 143-180.

7. Chyan, O.; Wu, J.; Chen, J. Comparative-Studies of Hydrogen Termination on Single-Crystal Silconsurfaces by FT-IR and Contact-Angle Measurements. *Appl. Spec.* **1997**, *51*, 1905.

8. Harrick, N. J. *Internal Reflection Spectroscopy;* John Wiley &Sons: 1967; .

9. Guanghua, C.; Chenzhi, Z.; Fangqing, Z.; Jinlong, C.; Wei, C. ESR and IR Studies on B-Doped Hydrogenated Amorphous Silicon-Nitrogen Film. *phys. stat. sol. (a)* **1986**, *96*, K187-K189.

10. Stutzmann, M. "Data on hydrogen in a-Si:H from diffusion and effusion studies". In *Amorphous Silicon and its Alloys*; Searle, T., Ed.; 1998; Vol. No. 19, pp p. 66.

11. Rimal, S.; Ross, N.; Pillai, K. S.; Singh, K. J.; Chyan, O. Characterization of Post Etch Residues on Patterned Porous Low-k Using Multiple Internal Reflection Infrared Spectroscopy. *ECS* **2011**, *41*, 315-322.

12. Liu, S.; Palsule, C.; Yi, S.; Gangopadhyay, S. Characterization of stain-etch porous silicon. *Phys. Rev. B* **1994**, *49*.

13. Cottrell, T. *The Strengths of Chemical Bonds (Butterworths Scientific Publications);* Academic Press/Butterworths: 1958; Vol. 2nd.

14. Santos, I.; Castrillo, P.; Windl, W.; Drabold, D.; Pelaz, L.; Marqu'es, L. Self-trapping in B-doped Amorphous Si: Interinsic Origin of Low Acceptor Efficiency. *Phys. Rev. B* **2010**, *81*, 033203.

15. Boyce, J.; Ready, S. Nuclear-Magnetic-Double-Resonance Investigation of the Dopant Microstructure in Hydrogenated Amorphous Silicon. *Phys. Rev. B* **1988**, *38*, 11008.

16. Fedders, P. A.; Drabold, D. A. Simulations of boron doping in a-Si:H. *J. Non Cryst. Solids* **1998**, *227–230, Part 1*, 376-379.

17. Socrates, G. *Infrared and Raman Characteristic Group Frequencies;* John Wiley & Sons: USA, 2001; , pp 247-253.

18. Shrestha, K.; Lopes, V. C.; Syllaios, A. J.; Littler, C. L. Raman spectroscopic investigation of boron doped hydrogenated amorphous silicon thin films. *J. Non Cryst. Solids* **2014**, *403*, 80-83.

CHAPTER 3

CHEMICAL BOND CHARACTERIZATION OF BORON DOPED AMORPHOUS SILICON FILMS BY MULTIPLE INTERNAL REFLECTION INFRARED AND RAMAN SPECTROSCOPY AT 275°C AND 365°C SUBSTRATE TEMPERATURE.

3.1 Introduction to Boron Doped Hydrogenated Amorphous Silicon

Thin films of hydrogenated amorphous silicon (*a*-Si:H) exhibit a wide range of structure and properties that enable a broad range of applications and technology base that includes thin film transistors (TFT) for active matrix liquid crystal displays, large area image sensor arrays (e.g. P-I-N photodiode arrays, x-ray imaging arrays), multi-junction solar cells, and micro-electro mechanical systems (MEMS) based sensors, metamaterials, flexible electronics, and microbolometer infrared imaging arrays.[1] Such devices include p-type component layers doped with boron. The doping efficiency of incorporated boron is affected by the details of its bonding configurations to silicon and hydrogen atoms. These films from L-3 were studied using multiple internal refraction infrared (MIR-IR) and Raman spectroscopies in order to analyze for boron incorporation and bonding growth via plasma enhanced chemical deposition (PECVD) at varying substrate temperatures, hydrogen dilution of the silane precursor and dopant to silane ratio.

Boron-doped hydrogenated amorphous silicon (*a*-Si:H(B)) is a material of choice due to its high temperature coefficient of resistance (TCR), relatively high optical absorption coefficient and low cost. Amorphous silicon (*a*-Si) material does not need to be cooled by liquid nitrogen or cooling systems, which makes *a*-Si based microbolometer infrared detector array technology more

portable than MCT detectors.[2] These qualities make *a*-Si an ideal detector material for hand-held and helmet mounted infrared cameras for military and law enforcement personnel.

The ideal structure of amorphous silicon material for hand-held microbolometer detector applications is protocrystalline-Si:H, which has a Si lattice with maximum order but without any formation of microcrystals. To reach the desirable protocrystalline-Si:H microstructure, one must carefully control several factors including hydrogen dilution, substrate temperature, RF power and frequency of PECVD.[3] With 100x increase in MIR-IR detection sensitivity compared to conventional transmission IR, MIR-IR metrology is well suited for the finely-tuned guiding development of amorphous films, shown in Figure 3.1. Growing *a*-Si:H films at a lower 275°C substrate temperature allows for growth on flexible plastic substrates as well as lower production costs. Infrared and Raman analysis has shown that at 275°C substrate temperature, the *a*-Si:H lattice order can be controlled and made as organized as *a*-Si:H films made at 365°C substrate temperature.

Infrared (IR) and Raman spectrometry are used together to receive a more comprehensive understanding of the chemical bonding information of amorphous silicon. The principle of mutual exclusion states that a molecule with a center of symmetry has vibrations that are Raman active and IR inactive and vice-versa. For example, a symmetrical stretch of CO_2 yields no dipole moment and therefore IR inactive; however, there is a change in polarizability and therefore it is Raman active. The asymmetrical stretch of CO_2 yields a dipole moment and is IR active but is not Raman active.[4]

Raman spectroscopy has been implemented for the study of short range order (SRO) and mid-range order (MRO) of *a*-Si.[5-7] In these literatures, by the method of Raman scattering spectroscopy, it is indicated for *a*-Si that this method is the direct and indirect probe of bond angle

disorder and its variation in the disorder state of tetrahedral group IV like silicon. Reduction in intensity ratio (I_{TA}/I_{TO}) is the indication of reduction in bond bending with respect to the stretching vibrations, which is an indication of improvement of MRO. The line width and peak position of transverse optical (TO) mode are associated with the force constant of the stretching vibrations and the bond angle deviation in the tetrahedral neighboring atoms of silicon, so the TO mode is the probe of SRO. Narrow TO line width is the indication of improvement of SRO, and shift of central wavenumber (ω_{TO}) towards the higher frequency is related to the decrease in the average bond length.[8]

Recently, J. He et al. indicated that changes in the gas temperature (T_g) can modify the surface network, hydrogen bonding modes, the density of the film, and improve in SRO and which the optoelectronic properties of *a*-Si:H thin films.[9] This literature also showed with the IR transmittance spectra using wagging mode at 630cm^{-1} that the T_g has a very little effect on total hydrogen content incorporated into the film, whereas using the stretching modes of Si-H (~2000cm^{-1}) and Si-H_2 (~ 2080cm^{-1}), decreases the microstructure factor and increases T_g.[9]

3.2 Experiment

Samples of *a*-Si:H thin films were grown on silicon substrate in a PECVD system using capacitively coupled 13.56 MHz plasmas with the substrate on the ground electrode. Source gases for p-type *a*-Si:H growth were silane (SiH_4) and hydrogen in argon, and boron trichloride (BCl_3). The flow rate ratio of boron to silane (defined as “r” = [BCl_3]/[SiH_4]) and hydrogen dilution to silane ratio (“R_H”=[H_2]/[SiH_4]),were varied to produce films with differing hydrogen and boron concentrations. The samples reported here were grown at R_H values ranging from 4 to 100 and

with “r” values of 0.12 and 0.32. MIR-IR was used to characterize the chemical bonding structure differences due to variation of H dilution and B doping during temperature change in PECVD deposition. MIR-IR utilizes the silicon wafer itself as an IR waveguide for attenuated total reflection (ATR) to achieve sub monolayer detection sensitivity. Favorable difference in refractive indices of the Si wafer and its air interface enables multiple total internal reflections (ca. 80 reflections from a 60 mm Si ATR crystal), which greatly enhances IR measuring sensitivity. The *a*-Si:H (ca. 50 nm) coated silicon wafers were fabricated into an ATR optical element (60 x 10 x 0.7 mm, 45° bevel angle) by mechanical polishing.[10] For Si<100> background ATR coupons, standard cleaning (SC1) solution was used to remove any organic contamination from the surface followed by etching in 0.5% HF solution. IR spectra were recorded on a Nicolet IS 50 FTIR spectrometer under constantly purged dry air (CO_2 < 1 ppm). Both transmission (TIR) and MIR-IR spectra were collected at 2 cm^{-1} resolution and are the average of 100 individual spectra. The detection limit of MIR-IR is ca. 0.2 miliabsorbance (mabs) unit with an error margin of < 3%. A thermo electron almega XR Raman spectrometer with a 532 nm laser as an excitation source and a 2.5 micron spot size was used to obtain room temperature Raman spectra. The thickness of the films investigated ranged from approximately 100 nm to 300 nm for Raman measurements and 50 nm to 100 nm for MIR-IR measurements.

The infrared absorption spectra (MIR-IR and TIR) of an 100 nm thick *a*-Si:H(B) thin film sample grown at 275°C over Si<100> are shown in Figure 3.1. MIR-IR demonstrates over a hundred fold increase in detection sensitivity compared with conventional TIR. The multiple sampling enabled by more than 80 total internal reflections greatly enhances the measuring sensitivity of MIR-IR technique.[10] Previously, MIR-IR monitored hydrogen passivation on Si<100> surface with sub-monolayer measuring sensitivity.[11] The MIR-IR spectrum, Figure 3.1,

reveals well-resolved IR absorption peaks associated with Si-H (1989 cm^{-1}) and B-H (2465 cm^{-1}) bonding modes originated from *a*-Si:H thin film.[12] The aforementioned 100x increase in resolution with MIR-IR brings improved quantification measurements. These improvements include displaying peaks in IR spectra that were previously unseen and showing changes in chemical bonding structure with minute changes in developmental variables which in the past could not be detected. For *a*-Si:H films the developmental variables studied are: hydrogen dilution, boron concentration, substrate temperature, ect.

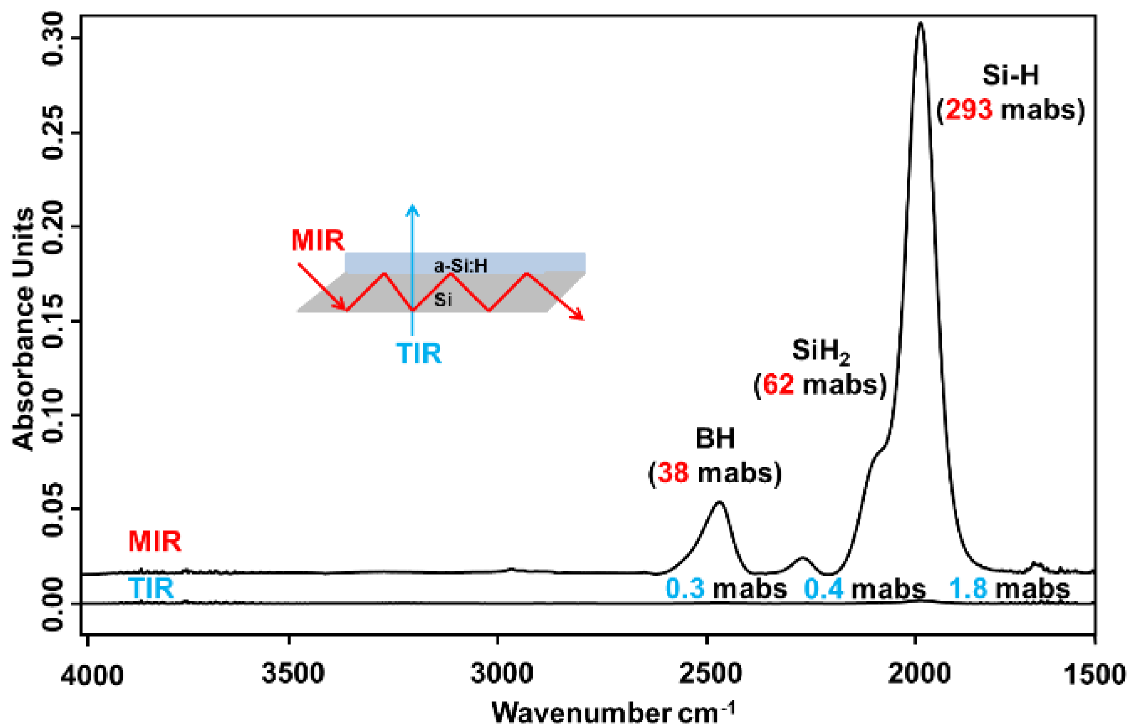

Figure 3.1: 1000 angstrom thick *a*-Si:H(B) layer on top of silicon substrate. Two infrared spectra using two different techniques (MIR and TIR) on the same sample. Peak height is in micro-absorbance units (mabs).

3.3 Organization Ratio of *a*-Si:H(B) Films

The target is to achieve protocrystalline-Si:H film with the majority of the atoms in the silicon lattice in the Si_3-<u>Si</u>-H configuration. This allows for the most organized silicon lattice while

still being a non-crystalline structure. This trend is shown in Figure 3.2.[3] Figure 3.3 displays that when silicon atoms from in a Si_2-Si-H_2 configuration the film becomes more disorganized (more amorphous). If there are too many silicon atoms with a Si_4-Si configuration, then the film becomes microcrystalline.[13] One of the figures of merit by industry is the $[SiH_2]_n/([SiH]+[SiH_2]_n)$ ratio. The higher the $[SiH_2]_n/([SiH]+[SiH_2]_n)$ ratio the more disorganized the film.

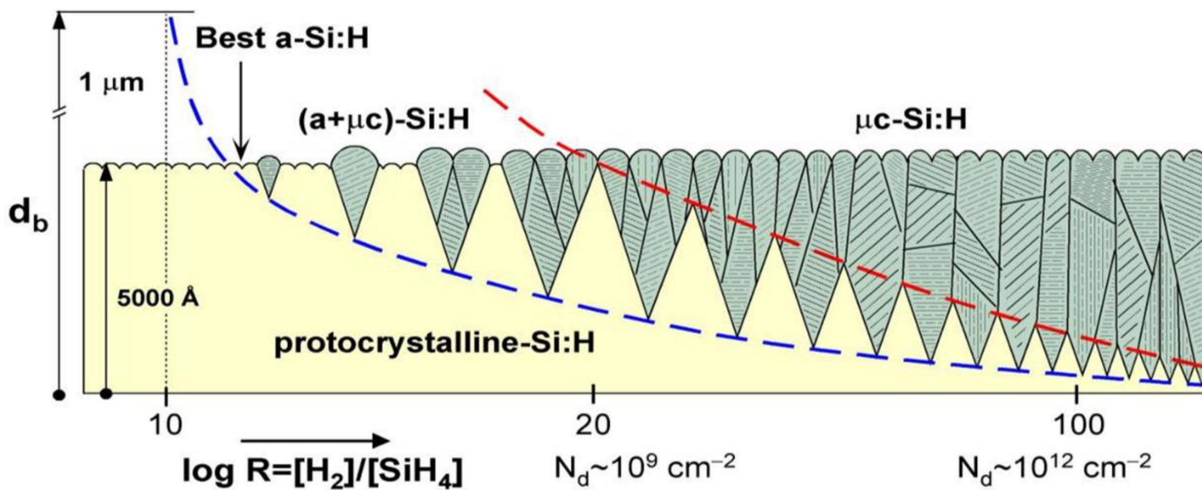

Figure 3.2: Amorphous, micro-crystalline and crystalline silicon in terms of film thickness and hydrogen dilution $[H_2]/[SiH_4]$.[3]

Past research focused on the effect of hydrogen dilution (R_H) and boron concentration (r) by MIR-IR study. The conclusion was that there is an inverse relationship between hydrogen dilution (R_H) and boron concentration (r). An increase in hydrogen dilution would create a decrease in the $[SiH_2]_n/([SiH]+[SiH_2]_n)$ ratio, while an increase boron concentration had the opposite effect.[11]

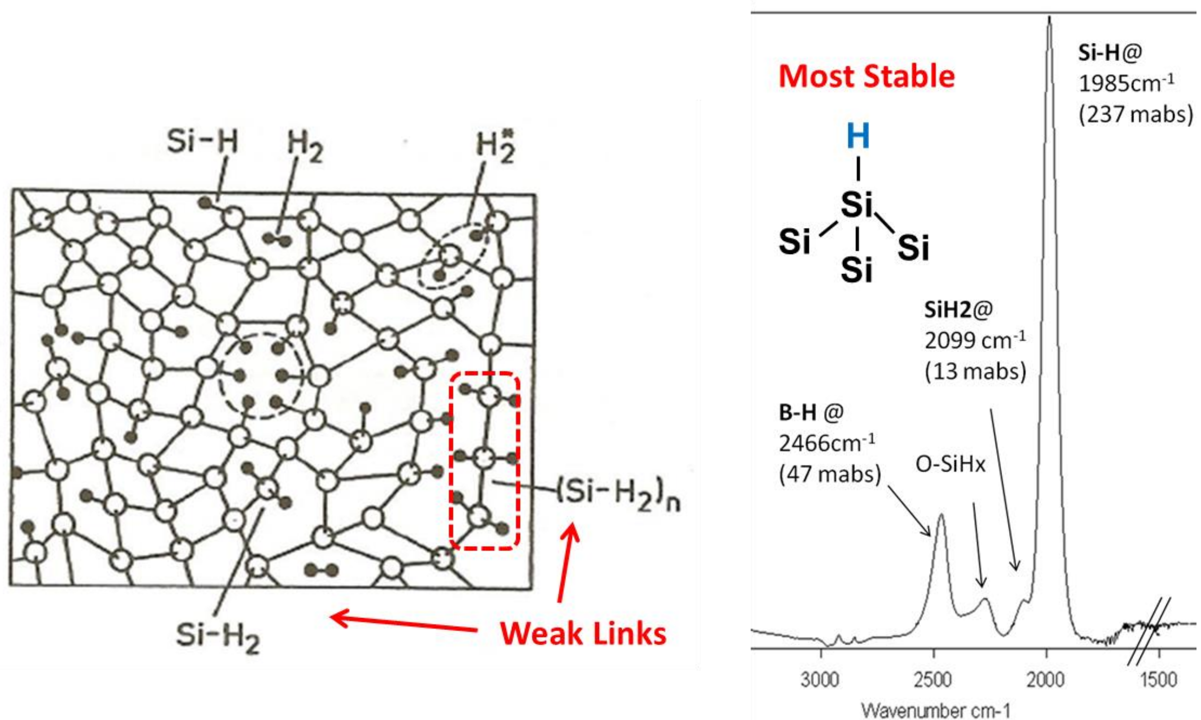

Figure 3.3: Hydrogenated amorphous silicon structure example with the main chemical bonds with an example MIR-IR spectra for reference.[13]

3.4 Boron Concentration Effect on Resistance on *a*-Si:H(B) Films

Research since the Ross, N. et al. 2012 paper has been focused on the effects of substrate temperature and low boron doping efficiency in *a*-Si:H films.[14] According to Ajmera, S. K 2010 after 1.9 sccm $[BCl_3]/[SiH_4]$ = r any increase in boron concentration will not decrease the resistivity.[14] Figure 3.4(A) shows that on r above 0.19 $[BCl_3/ SiH_4]$ yielded no change in resistivity. MIR-IR results show that there is an increase in B-H bonds within the film above r = 0.19 $[BCl_3/ SiH_4]$. Therefore, the boron is attached to the *a*-Si:H film in a non-active doping mode, Figure 3.4(B).[15,16] Chemical bonds labeled below the spectra are possible configurations of boron in an *a*-Si:H(B) matrix but were not seen in MIR-IR analysis. Non-observed chemical bonding locations are displayed by thick red lines on MIR-IR spectrum and chemical bonds labled above spectra are

chemical bonds that are visable in MIR-IR analysis, Figure 3.4(B). There are no peaks located at 2550cm^{-1}, 1900cm^{-1}, and 1850cm^{-1}, thus there are no observed BH_2, B-H-B, or Si-H-B bonds respectfully. The bonds detected by MIR-IR at 2466cm^{-1}, 2100cm^{-1} and 1900cm^{-1} are B-H, *a*-Si-H_2 and *a*-Si-H respectfully. This chemical bonding information is how assignment of the chemical configurations to the "observed" and "not observed" sections in Figure 3.4(B) where made. It has been previously shown that increasing boron concentration decreases organization in *a*-Si:H(B) matrix.[11] Thus, for the purpose of *a*-Si:H(B) films made for microbolometer, it is not adviseable to dope above r = 0.19 [BCl_3/ SiH_4].

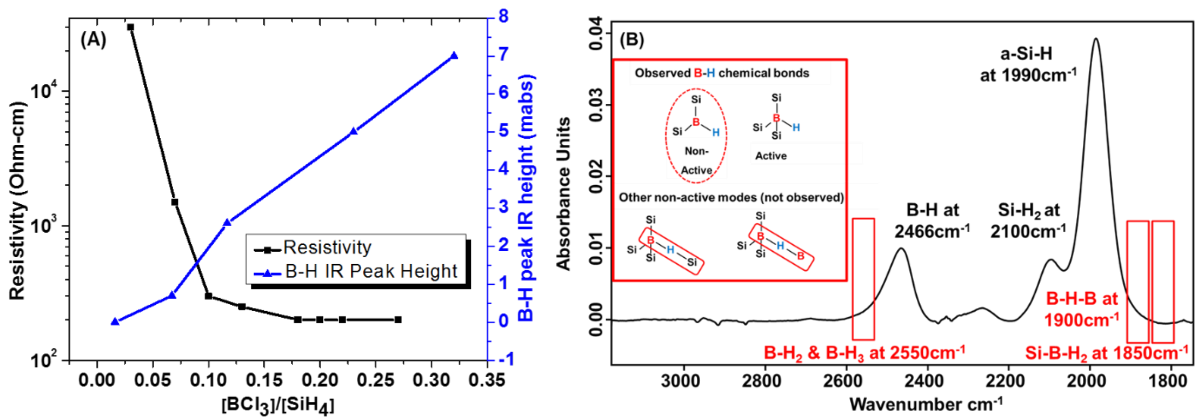

Figure 3.4: (A) resistivity vs boron concentration (r) = [BCl_3/ SiH_4]. (B) Active and non-active boron doping configurations with a MIR-IR spectrum of an *a*-Si:H(B) sample.

3.5 Substrate Temperature Effect on Organization of *a*-Si:H(B) Films by MIR-IR Analysis

The effects of lowering substrate temperature from 365°C to 275°C via PECVD on *a*-Si:H thin film were studied by MIR-IR. MIR-IR spectra of *a*-Si:H(B) film at 365°C and 275°C substrate temperature is displayed in Figure 3.5. The sample set with 275°C substrate temperature has an *a*-Si:H(B) film layer that is twice as thick (100nm) than the sample set grown at 365°C substrate (50nm). To correct for film thickness, the spectrum intensity for 275°C substrate temperature is

reduced by one half for better comparison in Figure 3.5. Both spectra have the same boron concentration and hydrogen dilution. At 275^oC substrate temperature, hydrogen stays within the material at a higher percentage than that of the 365^oC substrate temperatures. This is due to less hydrogen boil off. This explains the almost double in peak height for B-H and Si-H bonds. The 7x increase in peak height for the peak corresponding to SiH_2 bond is an indicator that the *a*-Si:H(B) film has become more disorganized. In Figure 3.5, the $[SiH_2]_n/([SiH]+[SiH_2]_n)$ ratio for 365^oC and 275^oC are 0.2 and 0.45 respectfully. This increase in $[SiH_2]_n/([SiH]+[SiH_2]_n)$ ratio by a factor of 2.25 indicates that lowering the substrate temperature during the PECVD process decreases the organization of the *a*-Si lattice significantly.

The O-H bonds in Figure 3.5-3.7 are due to isolated Si-OH and Si-(OH)x bonds located at 3620cm^{-1} and 3400cm^{-1} respectfully.[17] Most likely, silanol and O-H developed in the *a*-Si:H(B) films due to residual moister and oxygen in the PECVD chamber. The O-H peak height in Figure 3.5-3.7 for *a*-Si:H(B) films becomes no longer detectable when the hydrogen dilution is increased or substrate temperature is increased. This decrease in O-H with increase in hydrogen dilution is due to less voids being created within the amorphous film.[1] It has been shown that with an increase in ratio of hydrogen dilution to silane, the effect is a more organized amorphous film.[11] The 365^oC substrate sample set does not have an observable O-H peak for the same reason, due to increased organization compared to the 275^oC sample set. It has been previously shown that with an increase of hydrogen dilution there are more Si-H bonds and a reduction in SiH_2, thus less voids within the film to allow oxygen to be trapped within the film. To fix the $Si\text{-}(OH)_x$ issue in *a*-Si:H films, one can increase hydrogen dilution to out gas the oxygen or raise the temperature to “bake” the chamber to remove moisture and oxygen. For example, the O-H peak height in Figure 3.5-3.7 for

a-Si:H(B) films becomes no longer detectable when the R_H is increased or substrate temperature is increased.

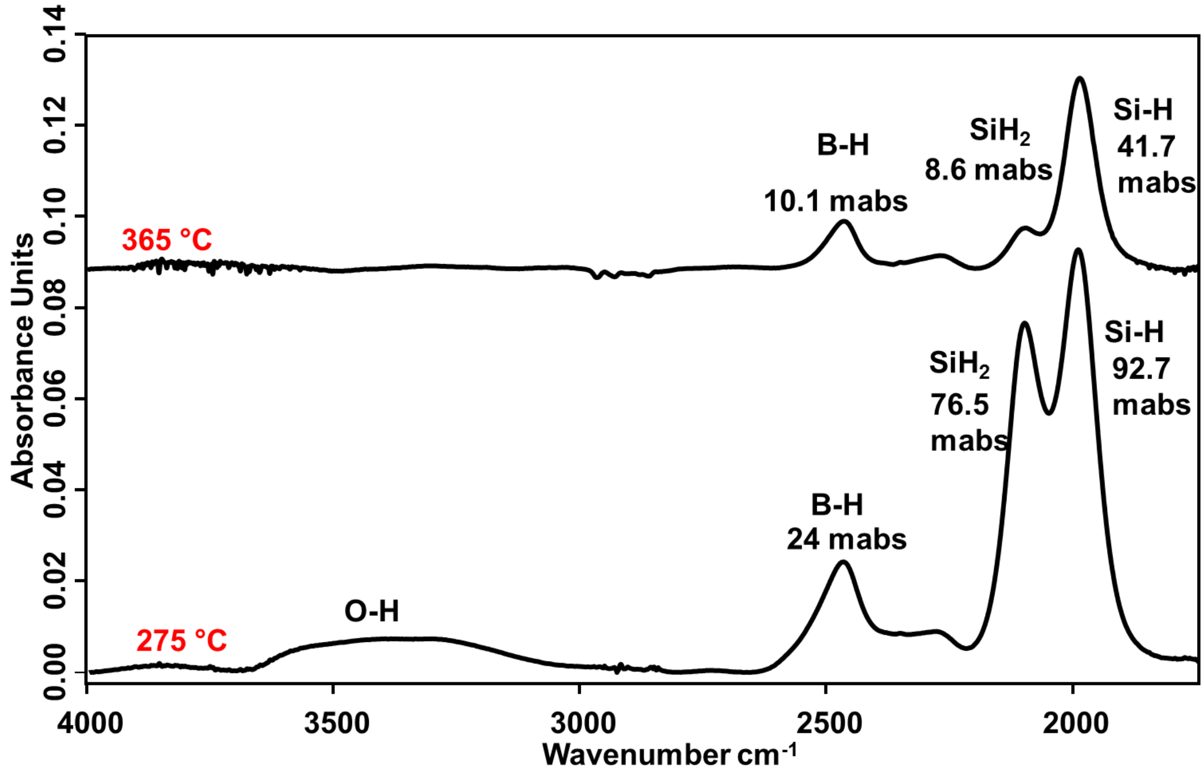

Figure 3.5: MIR-IR spectra of two *a*-Si:H(B) films grown at 365°C and 275°C substrate temperature. Intensity is reduced by a factor of 2 for the MIR-IR spectrum of the 275°C sample due the film having a film thickness double than the 365°C sample.

Ten MIR-IR spectra of *a*-Si:H(B) films grown at 275°C substrate temperature are shown in Figure 3.6. Hydrogen dilution values of 4/1, 10/1, 16/1 and 40/1 [H_2]/[SiH_4] were observed with boron concentration values of 0.12, 0.27 and 0.32 [BCl_3/ SiH_4]. The Ross, N. et al. 2012 paper shows a similar trend in hydrogen dilution and boron concentration with films in terms of organization. These trends and comparisons are better shown in Figure 3.7, 3.8 and 3.11.

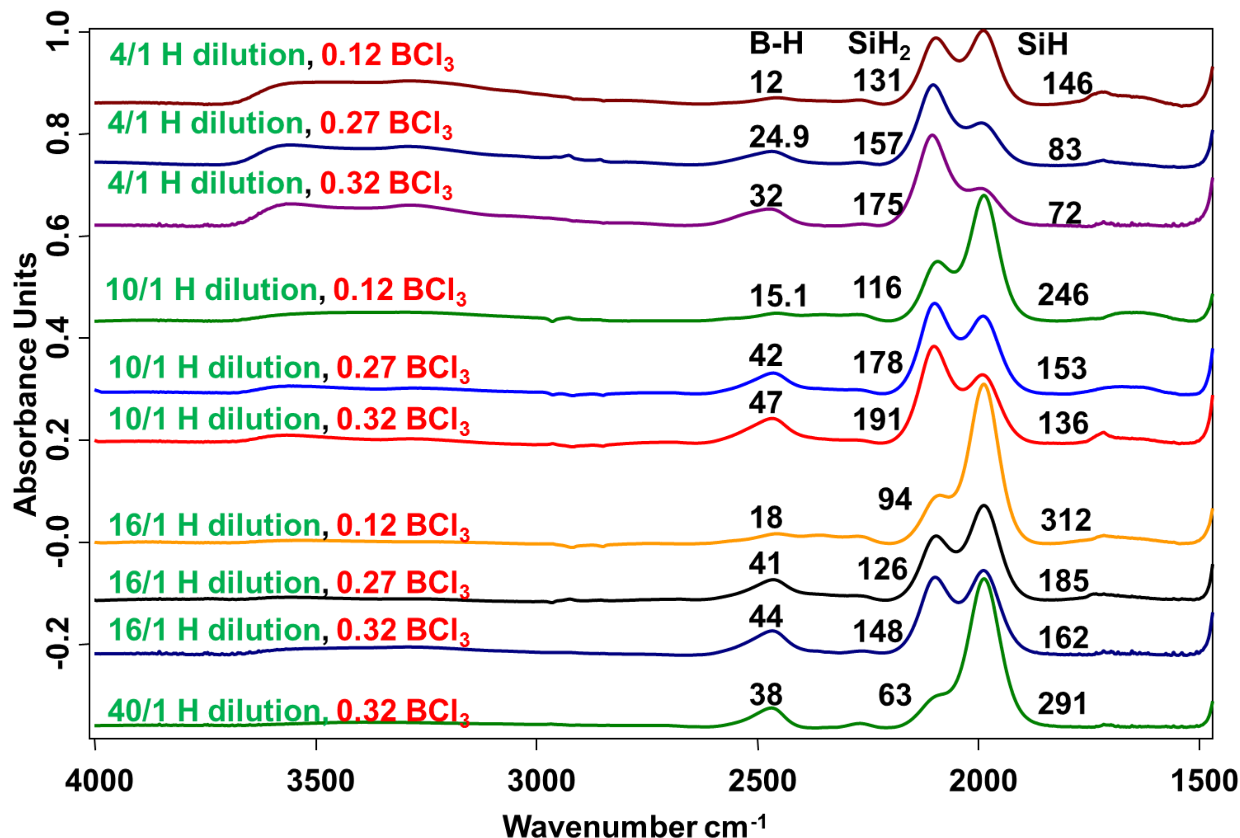

Figure 3.6: Ten MIR-IR spectra of *a*-Si:H(B) films grown at 275°C substrate temperature. Hydrogen dilution values of 4/1, 10/1, 16/1 and 40/1 [H_2/SiH_4] and with boron concentration values of 0.12, 0.27 and 0.32 [BCl_3/SiH_4].

Figure 3.7 (A, B) shows MIR-IR spectra of *a*-Si:H(B) films varying by hydrogen dilution and all samples have the same boron concentration. Figure 3.7(A, B) shows that an increase in hydrogen dilution has an increased effect at 275°C versus 365°C. For example, the bottom two spectra in Figure 3.7(A) differ from 16/1 to 40/1 hydrogen dilution and the $[SiH_2]_n/([SiH]+[SiH_2]_n)$ ratio goes from 0.45 to 0.19 respectfully. In comparison at 365°C substrate temperature when the hydrogen dilution increases by 29 (16 to 45 R_H) there is an increase in $[SiH_2]_n/([SiH]+[SiH_2]_n)$ ratio by 0.11. The $[SiH_2]_n/([SiH]+[SiH_2]_n)$ is increased significantly more at 275°C versus 365°C substrate temperature. This is due to hydrogen gas not being boiled out of the material as quickly at lower substrate temperatures, thus increasing the chance for Si-H bonds to form.[18]

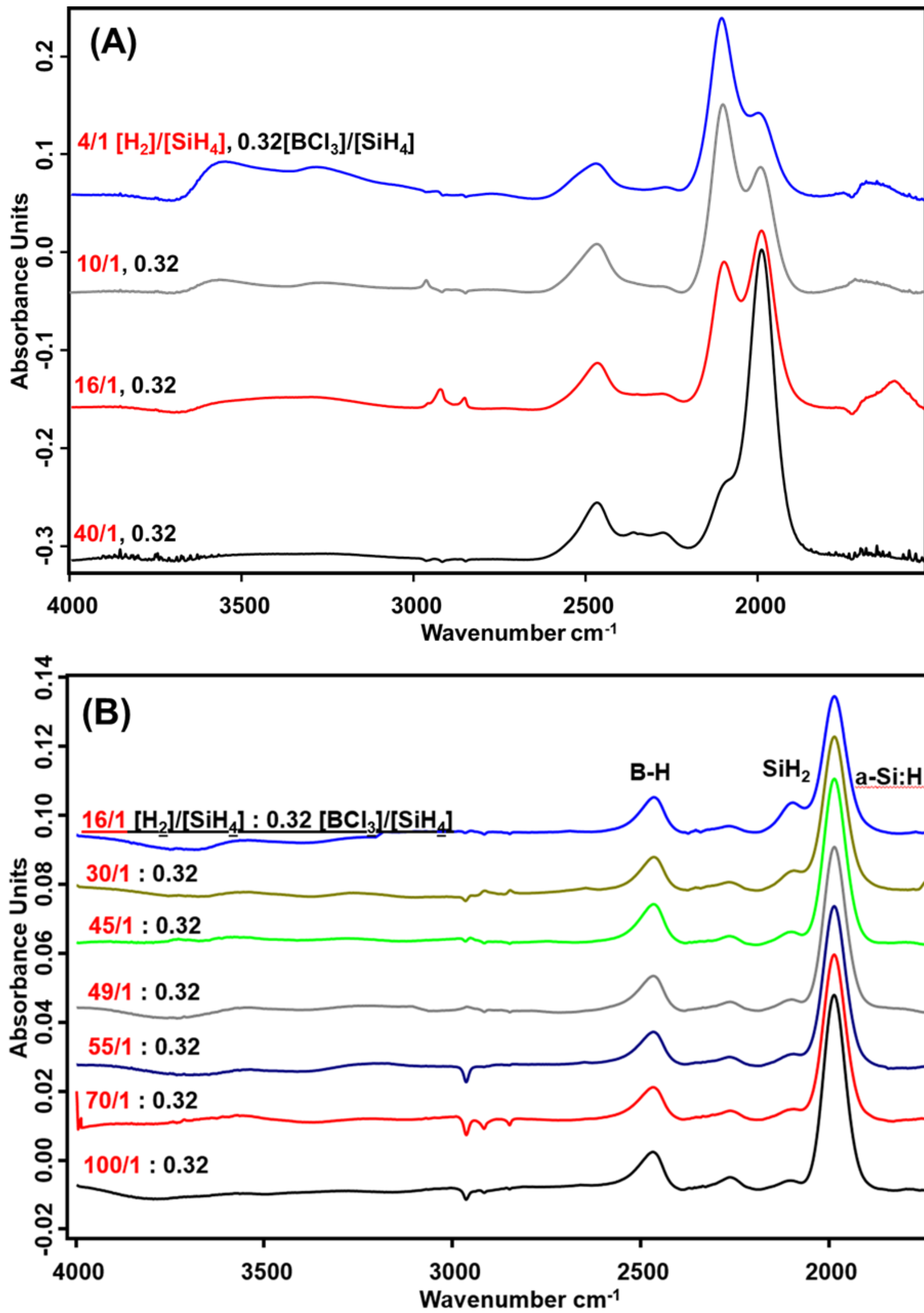

Figure 3.7: (A) Four *a*-Si:H(B) samples grown at substrate temperature 275°C and analyzed by MIR-IR spectroscopy. These samples have a boron concentration value of 0.32 [BCl_3/SiH_4] and hydrogen dilution values of 4/1, 10/1, 16/1, and 40/1 [H_2/SiH_4]. (B) Seven *a*-Si:H(B) samples were grown at substrate temperature 365°C and analyzed by MIR-IR spectroscopy. These samples have a boron concentration value of 0.32 [BCl_3/SiH_4] and hydrogen dilution values of 16/1, 30/1, 45/1, 49/1, 55/1, 70/1, and 100/1 [H_2/SiH_4].

In Figure 3.8(A-C), there are MIR-IR spectra with varying hydrogen dilution at 4/1, 10/1 and 16/1 [H_2/SiH_4] with boron concentration values of 0.12, 0.27, or 0.32 [BCl_3/ SiH_4]. As the boron concentration increases, the *a*-Si:H(B) film becomes more disorganized. In Figure 3.8(A) there is an increase in Si:H_2 peak height and a decrease in Si:H peak height when boron concentration is increased, thus increasing the $[SiH_2]_n/([SiH]+[SiH_2]_n)$ ratio which is a sign of a decrease in organization. When the hydrogen dilution is increased, the opposite trend occurs and the organization is increased. [11]

There is an increase in boron concentration by 0.05 [BCl_3/ SiH_4] from first (R_H = 4 [H_2/SiH_4], r = 0.12 [BCl_3/ SiH_4]) and second (R_H = 4 [H_2/SiH_4], r = 0.27 [BCl_3/ SiH_4]) spectrum in Figure 3.8(A). The increase in boron concentration by 0.05 [BCl_3/ SiH_4] increases the B-H peak height from 12 to 24.9 mabs, *a*-SiH_2 peak height from 131 to 157, and *a*-Si:H from 146 to 83 mabs. This increases the $[SiH_2]_n/([SiH]+[SiH_2]_n)$ ratio from 0.469 to 0.654 from first and second spectrum respectfully. As the boron concentration increases the material becomes more disorganized. At a higher boron concentration there is more boron in the material to bond with the *a*-Si matrix, thus decreasing the amount of Si_4-<u>Si</u> and Si_3-<u>Si</u>-H bonds and increasing the amount of Si_2-<u>B</u>-H bonds which decreases organization by creating wider short range angles.[1] Thus an increase in *a*-SiH_2 peak height in MIR spectra, is a decrease in organization by having Si_2-<u>Si</u>-H_2 bonds and less Si_3-<u>Si</u>-H bonds in the *a*-Si:H matrix.

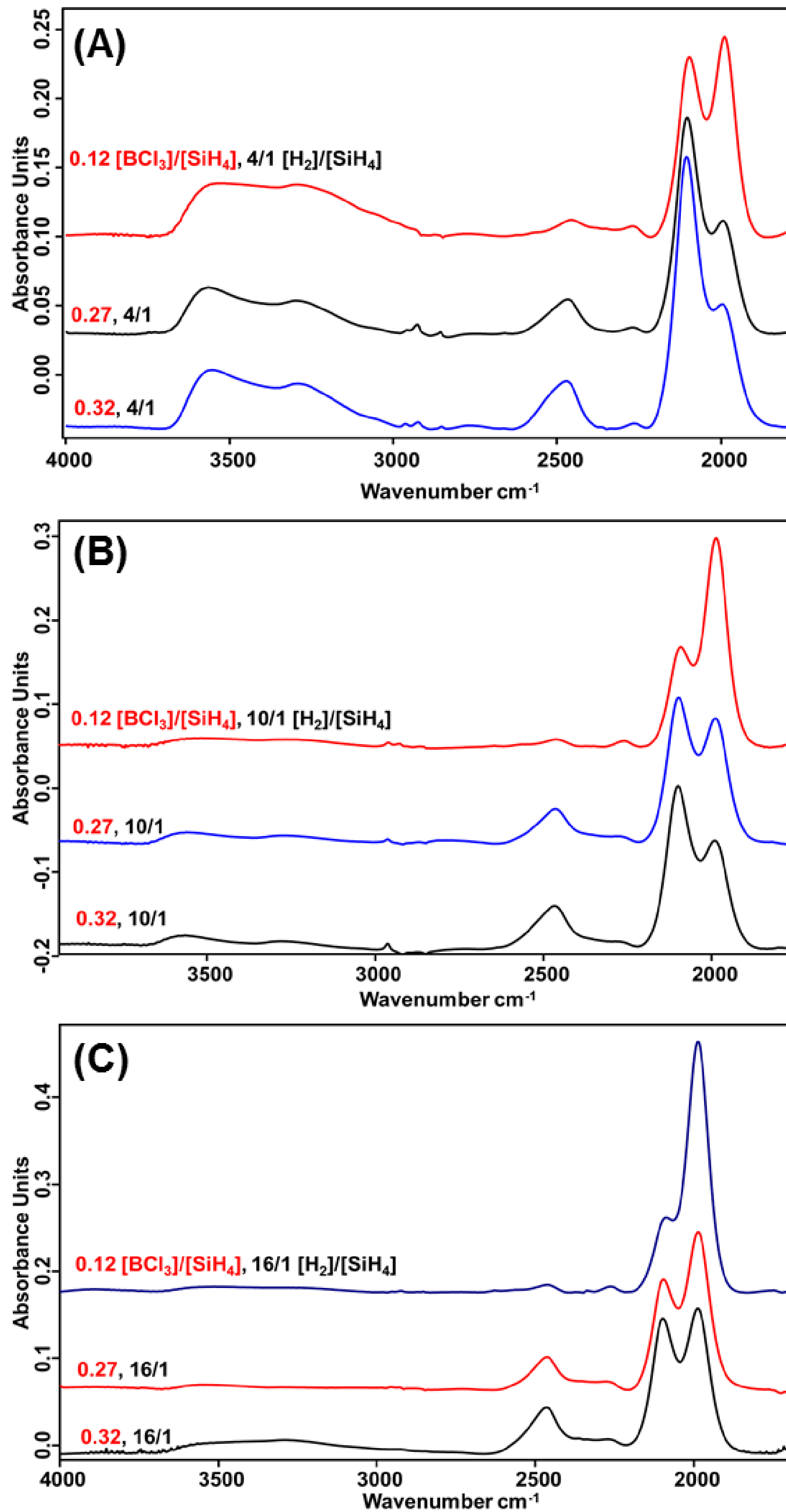

Figure 3.8: (A-C) Three *a*-Si:H(B) samples grown at substrate temperature 275ºC and analyzed by MIR-IR spectroscopy. These films have boron concentration values of 0.12, 0.27, and 0.32 [BCl_3/SiH_4] and hydrogen dilution value of (A) 4/1, (B) 10/1, and (C) 16/1 [H_2/SiH_4].

Figure 3.9(A, B) shows the normalized peak height values from MIR-IR analysis of B-H, *a*-SiH_2, and *a*-SiH bonds on *a*-Si:H(B) films with varying hydrogen dilution values and with a boron concentration of 0.32 [BCl_3/ SiH_4] at (A) 275ºC (B) 365ºC substrate temperature. Normalizing the data and putting the peak height in linegraph form makes the trend easier to display. Increasing the hydrogen dilution at 275ºC versus 365ºC is due to less hydrogen boil off at a lower substrate temperature. This allows more Si_4-Si bonds to break to become Si_2-Si-H_2 and Si_3-Si-H bonds.

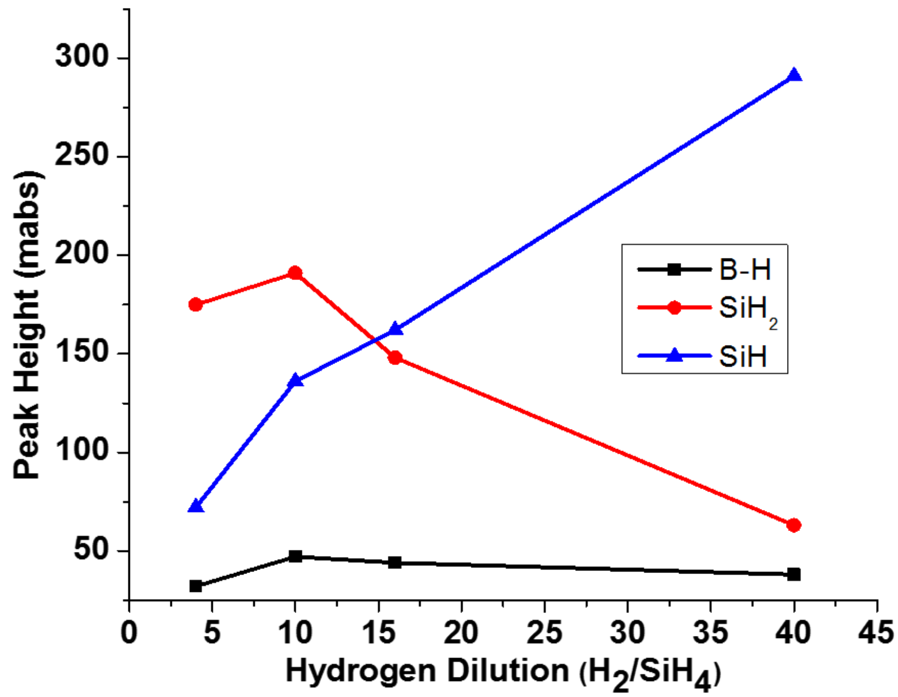

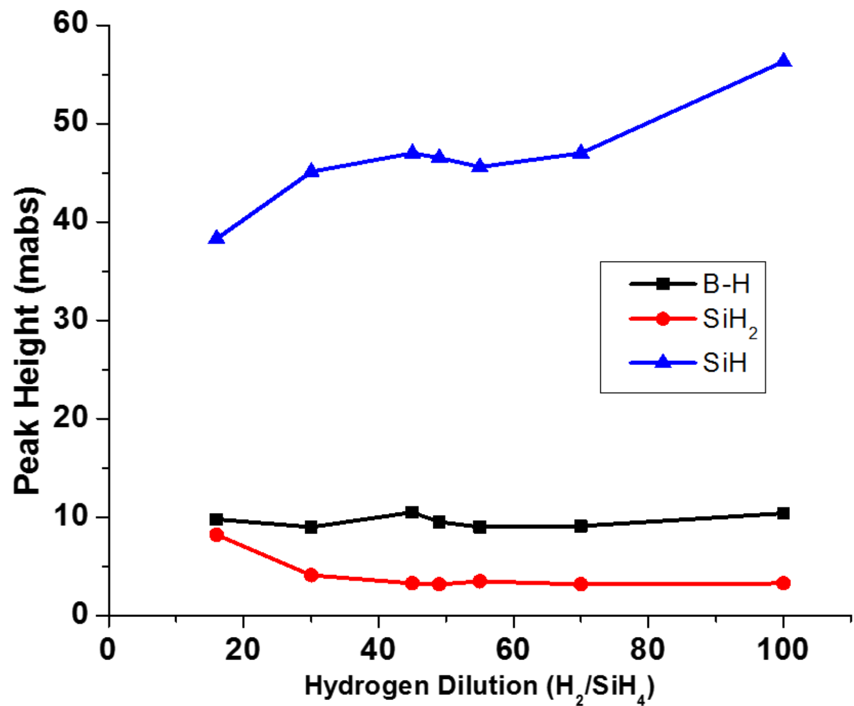

Figure 3.9: MIR-IR analysis of hydrogen dilution dependent line graph showing normalized peak height of B-H, SiH_2, and SiH bonds on *a*-Si:H(B) films with varying hydrogen dilution values and boron concentration 0.32 [BCl_3/ SiH_4] at (A) 275ºC (B) 365ºC substrate temperature.

3.6 Raman Analysis on *a*-Si:H(B) Films

Raman analysis was done by Kiran et al. in collaboration with the same sample sets analyzed by MIR-IR.[18] Raman analysis displays similar results to MIR-IR analysis displayed in Figure 3.10 and 3.11. For example, *a*-Si:H(B) films grown at 16/1 hydrogen dilution and 275°C substrate temperature are more disorganized than films grown at 16/1 hydrogen dilution at 365°C substrate temperature. This trend is displayed in Figure 3.10 with a larger and broader full width at half maximum (FWHM) for line width of transverse optical (TO) at 475cm^{-1} and transverse acoustic (TA) at 154cm^{-1} for samples grown with 16/1 hydrogen dilution at substrate temperature at 275°C versus 365°C. This translates in an increase in bond angle and bond length, leading to a degradation of the short range order (SRO) which shows a more disorganized amorphous state at substrate temperature 275°C versus 365°C.[6] Also at 275°C substrate temperature the line width of TO and the intensity of TA is larger than films grown at 16/1 hydrogen dilution and 365°C substrate temperature which point to a more amorphous state of the film.[18]

Raman analysis agrees with MIR-IR analysis that the 275°C substrate temperature samples are more effected by hydrogen dilution than 365°C substrate temperature samples. Also it is shown that 275°C substrate temperature samples can be made as organized as 365°C substrate temperature samples with high hydrogen dilution as shown by Figure 3.10 and 3.11. There is not much change in terms of organization for 365°C substrate temperature sample set with the increase in hydrogen dilution displayed in Figure 3.10(B). Hydrogen dilution has an increased factor at 275°C substrate temperature in terms of increasing the organization of the *a*-Si:H(B) films. As observed by R. W. Collin et al.[3] with the increase of hydrogen dilution, the thin film becomes a more organized amorphous structure as evidence of the decrease of the line width of TO and decrease in TA intensity as shown in Figure 3.10(A). Figure 3.10(B) shows that the line width of 365°C substrate

temperature does not change as much as that of the 275°C substrate temperature, indicating that the hydrogen dilution has minimal effect on higher substrate temperatures. This trend is due to the fact that at 365°C substrate temperature, hydrogen is more likely to dissociate from the material.[18] Thus at 275°C substrate temperature, hydrogen dilution can be more effectively used to guide the *a*-Si:H(B) matrix to the desired amount of organization. MIR-IR analysis shows that at 365°C substrate temperature and 100/1 hydrogen dilution, there is lower $[SiH_2]_n/([SiH]+[SiH_2]_n)$ ratio. Raman shows more ordered SRO and mid ranged order (MRO) in the *a*-Si:H(B) material at higher substrate temperature and higher hydrogen dilution. Raman studies confirm the MIR-IR analysis in Figures 3.5 and 3.7. In short, MIR-IR and Raman studies both show that by increasing either hydrogen dilution or substrate temperature during PECVD, increases the organization of the silicon lattice in the amorphous films.

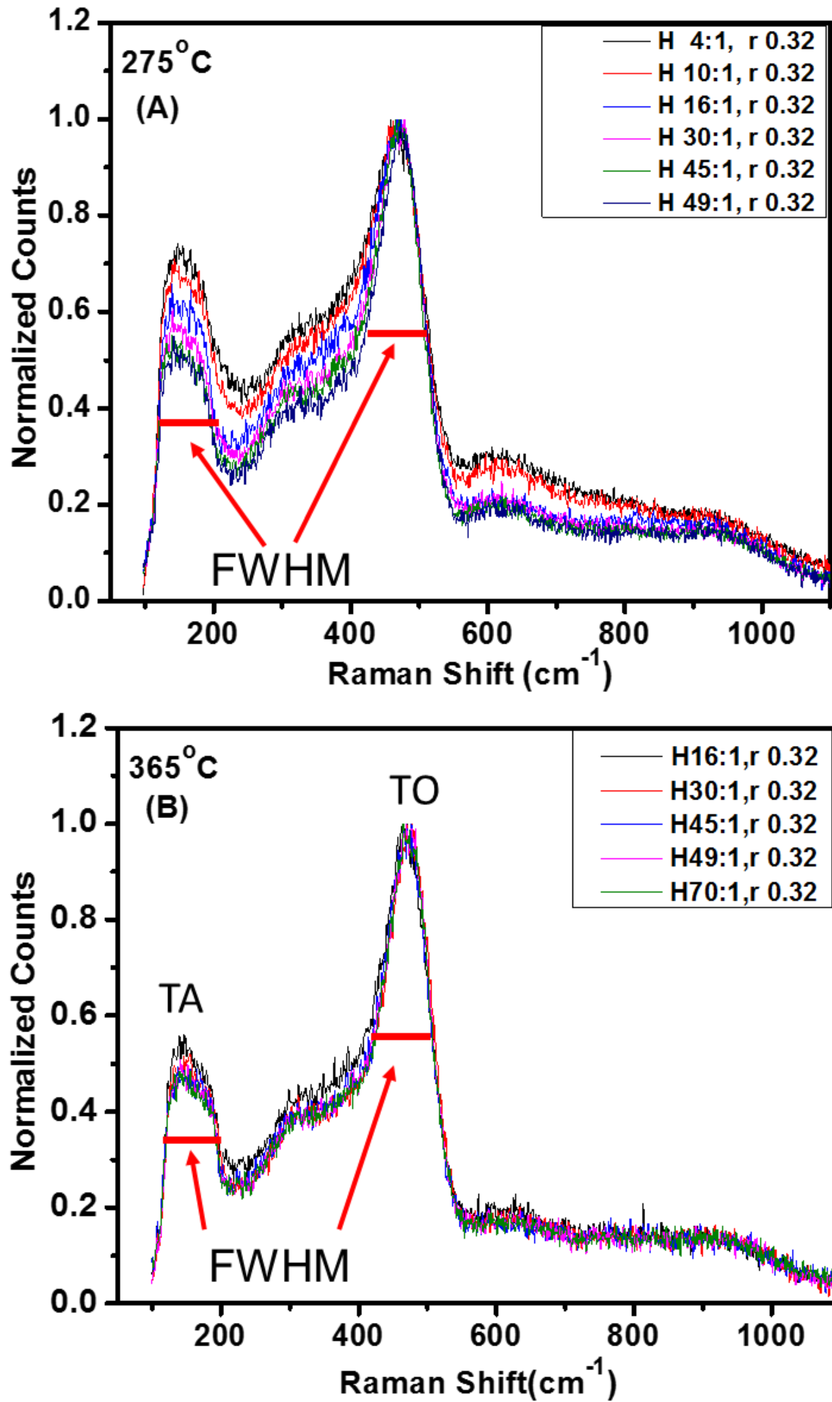

Figure 3.10: Raman analysis showing normalized peak height of Transvers acoustic (TA) at 154cm^{-1}, Longitudinal acoustic (LA) at 310cm^{-1}, Longitudinal optical (LO) at 405cm^{-1}, and Transverse optical (TO) at 475cm^{-1} on *a*-Si:H(B) films at (A) 275°C (B) 365°C substrate temperature.[18]

Figure 3.12 displays values of $[SiH_2]_n/([SiH]+[SiH_2]_n)$ ratio and I_{TA}/I_{TO} ratio from MIR-IR and Raman analysis respectfully. Mid-range order (MRO) is defined by the intensity of TO divided by intensity of TA (I_{TO}/I_{TA}). Having a lower I_{TO}/I_{TA} ratio indicates a more organized lattice than having a high I_{TO}/I_{TA} value.[7] R_H values of 4/1 to 45/1 for Raman and R_H values of 4/1 to 40/1 for MIR-IR are more disorganized for the *a*-Si:H(B) films grown at substrate temperature 275°C substrate temperature versus 375°C substrate temperature. In Raman analysis, 49/1 R_H is the hydrogen dilution that shows the *a*-Si:H(B) more organized at 275°C substrate temperature versus 375°C substrate temperature. Since Raman analysis is showing similar results to MIR-IR then samples with a high $[SiH_2]_n/([SiH]+[SiH_2]_n)$ ratio in MIR-IR analysis will have less SRO and MRO. MIR-IR analysis shows a steeper slope for 275°C substrate temperature versus 375°C substrate temperature, however future work with *a*-Si:H(B) with higher hydrogen dilution will be needed to confirm the theory.

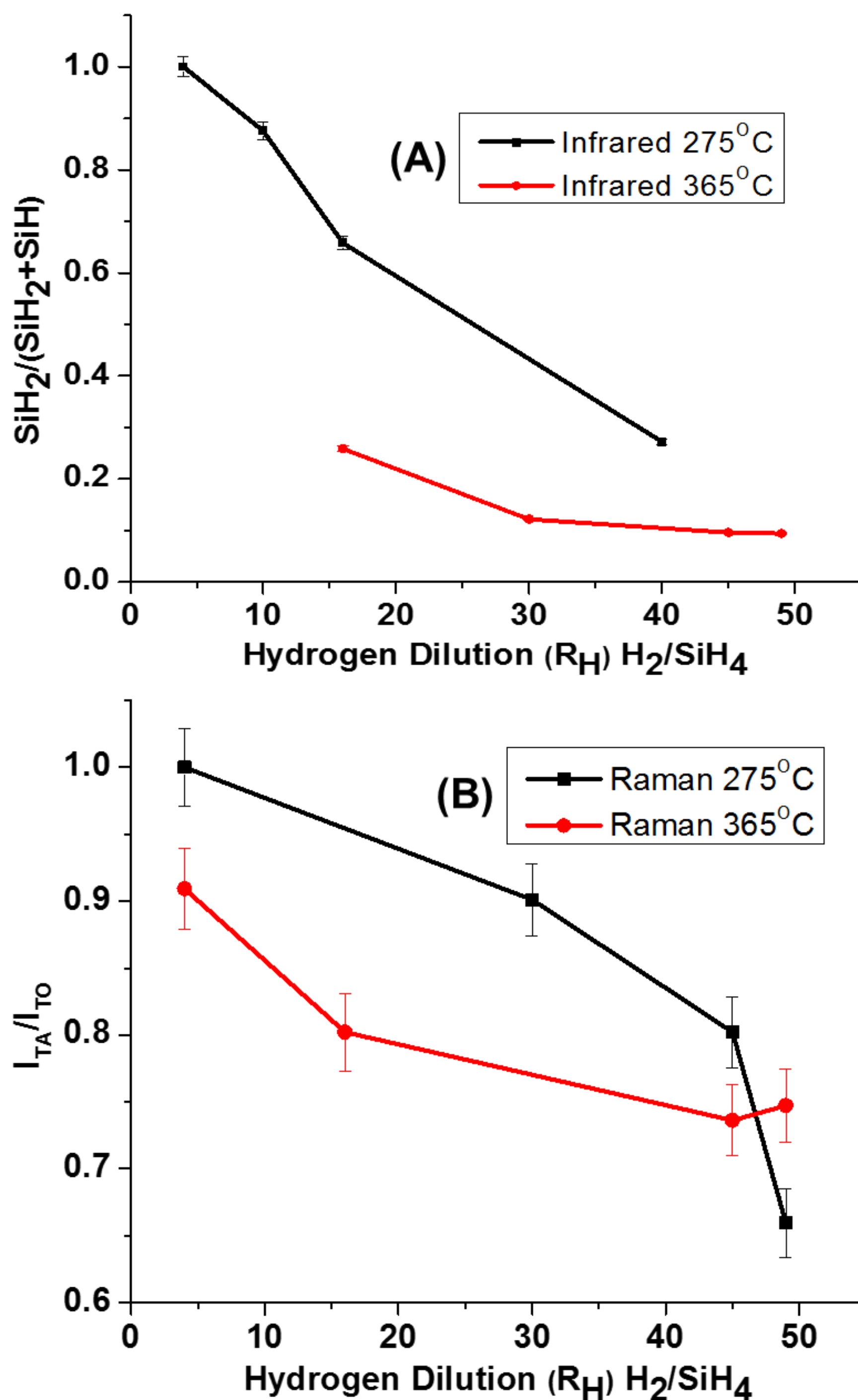

Figure 3.11: Displays values of (A) [Si:H_2]/[[Si:H]+ [Si:H_2]] ratio and (B) ITA/ITO ratio from MIR-IR and Raman analysis respectfully.

More data points are needed for hydrogen dilution and boron concentration at 275°C as well as for other substrate temperatures in order to confirm the trends shown. However, the data in Figure 3.12 does show a trend that correlates with an inverse relationship of boron concentration and hydrogen dilution with amorphous silicon lattice organization. It is also shown that there is a direct link between MIR-IR analyzation technique and Raman spectrometer analyzation.

Initially, Raman spectroscopy was used to determine the SRO and MRO as well as to help explain the reason for the change in conductivity, resistivity and Temperature Coefficient of Resistance (TCR).[2,14,18] MIR-IR spectroscopy was implemented in order to analyze chemical bonding information and to receive a better understanding of what was going on at the interatomic level on the *a*-Si:H(B) films. For example, in Figure 3.4 MIR-IR answered the questions of why amorphous silicon has a low doping efficiency and whether the boron in the film or not. MIR-IR has advantages over Raman spectroscopy in terms of increased sensitivity, less noise, and shorter analyzation time and made MIR-IR a well suited technique for this study. For example, in Figure 3.12 one can see a significant difference in percentage of the length of the error bars.

Once it was discovered that [Si:H_2]/[[Si:H]+ [Si:H_2]] ratio in peak height in the MIR-IR spectra, a direct correlation between Raman and infrared spectroscopy in terms of *a*-Si:H(B) was discovered. Thus MIR-IR can be correlated to conductivity, resistivity, and TCR when MIR-IR spectra data is used to find organization and boron concentration.

3.7 Conclusion

Boron concentration and hydrogen dilution coordination are affected by deposition substrate temperature. MIR-IR and Raman spectroscopy display that at 275°C substrate

temperature, the film is initially a more disorganized amorphous state versus a substrate temperature of 365°C. This is due to less dissociation of hydrogen in the amorphous films at lower substrate temperatures during PECVD. This is shown by a significant increase in the intensity of the peaks associated with *a*-Si:H_2 via MIR-IR analysis and an increase intensity ratio (I_{TA}/I_{TO}) in Raman analysis. Raman collaboration with MIR-IR shows that films with low SRO and MRO in Raman have a high $[SiH_2]_n/([SiH]+[SiH_2]_n)$ ratio in MIR-IR. MIR-IR can use this $[SiH_2]_n/([SiH]+[SiH_2]_n)$ ratio and intensity of *a*-Si:H(B) peaks to fine tune a- Si:H(B) films by increasing substrate temperature, hydrogen dilution or decreasing boron concentration to receive a more ordered *a*- Si:H(B) film. Lowering the substrate temperature has its benefits: more effective control of organization of *a*-Si:H(B) matrix via hydrogen dilution, lower costs, can be implemented on an already made circuit, and easier manufacturing on top of flexible substrates. Boron incorporation and bonding information shows Si_3-B-H as the only observed electrically active bonds and Si_2-B-H as the only observed non-electrically active bonds. At this time it is unknown if the protocrystalline-Si:H has been reached. More testing in verying hydrogen dilution and substrate temperatures would be beneficial in this area. There is, however, a clear trend that has been shown.

3.8 References

1. Street, R. A. Hydrogenated Amorphous Silicon. *Cambridge: Cambridge University Press* **1991***, 1st ed.*

2. Syllaios, A. J.; Tyber, G. S.; Taylor, M. F.; Hollingsworth, R. E. - Amorphous silicon thin-films for uncooled infrared microbolometer sensors. *SPIE* **2010***, 7660*, 766012.

3. Collins, R. W.; Ferlauto, A. S.; Ferreira, G. M.; Chen, C.; Koh, J.; Koval, R. J.; Lee, Y.; Pearce, J. M.; Wronski, C. R. Evolution of microstructure and phase in amorphous, protocrystalline,

and microcrystalline silicon studied by real time spectroscopic ellipsometry. *Solar Energy Mater. Solar Cells* **2003***, 78*, 143-180.

4. Skoog, Douglas A., Holler, F. James., Crouch,Stanley R., *Principles of instrumental analysis;* Brooks/Cole : Thomson Learning: Australia, 2007; .

5. Fortner, J.; Lannin, J. S. Radial distribution functions of amorphous silicon. *Phys. Rev. B* **1989***, Vol. 39, 8*, 5527.

6. Fortner, J.; Lannin, J. S. Short range order variations in amorphous silicon. *J. Non Cryst. Solids* **1988***, 106*, 128-131.

7. Lannin, J. S. Intermediate range order in elemental amorphous and liquid semiconductors. *J. Non Cryst. Solids* **1987***, 97–98, Part 1*, 203-206.

8. Danesh, P.; Pantchev, B.; Antonova, K.; Liarokapis, E.; Schmidt, B.; Grambole, D.; Baran, J. Hydrogen bonding and structural order in hydrogenated amorphous silicon prepared with hydrogen-diluted silane. *J. Phys. D* **2004***, 37*, 249.

9. He, J.; Wang, C.; Li, W.; Qi, K.; Jiang, Y. Effect of gas temperature on the structural and optoelectronic properties of a-Si:H thin films deposited by PECVD. *Surface and Coatings Technology* **2013***, 214*, 131-137.

10. Rimal, S.; Ross, N.; Pillai, K. S.; Singh, K. J.; Chyan, O. Characterization of Post Etch Residues on Patterned Porous Low-k Using Multiple Internal Reflection Infrared Spectroscopy. *ECS* **2011***, 41*, 315-322.

11. Ross, N.; Shrestha, K.; Chyan, O.; Littler, C. L.; Lopes, V. C.; Syllaios, A. J. Characterization of Boron Doped Amorphous Silicon Films by Multiple Internal Reflection Infrared Spectroscopy. *MRS Online Proceedings Library* **2013***, 1536*, 127-132.

12. Guanghua, C.; Chenzhi, Z.; Fangqing, Z.; Jinlong, C.; Wei, C. ESR and IR Studies on B-Doped Hydrogenated Amorphous Silicon-Nitrogen Film. *phys. stat. sol. (a)* **1986***, 96*, K187-K189.

13. Stutzmann, M. "Data on hydrogen in a-Si:H from diffusion and effusion studies". In *Amorphous Silicon and its Alloys*; Searle, T., Ed.; 1998; Vol. No. 19, pp p. 66.

14. Ajmera, S. K.; Syllaios, A. J.; Tyber, G. S.; Taylor, M. F.; Hollingsworth, R. E. Amorphous silicon thin-films for uncooled infrared microbolometer sensors. **2010***, 7660*, 766012.

15. Fedders, P. A.; Drabold, D. A. Simulations of boron doping in a-Si:H. *J. Non Cryst. Solids* **1998***, 227–230, Part 1*, 376-379.

16. Cai, B.; Drabold, D. A. **Theoretical Studies of Structure and Doping of Hydrogenated Amorphous Silicon**. *MRS* **2011***, 1321*, 297.

17. Uchida, Y.; Hishiya, S.; and Fujii, N. Effect of Moisture Adsorption on the Properties of Porous-silica Ultralow-K Films. *Microelectron Eng* **2006***, 83*, 2126-2129.

18. Shrestha, K.; Lopes, V. C.; Syllaios, A. J.; Littler, C. L. Raman spectroscopic investigation of boron doped hydrogenated amorphous silicon thin films. *J. Non Cryst. Solids* **2014***, 403*, 80-83.

CHAPTER 4

INVESTIGATION OF COPPER-ALUMINUM BIMETALLIC CORROSION IN HUMID CHLORIC RELATED ENVIRONMENTS *

4.1 Introduction

In modern microelectronic applications, copper replaces aluminum as the main metal used for interconnects due to their high electrical conductivity, shorter resistance-capacitance (RC) delays, and reduced electromigration.[1-3] Cu also makes lower intermetallic compounds (IMCs) and less voids growth compared to Au. Kim et al. found that the growth rate of Cu-Al IMC was 10% of that of Au-Al IMC during annealing.[4] However, when Al and Cu are used together, corrosion can be accelerated due to the standard reduction potential difference between Al (-1.66 E^o(V)) and Cu 0.34 E^o(V)), shown in Figure 4.1.[5] Corrosion effects cause serious reliability issues for integrated circuits in manufacture processing. For example, 20% of all microelectronic device failure has been attributed to corrosion.[6] Corrosion is even more of a concern for microelectronics in outdoor environments by having less protection against humidity and temperature. This is because corrosion rate is effected by temperature, moisture (relative humidity (RH)), chloride ion concentration, pH, surface area, physical imperfections, and dissimilar metal contact(s). As device dimensions become ever smaller, corrosion-related reliability will prove to be a bigger issue.

---

*This chapter is presented in its entirety from N. Ross, A. Goswami, S. Berhe, P. Lin, O. Chyan. "Study of Bimetallic Corrosion and Its Inhibition Strategy for Cu Interconnect and IC Packaging Using Micro-Pattern Corrosion Screening." SRC TECHCON, 2015, 9, with permission from SRC Techcon.

Electrode reaction	E° (volt)
$Au^+ + e^- = Au$	+1.68
$Pt^{2+} + 2e^- = Pt$	+1.20
$Hg^{2+} + 2e^- = Hg$	+0.85
$Ag^+ + e^- = Ag$	+0.80
$Cu^{2+} + 2e^- = Cu$	+0.34
$2H^+ + 2e^- = H_2$	0.00
$Pb^{2+} + 2e^- = Pb$	−0.13
$Sn^{2+} + 2e^- = Sn$	−0.14
$Ni^{2+} + 2e^- = Ni$	−0.25
$Cd^{2+} + 2e^- = Cd$	−0.40
$Fe^{2+} + 2e^- = Fe$	−0.44
$Cr^{3+} + 3e^- = Cr$	−0.71
$Zn^{2+} + 2e^- = Zn$	−0.76
$Al^{3+} + 3e^- = Al$	−1.67
$Mg^{2+} + 2e^- = Mg$	−2.34
$Na^+ + e^- = Na$	−2.71
$Ca^{2+} + 2e^- = Ca$	−2.87
$K^+ + e^- = K$	−2.92

Figure 4.1. Standard reduction potentials of selected metals.[5]

Bimetallic corrosion, also known as galvanic corrosion, is the acceleration of corrosion due to an electrochemical process in which one metal is oxidized by giving its electrons to the more noble metal via redox reaction. When two dissimilar metals touch one another in the presence of an electrolyte, an electrical current enabled by this re-dox reaction can form due to the difference in standard reduction potentials.

Bimetallic corrosion effects can cause serious reliability issues such as Cu wire bonding lift-off due to severely corroded Al pads especially in more demanding automotive applications. There are various common types of corrosion observed on aluminum metal such as pitting corrosion, intergranular (mud crack) corrosion, crevice corrosion, and stress corrosion. The most commonly observed corrosion defects in Al/Cu interconnects are intergranular (mudcrack) and pitting corrosion.[5]

To understand the mechanism of corrosion, extensive research has been done on Al-Cu IMCs.[7-11] Several studies revealed the growth and formation of different IMCs of CuAl, $CuAl_2$, $CuAl_4$, and Cu_9Al_4.[12-17] Uno et. al. revealed that IMCs Al_4Cu_9 and Al_2Cu, are the most prone to corrosion.[16,18] It has also been reported that diffusion of halogen ions towards the ball bond center through cracks caused a corrosion reaction between halogens (Cl, Br) and IMCs.[16,17] Although studies of Al/Cu IMCs is important and is studied heavily for exploration of corrosion process on Cu interconnects, Al-Cu IMC formation is slow and minimal.[4,19] Research with Al and Cu Bimetallic corrosion is lacking even though devices with a Cu wire connect to an Al pad are common in industry. For example, Tomohiro Uno from Nippon Steel Corporation[16] focuses on Al/Cu IMC as the weak link and starting place of the corrosion in the Cu wire bonded to Al pad devices. However, Uno only showed examination of the corrosion "postmortem" by showing transmission electron microscopy (TEM) images of the area after the corrosion has taken place. Uno mentions oxygen reduction reaction (ORR) in the corrosion mechanism, however Uno doesn't mention how he observing the ORR. Uno goes on to state that palladium coating on the copper wire will slow down corrosion rate.[16] Although Uno and other researchers in the area of made advancements in the area of Al/Cu corrosion it is not observed where the corrosion starts, how corrosion progresses, or how it interacts with effects of Al/Cu bimetallic interface.

Therefore, a more relevant experimental technique mimicking the real device assembly would give a better understanding to the corrosion mechanism. In this chapter, it is reported that Al-Cu bimetallic micropattern corrosion screening technique delivers a more relevant and direct link to the real devices and would reveal a more detailed understanding to the mechanistic chemical transformation and corrosion process. Previously, we reported that micropattern corrosion testing methodology is effective for evaluating bimetallic corrosion of Cu interconnects when exposed to chemical mechanical planarization (CMP) and post CMP cleaning conditions. It also showed that Cu/Ru exhibit enhanced corrosion compared to Cu/Ta.[20] A similar micropattern corrosion testing methodology combined with electrochemistry and microscopy are used to investigate Al/Cu corrosion screening in various different chemical conditions. Corrosion screening metrology utilizing micro-corrosion test patterns provides rapid in-situ corrosion evaluations relevant to Cu interconnect structure and IC packaging. Copper micro dots were directly sputtered on aluminum substrate and detailed corrosion process was investigated under different corrosion variables (temperature, moisture, chloride ion concentration, and pH). This chapter is going to discuss the microscopic and electrochemical corrosion progression morphology of bare aluminum and copper microdot on aluminum substrate under acidic chloride environment. It is important to see the total progression of the corrosion from start to finish in order to understand and prove what the issue is. It will also discuss the evolution of hydrogen gas and mechanistic insights that would lead to more effective prevention of aluminum bond pad corrosion.

In this chapter, we report corrosion progression morphology of aluminum-copper alloy and Cu/Al bimetallic contact under acidic chloride solutions. Three main goals of this Cu/Al bimetallic corrosion project are to recreate Cu/Al bimetallic corrosion seen in industry's Cu wire bonded to Al pad devices, determine the Cu/Al bimetallic corrosion mechanism, and find a way to slow down

if not stop this bimetallic corrosion. These three goals have been obtained and this chapter will explain the journey in obtaining these goals.[21]

4.2 Experimental

4.2.1 Micropattern Corrosion Sputtering Metrology

Whenever Al or Al (0.5% wt. Cu) is mentioned in chapter 4 it is referring to a 1.2 µm thick Al (0.5% Cu by weight)/ 5 nm Ta/ SiN substrate. The Al bonding pad alloy with 0.5% Cu by weight is commonly used to minimize electromigration defects on the Cu wire bonded to Al pad devices.[22] Thus the Al tested in this study also has 0.5% Cu by weight to make the experiments as close to “real world” conditions as possible. Only in section 4.9 (Direct current measurement) is the Al tested using a pure Al substrate versus 1.2 µm thick Al (0.5% Cu by weight)/ 5 nm Ta/ SiN substrate sample.

Micropattern corrosion screening allows for a cost and time effective metrology to study Al/Cu bimetallic corrosion screening in various chemical environments. Micropattern corrosion screening metrology is shown in Figure 4.2. A 1.2 µm thick Al (0.5% Cu by weight)/ 5 nm Ta/ SiN substrate was used for the Al samples as well as the same substrate deposited by Cu dot samples. Circular micropatterns of Cu (100 nm thick, 130 um in diameter) were deposited on 1.2 micron thick Al (0.5% Cu)/ 5 nm Ta/ SiN substrate through a contact mask using a RF sputter Desktop Pro Denton Vacuum Sputtering System.

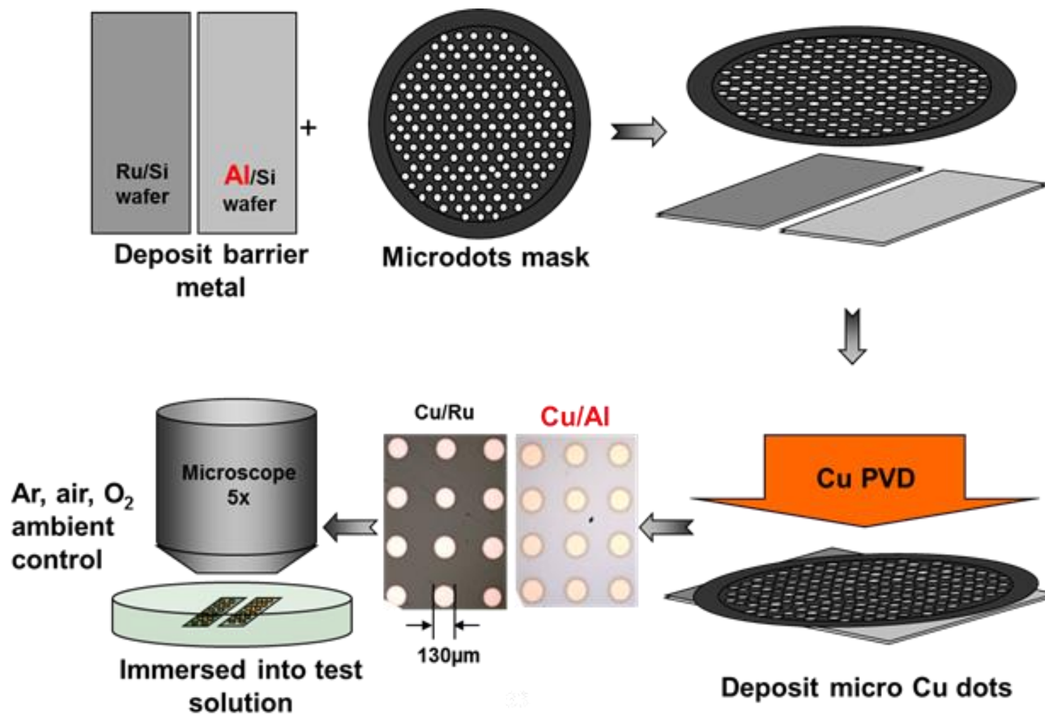

Figure 4.2: Micropattern corrosion screening product metrology.

4.2.2 Industry Wire-Bonded Samples

Wire-bonded samples were given to Dr. Chyan's research group by Freescale to study bimetallic corrosion on finished product. An image of a wire-bonded sample is shown in Figure 4.3. Each die has typically 100-200 Al pads with a Cu wire bonded to each one. At the Al pad, copper is attached by forming a copper ball bond. Two other types of samples were also given: Cu/Pd alloy and Au wire instead of Cu wire. The second bond is the bond between the Cu wire and the substrate with Au and Ni. The second bond on the substrate is Au on top and Ni underneath (not exposed). Between the die and substrate, there is nonconductive adhesive with silica filler. The back side of the substrate also has Ni/Au(top) pads. These chips are to be put into automobiles. A protective layer made out of epoxy will encapsulate the die to protect it from environmental factors such as humidity. However, there is usually 5-15 parts per million (ppm) Cl^- contaminants

within the epoxy. Any damage to the protective epoxy capsule will let in moisture. Moisture combined with Cl^- provides a perfect environment for an electrochemical cell between the Al pad and Cu ball connection.

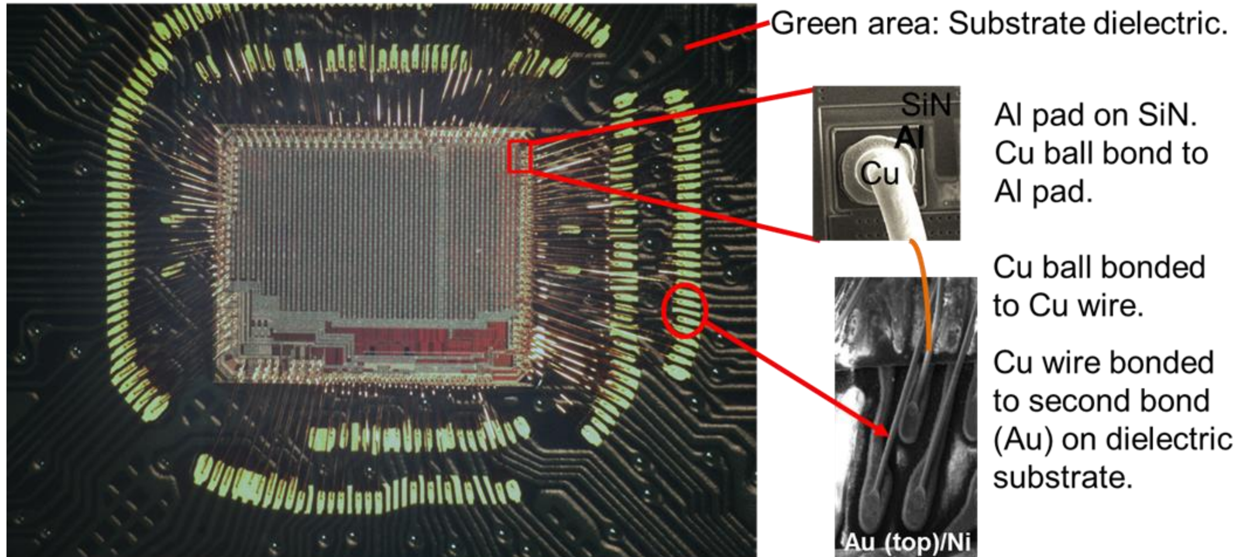

Figure 4.3: Wire-bonded sample structure.

Microchips with Cu (Cu-Al) and Pd coated Cu (Pd/Cu-Al) wire bonded to Al pads have a wire thickness of ~22 µm and a ball thickness of ~50 µm. Al pad is ~60 µm wide by ~60 µm long by 1.2 µm thick. The dimensions are shown in Figure 4.4. The visual investigation of in situ corrosion process was carried out using a metallurgical Nikon, eclise ME600 microscope, infinity 2-3C powerscope, and EOS Rebel T5i Cannon DSLR camera. During optical imaging, the samples were immersed in solutions with 0-20 parts per million (ppm) of sodium chloride and 3.5-7 pH with sulfuric acid. Solutions need to be optically clear for visual investigation. These solutions

were prepared with 18.2 Mega Ohm and 2ppb organic contaminant ultra-pure water (UPW) produced by an integral-3 UPW filtration system.

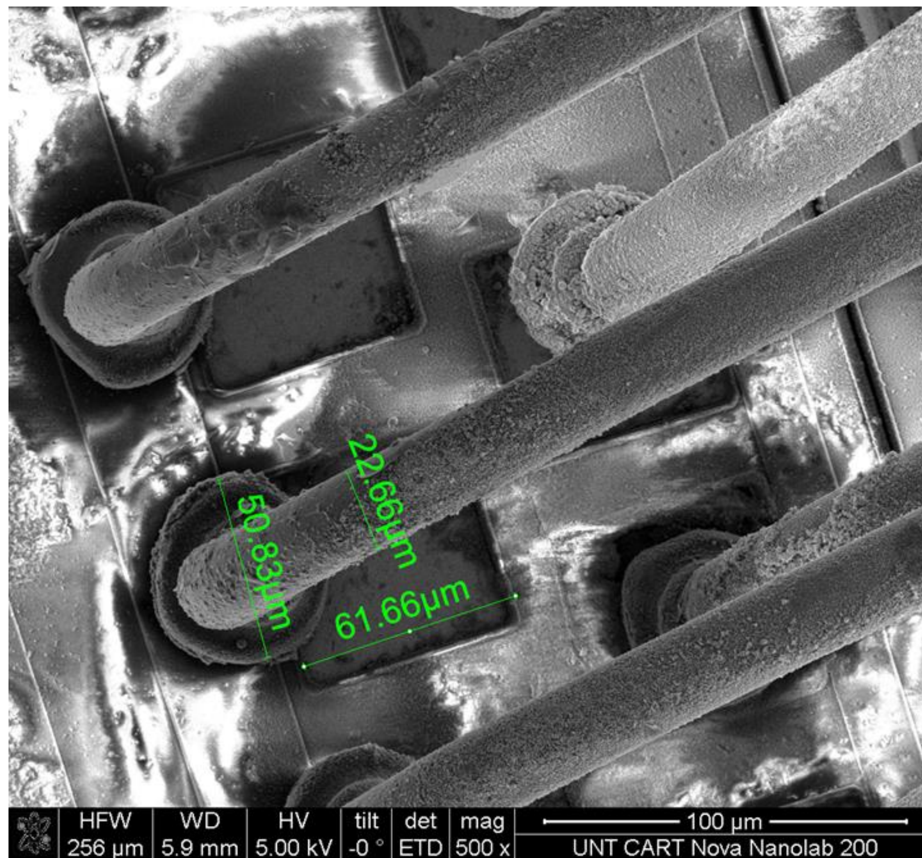

Figure 4.4: SEM image of wire-bonded sample dimensions.

4.2.3 Time Lapse Screening Metrology

With the amount of variables to test, it is necessary to efficiently test and analyze a large number of samples. The variables are as follows:

- Concentration on ions: 0-100ppm of Cl^-, F^-, and Na^+

- pH: 0-10 pH. pH was reached by adding sulfuric acid to lower pH and used sodium hydroxide to increase pH.
- Pressure: 1 and 2 atm
- Temperature: 22ºC, 85ºC, 121ºC.
- Material of metal
  - Al (0.5% Cu by weight)
  - Pure Al
  - Cu dot on Al (0.5% Cu by weight)
  - Cu dot on pure Al
  - Wire-bonded samples
  - Cu wire/ball attached to Al pad.
  - Pd/Cu wire/ball attached to Al pad.
  - Au wire/ball attached to Al pad.

To solve this large volume of variables issue, immersion corrosion screening was implemented with time lapse recording software. Immersion corrosion screening set up allows for 15 samples to be analyzed at a time, giving an efficient method in testing and analyzing larger numbers of samples at once. Web cam and a Cannan EOS Rebel T5i DSLR camera was used to take the optical images simultaneously yielding a total of 30 samples at a time being studied under time lapse recording. When a set of variables show repeatable mudcrack formation, further processing via powerscope, microscope, scanning electron microscope (SEM), and energy dispersive x-ray (EDX) studies was done.

Environmental stress corrosion test chamber was used to test temperature, pressure and humidity variables. This chamber is a pressure cooker which can hold up to 4 liters of water and

is placed into an oven. The temperature is 121°C and increasing the total pressure by one creates a pressure of 2 atm inside the pressure cooker. 15-30 samples can be placed inside at a time.

After being in the environmental chamber for 2 days the samples were then analyzed via DXM 1200 optical microscope. The Nikon microscope has magnification lens of 50x, 100x, 500x, and 1000x. The Nikon microscope has time lapse software, ACT, that allows for higher magnification images for the time lapse application.

4.2.4 Tafel Plots, SEM, EDX, and XPS

Corrosion currents and potentials were measured by Tafel plot technique and complemented well the micropattern corrosion optical imaging time lapse results to demonstrate the Al/Cu bimetallic corrosion rate and mechanism. A model 2400 potentiostat by CH Instruments, USA was used to obtain the Tafel plots. The metal electrodes (d=5mm) were polished down to 0.5 µm mirror polishing and sonicated in 18.2 Mega Ohm UPW. Three-electrode system with Pt as counter and $Hg/HgSO_4$ as reference electrodes were employed in a glass cell to obtain the Tafel plots in a corresponding solutions used in micropattern corrosion screening. A VersaProbe™ Scanning XPS Microprobe was used to receive chemical state and electronic state of elements that exist within the samples made in house and from industry. The FEI Nova 200 NanoLab with a dual column ultra-high resolution field emission scanning electron microscope (SEM) and focused ion beam (FIB) used to receive SEM imaging. Surface chemical composition information was obtained by energy dispersive X-ray spectroscopy (EDAX) system.

4.3 Al Corrosion Progression

An acidic chloric solution was utilized to mimic real world environments of an epoxy-embedded microchip device in an automobile application. The acidic chloric solution has a specific effect on Al morphology over time. For example, no corrosion was observed for at least fifteen days when a sample was submerged in a 0 ppm Cl^- solution whereas it took only ten days for 2ppm Cl^- and two days for 5ppm Cl^- to see a 10% surface dendrite corrosion on a Al (0.5% Cu) sample. The Al surface has a higher corrosion rate when chloride solution is slightly acidic in the 4-6 pH range. This is due to the acidic environment creating a positive charge on the Al surface (Lewis acid, $Al_2AlOH_2^+$) that will cause the Cl^- anion (Lewis base) to bind with the now positive Al surface. When the Al oxide is in a basic solution, the surface (Al_2AlO^-) is negatively charged and the ion-ion repulsion forces are no longer favored for attracting Cl^-.[10,23,24]

Corrosion progression morphology was studied using microscopy and revealed that the corrosion starts as surface roughening which evolves into a dendrite structure and later continues to grow into a mud-crack type corrosion. Figure 4.5 is a graph showing the change in the corrosion morphology and aluminum to oxygen ratio as the corrosion progresses through different stages. The image labeled "as is" has not been introduced to the acidic chloride solution. After approximately 2 hours of the Al (0.5% Cu by wt.) sample in 5ppm Cl^- 5pH solution obvious surface roughness can be seen on the Al (0.5% Cu by wt.) surface. Then, at around 12 hours dendrite corrosion appears on the Al (0.5% Cu by wt.) surface. At around 48 hours more than 10% of the sample is corroded with dendrite corrosion. An example of a sample at more than 10% corrosion is seen in Figure 4.5, labeled as dendrite. After significant (more than 10%) dendrite corrosion has set in, the corrosion penetrating the Al surface becomes more apparent as "cracks" become larger and easier to see even with low resolution microscopy. The oxide content increases as the aluminum surface goes through progression of morphological change. There is a slow decrease in

Al:O ratio in the beginning when the passivating oxide is under initial attack (induction period). Then a steeper slope follows where the Al:O ratio declines dramatically indicating the breaking down of the passivating oxide and a fresh Al under layer is under attack. The mud-crack morphology comes as a late/severe corrosion with the highest oxygen ratio coming from within the crack area. High resolution SEM picture showed that the early stage of corrosion with dendritic formation occurs mostly at the grain boundary. This could possibly be due to defects and a higher copper content at the grain boundary.[5,25]

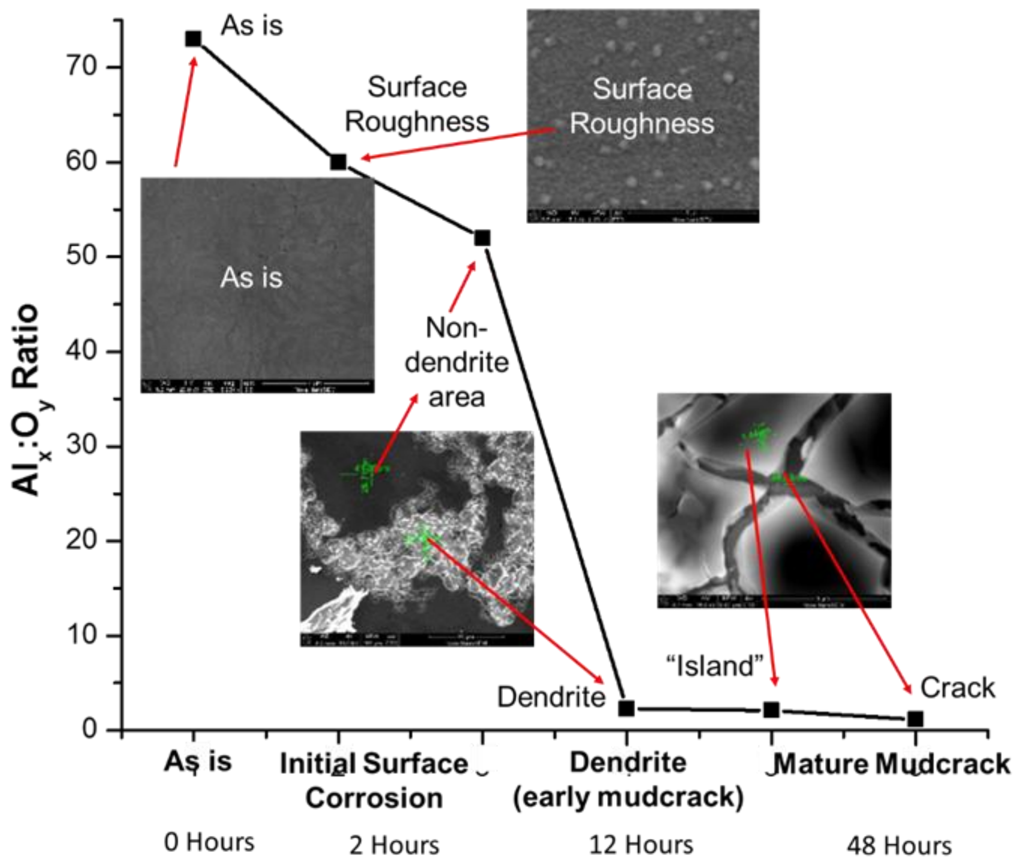

Figure 4.5: Morphological Progression of Corrosion. Left to right SEM images of; As is, initial surface roughness, dendrite formation and mudcrack (severe corrosion). All samples are of 1.2 micron thick of Al (0.5% Cu by wt.)/ 5 nm Ta/ SiN substrate.

To locate the starting point is an important task when studying corrosion. Al (0.5% wt.) samples were submerged in an acidic chloride solution and taken out at certain time intervals. The time was narrowed down by information obtained by time lapse experiments. The starting location of corrosion was identified on the grain boundaries shown in Figure 4.6. This is most likely due to the fact that gain boundary is the highest energy state, and Cu is at a higher percentage at these grain boundaries.[22,26]

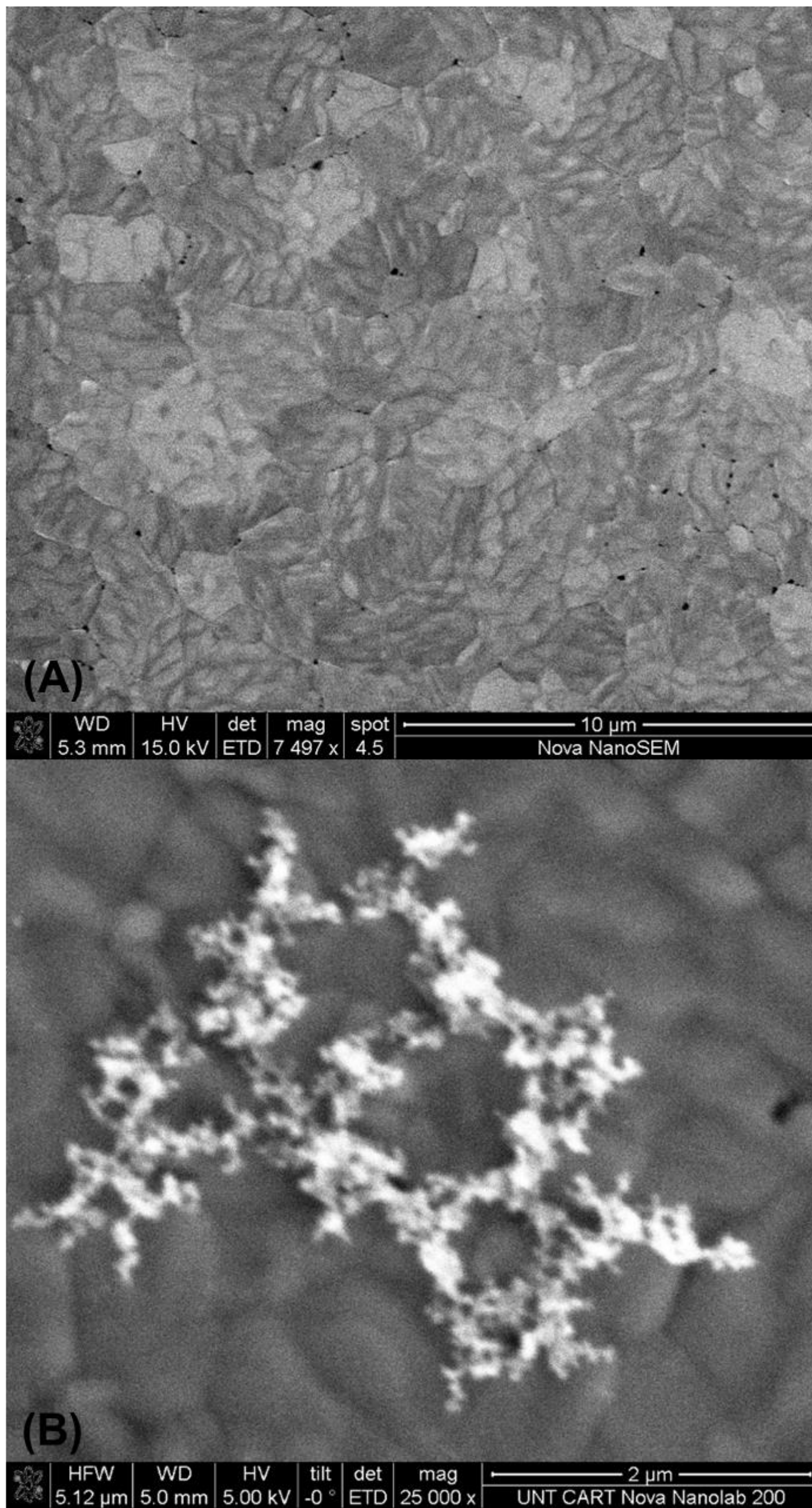

Figure 4.6: 12 kÅ Al/ 500 Å Ta/ 2000 Å SiN (A) as is. (B) in 5ppm Cl^- 5pH for 2 hours.

Dendrite formation on the Al surface is the morphology after surface roughness and before mudcrack formation. Further analysis of dendrite formation at higher magnification that one can see with SEM imaging shows that the corrosion is already penetrating the Al surface, shown in Figure 4.7. Dendrite is confirmed to be the early stages of mudcrack formation, thus dendrite is considered “early mudcrack” formation. This is an important finding by noticing that it is this stage that the corrosion is significantly penetrating the Al surface.

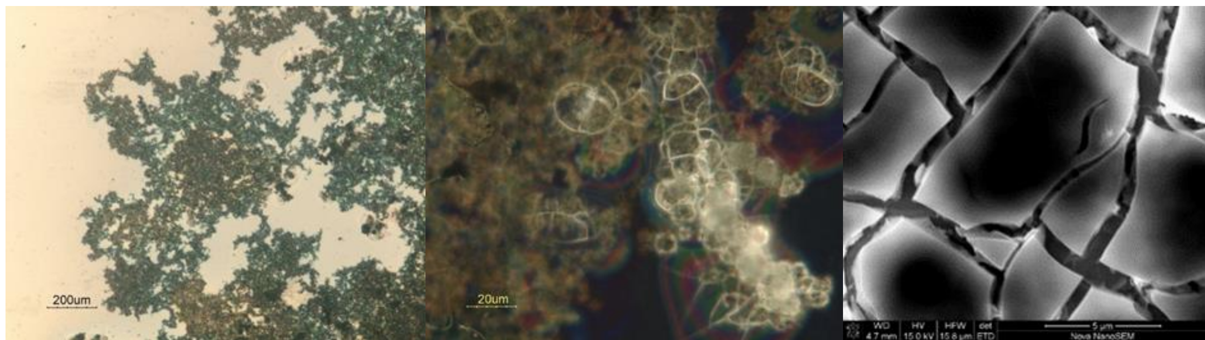

Figure 4.7: All three images are of the same sample: 12 kÅ Al/ 500 Å Ta/ 2000 Å SiN in a 20ppm Cl^- solution at 4pH (H_2SO_4) for 96 hours. Image on the left is taken at 50X maginification by a DXM 1200 Nikon Optical Microscope. Middle image is taken via Nikon microscope at 500X magnification. Image at the right is taken by Nova NanoSEM 230.

4.4 Al Corrosion Variables

4.4.1 Chloride Concentration, pH of Solution, and Time

As Figure 4.7 shows mudcrack corrosion will be produced under 20 ppm Cl^- at 4pH over several days on the Al(0.5 Cu wt%) surface. The variables of chloride concentration, pH, time in solution and temperature were studied at great lengths. Table 4.1 shows the immersion corrosion screening results on Al(0.5 Cu wt%) surface at different pH and chloride concentrations. Going from left to right column, the left most is the total number of samples tested for each set. Next is pH from 4-8 pH. Following that is parts per milion (ppm) of chloride. The next 15 columns

represent the number of days the experiement elapsed and the percent of samples that produced mudcrack corrosion on 10% or more of the surface area of the sample. The samples where analyzed by Nikon microscope.

The 4-6 pH range was tested thoroughly to simulate real world conditions. The pH will vary from carbon dioxide in rural areas, to sulphur dioxide, sulphur trioxide, nitrous compounds, hydrogen sulphide and chloride ions, and ammonium ions in industrial areas. Exposure tests have shown a corrosion rate for steel of 5 um per year at Nkpoku, a rural area in Nigeria, versus 90 um per year in Sheffield, an industrial area in the UK. Areas near the shore line can be considerably higher.[5] Chloride was chosen due to the fact that chloride ion is the main ion in this corrosion system. This is because the chloride ion is most commonly found next to bodies of salt water and roads in colder climates. The protective layer made out of epoxy encapsulates the die of the microchip to protect the chip from environmental factors such as humidity. However, it was found that 5-15 ppm Cl^- contamination within this epoxy. In an epoxy capsule, the difference in water vapor pressure between the atmosphere inside and outside of the epoxy capsule is enough to cause permeation and leakage of water into the die. Any damage or increase in temperature to the capsule will allow for serious moisture ingress to occur.[27] Two different metals, Cl^- (salt bridge), and solvent (moisture) makes an electrochemical cell within the encapsulated die area. This allows for the severe Al mudcrack corrosion.

			Time (days)	1	2	3	4	5	6	7	8	9	10	11	12	13	14	15
# Tested	pH	PPM Cl-																
10	3.5	0		0	0	0	0	0	0	0	0	0	0	0	0	0	0	0
2	3.5	0.5		0	0	0	0	0	0	0	0	0	0	0	0	0	0	0
2	3.5	1		0	0	0	0	0	0	0	0	0	0	0	0	0	0	0
2	3.5	1.5		0	0	0	0	0	0	0	0	0	0	0	0	0	0	0
2	3.5	2		0	0	0	0	0	0	0	0	0	0	0	0	0	0	0
16	4	1		0	0	0	0	0	0	0	0	0	0	0	0	0	0	0
2	4	1.5		0	0	0	0	0	0	0	0	0	0	0	0	0	0	0
2	4	2		0	0	0	0	0	0	0	0	0	50	50	50	50	50	50
11	4	3		0	0	0	9.09	9.09	9.09	9.09	9.09	9.09	9.09	9.09	9.09	9.09	9.09	9.09
16	4	5		0	18.8	18.8	25	25	31.3	31.3	31.3	31.3	31.3	31.3	31.3	31.3	31.3	31.3
8	4	10		0	25	37.5	37.5	37.5	37.5	37.5	37.5	37.5	37.5	37.5	37.5	37.5	37.5	37.5
9	4	20		0	66.7	66.7	66.7	66.7	88.9	88.9	88.9	88.9	88.9	88.9	88.9	88.9	88.9	88.9
2	4	50		0	100	100	100	100	100	100	100	100	100	100	100	100	100	100
15	4.5	0		0	0	0	0	0	0	0	0	0	0	0	0	0	0	0
1	4.5	0.5		0	0	0	0	0	0	0	0	0	0	0	0	0	0	0
4	4.5	1		0	0	0	0	0	0	0	0	0	25	25	25	25	25	25
1	4.5	1.5		0	0	0	0	0	0	0	0	0	0	0	0	0	0	0
3	4.5	2		0	0	100	100	100	100	100	100	100	100	100	100	100	100	100
1	4.5	3		0	0	0	0	0	0	0	0	0	0	0	0	0	0	0
6	4.5	5		0	0	0	0	0	0	0	0	0	0	0	0	0	0	0
6	4.5	10		0	33.3	33.3	33.3	33.3	33.3	33.3	33.3	33.3	33.3	33.3	33.3	33.3	33.3	33.3
5	4.5	20		0	100	100	100	100	100	100	100	100	100	100	100	100	100	100
2	4.5	50		0	100	100	100	100	100	100	100	100	100	100	100	100	100	100
5	5	0		0	0	0	0	0	0	0	0	0	0	0	0	0	0	0
1	5	0.5		0	0	0	0	0	0	0	0	0	0	0	0	0	0	0
16	5	1		0	12.5	12.5	12.5	12.5	12.5	12.5	12.5	12.5	12.5	12.5	12.5	12.5	12.5	12.5
1	5	1.5		0	0	0	0	0	0	0	0	0	0	0	0	0	0	0
1	5	2		0	0	0	0	0	0	0	0	0	0	0	0	0	0	0
10	5	3		0	0	0	0	0	0	0	0	0	30	30	30	30	30	30
15	5	5		0	13.3	13.3	13.3	13.3	13.3	13.3	13.3	13.3	13.3	13.3	13.3	13.3	13.3	13.3
7	5	10		0	28.6	28.6	28.6	28.6	28.6	28.6	28.6	28.6	28.6	28.6	28.6	28.6	28.6	28.6
6	5	20		0	100	100	100	100	100	100	100	100	100	100	100	100	100	100
2	5	50		0	100	100	100	100	100	100	100	100	100	100	100	100	100	100
1	5.5	0		0	0	0	0	0	0	0	0	0	0	0	0	0	0	0
1	5.5	0.5		0	0	0	0	0	0	0	0	0	0	0	0	0	0	0
1	5.5	1		0	0	0	0	0	0	0	0	0	0	0	0	0	0	0
1	5.5	1.5		0	0	0	0	0	0	0	0	0	0	0	0	0	0	0
1	5.5	2		0	0	0	0	0	0	0	0	0	0	0	0	0	0	0
2	7	0		0	0	0	0	0	0	0	0	0	0	0	0	0	0	0

Table 4.1: Excel sheet of samples tested in Immersion Corrosion Screening experiment at room temperature. Explanation from left column to the right. # Tested is the total number of 12 kÅ Al/ 500 Å Ta/ 2000 Å SiN samples tested at the certain pH and ppm of chloride shown on the following two columns. Percentage of samples with 10% surface area corrosion on Al surface of the sample within Day 1 to Day 15.

The trend of mudcrack formation due to concentration of chloride and pH testing is more easily identified in Figure 4.8 3D plot. If pH is between 4-6 the higher the concentration of chloride the more likely there will be mudcrack corrosion. Chloride ion (Lewis base, electron donor) is

known to remove the top Al oxide protective layer by replacing $Al(OH)_3$ (Lewis acid, electron acceptor) to $AlCl_3$ allowing the Al layer underneath to become exposed to moisture thus the pure Al will oxidize and expand. This volume expansion from pure Al to $Al(OH)_3$ increases from 9.993 cm^3/mol of Al to 32.231 cm^3/mol of $Al(OH)_3$ which is a volume expansion of 320%. This expansion causes cracks in the Al bulk to the surface to make room. Crack exposes pure Al further down in the bulk to repeat the process over. With a higher concentration of chloride the faster and wider spread this process will proceed. The mudcrack corrosion will usually happens at 4-6 pH due to a solution at the 4-6 pH range that makes the $Al(OH)_3$ layer positively charged and is more likely to attract chloride ions.[7] If the solution is neutral, the chloride ions are not as attracted to the $Al(OH)_3$ surface. A solution that is basic will take hydrogen from the $Al(OH)_3$ surface to create $Al(O)_3^{3-}$ which creates a negatively charged Al surface, thus repelling the chloride away. Solutions more acidic than pH 4 will attract the most of chloride ions to the highly positively charged solution itself rather than the $Al(OH)_3$ surface. In this research study, corrosion has been seen in pH ranges other than 4-6pH. This is due to pitting and microenvironments in which the pH can change allowing the corrosion process to start. Corrosion has been seen at other pH ranges than 4-6 pH; however, most of the cases of severe mudcrack corrosion has been between 4-6pH and ≥5ppm Cl^-.

Figure 4.8: 3D graph of the data shown in figure # (excel sheet of the Immersion Corrosion Screening.) X-Axis = pH, Y-Axis = ppm Chloride, and Z-Axis = Percent of Occurrence of Corrosion at 10% or higher. 3D graph (A) is at the 2 day mark and the 3D graph (B) is at the 10 day mark.

4.4.2 Temperature and Pressure

The higher the temperature, the faster the corrosion rate for Al oxide in acidic chloric solutions. One exclusion from this is hot deserts due to low moisture.[5] The reaction rate approximately doubles for every $10^{o}C$ rise in temperature. If temperature falls below the dew point, the air becomes saturated with water vapor, and free water droplets condense on any exposed surfaces.[5] Moisture is a key factor in corrosion. It has been shown that even with encapsulation with polymeric materials, permutation and leakage still let in moisture due to difference of water vapor pressure between the inside and outside atmosphere of the package. In fact, the polymeric materials themselves are permeable to moisture and will absorb moisture if they are exposed to humid environments for extended period of time.[27,28]

To study the effects of temperature and pressure on Al corrosion under acidic chloride solutions, a pressure cooker was modified to do pressure cooker screening at $121^{o}C$, 100% humidity, and 2 atm total pressure for two days. The chloride solutions where placed on the Al(0.5% Cu by wt.) samples via micropipette (35 uL) to dry. The Al(0.5% Cu by wt.) samples were on a rack inside the pressure cooker and not submerged in the water. Similar to immersion corrosion screening, 10% mudcrack corrosion is seen primarily in the 4-6 pH range and at $\geq$ 5ppm Cl^{-}. Temperature increases corrosion rate and has been seen when comparing at the two day mark on Table 4.1 and Table 4.2. Higher percentages of $\geq$10% mudcrack corrosion is seen when comparing at the two day mark with Table 4.1 and Table 4.2. This is to be expected since an increase in temperature increases corrosion rate on most types of corrosion.[5] The 3-D figures in Figure 4.11 (A) is to better show the corrosion trend of Al(0.5% Cu by wt.). In Figure 4.9 (B) focuses on $\leq$5% ppm Cl^{-} at 4-5pH.

Pressure Cooker		121oC	2 ATM		2	2	2	2	2	2	2			2					
100% RH	48 Hour	Date	7/18/	7/21/	8/4/	8/11/	8/13/	8/19/	8/23/	8/29/	9/1/	9/4/	9/7/	9/12/	9/15/	9/18/	Total with	# Tested	10% / # Tested
pH	ppm Cl	Wafer	IH	IH	IH	IH	IH	IH	IH	IH	IH	FS	FS	IH	FS	FS	>10%		
		acid	AA	AA	AA	AA	AA	AA	AA	AA	AA	AA	AA	SA	SA	SA	Corrosion		
4	0		0	0	0	0	0	0	0	0	0	0	0	0	0		0	22	0
4	1		1	0	0	0		2	0		0	0	0	0	0	0	3	18	16.67
4	2											0	1				1	2	50
4	3								0		2	0	0	0	0	0	2	10	20
4	4											0	1				1	2	50
4	5		1	1	2	0		0	0		2	1	0	2	0	0	9	18	50
4	10		1	0	2	0		0	2		2			2	0	0	9	14	64.29
4	20		1	1	2	0		2	2					2	0	1	11	14	78.57
4	50		1														1	1	100
4	100		1														1	1	100
4	300		1														1	1	100
4	1000		1														1	1	100
4.5	0		0				0			0		0	0				0	9	0
4.5	1		0									0	0				0	3	0
4.5	2											0	0				0	2	0
4.5	3											0	0				0	2	0
4.5	4											0	0				0	2	0
4.5	5		0									0	0				0	3	0
4.5	10		1														1	1	100
4.5	20		1														1	1	100
4.5	50		1														1	1	100
4.5	100		1														1	1	100
4.5	300		1														1	1	100
4.5	1000		1														1	1	100
5	0		0				0			0		0	0	0	0		0	10	0
5	1		0									0	1	0	0	0	1	7	14.29
5	2											0	0				0	2	0
5	3											0	0	0	0	0	0	6	0
5	4											0	0				0	2	0
5	5		1									0	0	0	0	0	1	6	16.67
5	10		1											2	0	1	4	6	66.67
5	20		1											0	0	1	2	5	40
5	50		1														1	1	100
5	100		1														1	1	100
5	300		1														1	1	100
5	1000		1														1	1	100
7	0			0			0			0							0	5	0
7	1			0													0	1	0
7	5			0													0	1	0
7	10			0													0	1	0
7	20			0													0	1	0
10.5	0				0		0			0							0	5	0
10.5	1				0												0	1	0
10.5	5				0												0	1	0
10.5	10				0												0	1	0
10.5	20				0												0	1	0
																	0	1	0
Key	SA= Sulfuric acid			FS = free scale wafers												Total	58	198	29.29
	FS SA = Free scale wafers with Sulfuric acid																		
	2000A SiN/ 500 a Ta/ 12KA																		
	white = in house wafers (IH)					AA= acetic acid													
	Si substrate/7nm TA/ 1micron Al																		

Table 4.2: Excel sheet of samples tested in Pressure Cooker Screening experiment. Samples were subjected to 121°C for 2 days. The pressure is increased by about 1 atm at this temperature totaling to 2 atm of pressure total.

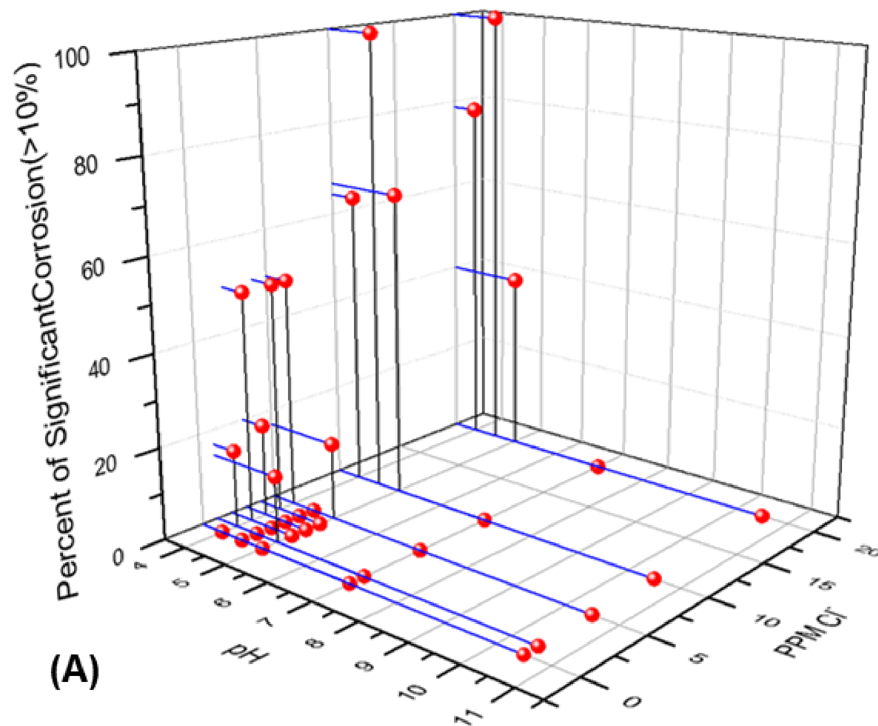

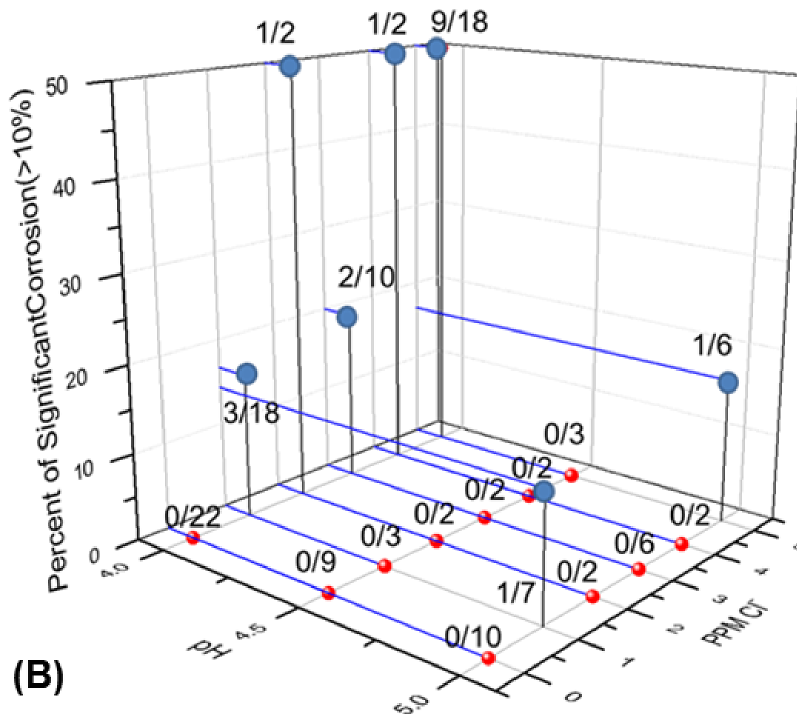

Figure 4.9: 3D graph of the data shown in Figure 4.10 X-Axis = pH, Y-Axis = ppm Chloride, and Z-Axis = Percent of Occurrence of Corrosion at 10% or higher. (A) Shows the full system, (B) shows only ≥5 ppm Cl^- and 4-5pH system.

4.5 Cu/Al Bimetallic Effect on Corrosion

Exploring the impact of copper on corrosion of aluminum is crucial because the actual Al pad in the microchip devices is directly bonded to a copper wire. To further study the impact of copper on aluminum corrosion, a bimetallic aluminum-copper interface was prepared by sputtering copper microdots on aluminum substrate in a PVD chamber. The Cu/Al bimetallic effect on corrosion was studied in an acidic chloride solution. Three important observations from this study are; 1. Chloride ion concentration plays a key role in the corrosion process. 2. The corrosion starts at the aluminum – copper interface with a release of hydrogen gas. 3. Once corrosion starts at Al/Cu interface, it continues to extend primarily to the Cu/Al interface and aluminum area**.** The copper dots are usually the last to corrode. This is the first recorded data revealing bimetallic corrosion of Cu/Al interface producing hydrogen evolution.

In Figure 4.10 below there are 5 images from a microscopy time lapse experiment, 1 SEM image and 1 EDX spectrum. In each Nikon microscope image there is, 1.2 micron thick of Al (0.5% Cu) substrate on the left and 100nm thick Cu dot on Al (0.5% Cu) substrate on the right. Both samples were placed in a 2ppm Cl- solution at 5pH. Within ~7 minutes corrosion appeared at the Cu/Al intermediate location. Dendrite corrosion extended outwards on the Al substrate. Within 10 minutes, H_2 bubbles became visible with the microscope time lapse image. Corrosion continue to spread, attacking Cu/Al intermediate and Al surface. In approximately 8 hours 10% of the Cu dot sample was corroded. At the 44 hour mark, Cu dot on Al sample had most of the Al substrate corroded with only pitting and surface roughness viable on the Al only sample to the left. This shows a significant increase in corrosion rate due to Cu/Al bimetallic effect. For example it took about 12 hours for noticeable corrosion to be observable via the Nikon microscope on a Al(0.5% wt. Cu) surface submerged in a 5ppm Cl^- 5pH solution. SEM image and EDX spectrum

of the sample at 44 hour mark is displayed in Figure 4.10. The Al: O_x ratio is close to 1:2, this high oxide ratio shows that the sample is at the severe corrosion stage in which the corrosion has not only corroded horizontally but also vertically.

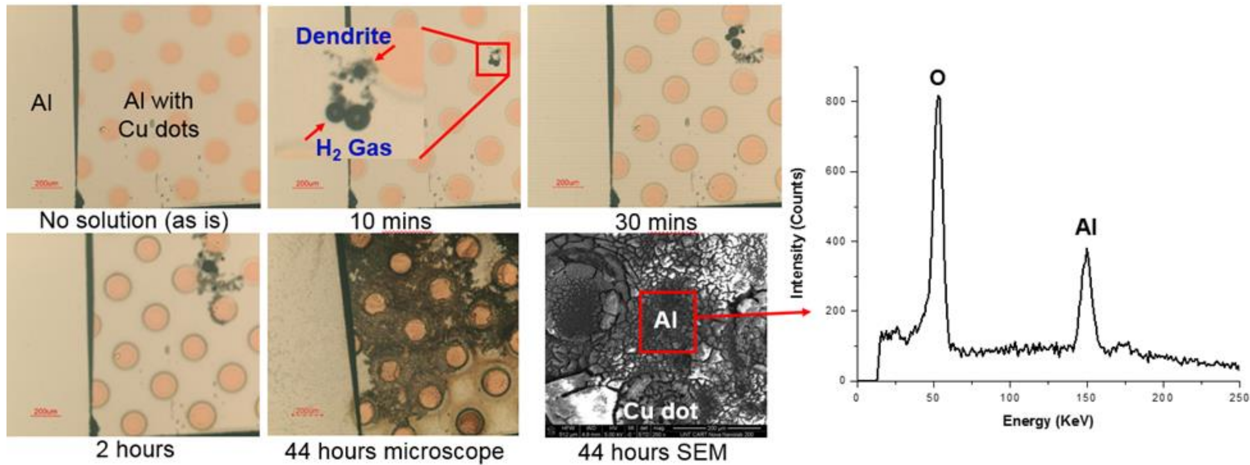

Figure 4.10: Corrosion progression comparison of 100 nm thick Cu microdot sputtered on 1.2 micron Al (0.5% Cu) versus only Al (0.5% Cu) placed into a 2ppm Cl^- solution at 5 pH using sulfuric acid.

The experiement in Figure 4.10 shows that hydrogen evolution is always present in an area of severe corrosion. Thus, an experiment focusing on hydrogen evolution was done. Figure 4.11 shows the focused study on the morphology of corrosion at the start of corrosion. The sample is 100nm Cu dot on a Al (0.5% Cu) substrate placed in a 1ppm Cl^- solution at 5pH. Once H_2 bubble evolution commenced for 30 seconds, the sample was taken out of solution for SEM and EDX analysis.

After the 30 seconds of hydrogen gas evolution, the Al/Cu interface area under SEM looked like an area of a volcano explosion with fragments around the explosion site, Figure 4.11 (A&B). This outburst is an effect of two causes: 1. As corrosion penetrates the top layer of aluminum oxide the pure Al underneath undergoes volume expansion due to oxidization. Cracking appears and becomes large due to aluminum increasing its size up to 5 times than its original volume when

oxidized.[29] 2. As aluminum oxidizes, hydrogen gas is generated, and the gas creates internal stress as the surface delaminates. Hydrogen gas leaving the system causes a self-catalyzing mechanism by not allow equilibrium to occur. Thus, this reaction is non-self-limiting and will spread to other areas of Al.

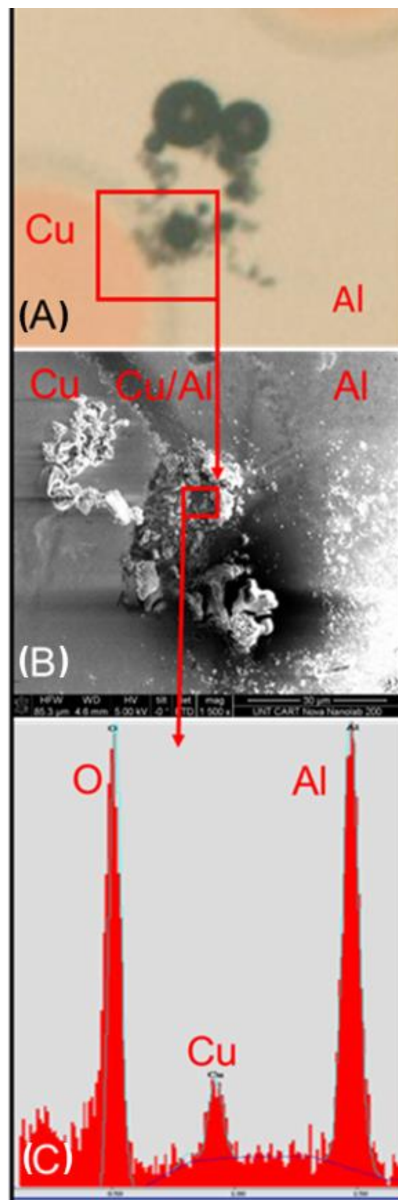

Figure 4.11: 30 second hydrogen evolution on Al/Cu interface area analyzation with; (A) Nikon microscope, (B) SEM and (C) EDX. Al/Cu sample was submerged in 1ppm Cl^- 5pH solution.

4.6 Cu-Wire Bonded Devices

At this point in the research project, three major aspects have been proven: Al mud crack has been reproduced, Cu/Al bimetallic interface increases corrosion rate, and hydrogen evolution is a critical part of the corrosion mechanism. Through experimentation and literature reading, a mechanism hypothesis has been formed. Testing the Al/Cu bimetallic corrosion mechanism against the Cu-wire bonded devices to verify the hypothesis is the next logical step.

More information on the Cu-wire device is shown in Figure 4.3 and section 4.2.2 Industry wire-bonded samples. The corrosion is very similar in the Cu-wire bonded to Al pad devices from industry collaborators when compared to the Cu dot sputtered on Al substrate samples made in house. First, the first sign of corrosion for both industry and in house samples is always on an Al surface with Cu nearby. Second, areas of severe corrosion have bubbles erupting from the Al surface and leaving the system, this was later found to be hydrogen evolution. Third, the times in which there is first sign of corrosion and 10% Cu wire bond separation from Al pad are similar to the times for Cu dot on Al surface first sign of corrosion and 10% total surface area corrosion.

In Figure 4.12 the Cu wire bonded to Al pad device is fully submerged in a 5ppm Cl^- 5pH solution and analyzed underneath a powerscope time lapse experiment. Figure 4.12 (A) shows the Cu wire bonded device before being submerged in the acidic chloride solution. The first sign of corrosion happened around the 10 min mark with darkening of the Al pad that is connected to a Cu wire. In Figure 4.12(B) there are several "bubbles" that can be seen as a sign of hydrogen evolution at around the 20-22 min mark. In Figure 4.12 (C), 10% of the Cu wires have been separated from the Al pad due to corrosion at the 4 hour and 12 min mark.

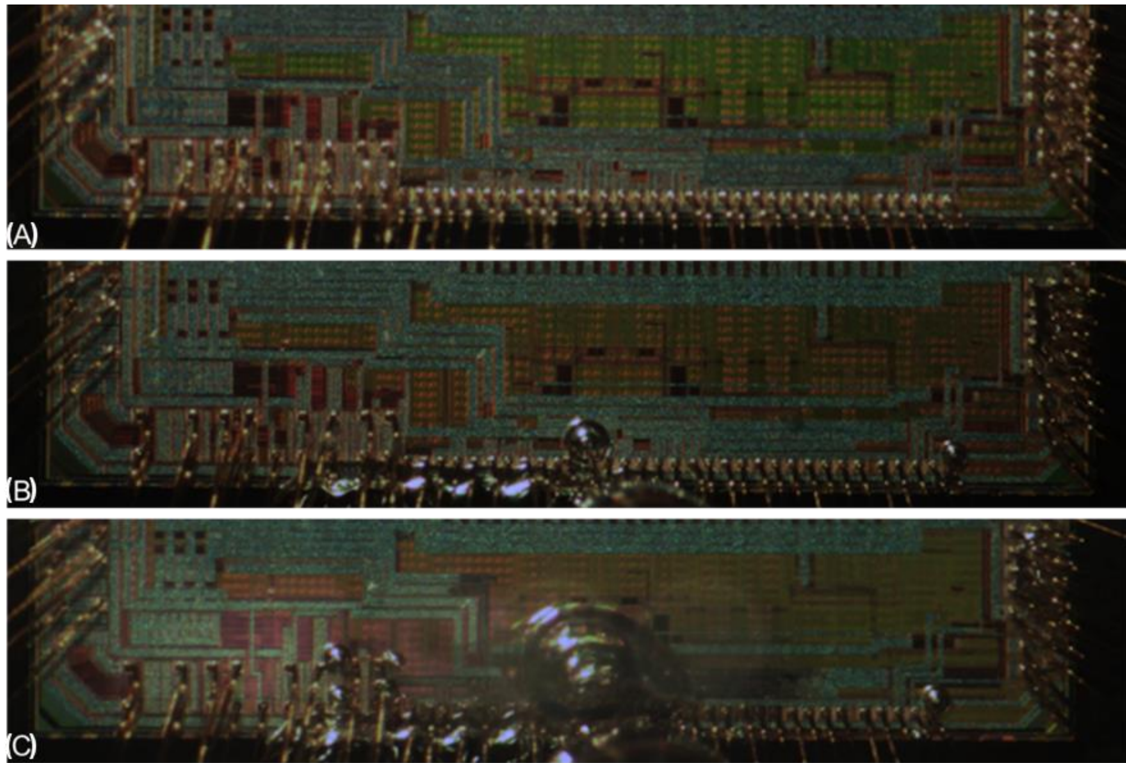

Figure 4.12: Cu-wire bonded on Al pad device submerged in 5ppm Cl- 5pH solution for (A) 0 mins, (B) 22 mins, (C) 4 hours 12 mins.

4.7 Pd Coated Cu-Wire Bonded Devices

The morphology and corrosion rate of Pd coated Cu wire bonded on Al pad (Pd/Cu-Al) samples in the acidic chloride solution is displayed in Figure 4.13 (A). In Figure 4.13 (A), within about 6 minutes of being submerged in 5ppm Cl^- 5pH solution, the first sign of corrosion can be seen on the Pd/Cu alloy wire Al pad sample. The first corrosion sight is on the Pd/Cu-Al interface where Pd/Cu alloy wire connects to the Al pad. Once corrosion started at the Pd/Cu wire Al pad interface, the evolution of hydrogen gas is present. The corrosion then spreads at a rate of 30 um per min along any connecting Al connection pathways of the chip. Within 7 minutes the first Pd/Cu ball disconnect from the Al pad. At the 43 minute mark more than 10% Pd/Cu ball is disconnects from Al pad. Despite a report that Pd coating shows promise of corrosion resistance, our result

shows palladium coated copper wire on Al pad (Pd/Cu-Al) have an increased corrosion rate.[16,21] Over 10% at copper wires are detached in 1hour in Pd/Cu-Al versus 12 hours for Cu-Al. This increase in corrosion rate could be to the high standard reduction potentials of Pd (E^o = +0.92 V) compared to Cu (E^o =+0.34 V). This creates a bigger potential gap vs Al (E^o = -1.66 V) which favors the flow of more electrons from Al to Pd, causing a faster oxidation (corrosion) rate of Al. In terms of morphological progression of corrosion, both Pd/Cu-Al and Cu-Al chips corrode similarly. In short, the only difference is corrosion rate.

Gas chromatography mass spectrometry (GC-MS) analysis in situ of Cu dot on Al and wire-bonded samples submerged in an acidic chloride solution was performed to determin if the bubble formation was indeed hydrogen evolution. Figure 4.14 (B) displays GC-MS analysis with sample vessels with Cu wire-bonded samples submerged in 5ppm Cl^- 5pH solution for over 40 hours versus an empty vial. Hydrogen gas was detected in a higher concentration within the vial with the Cu wire-bonded samples submerged in an acidic chloride solution for 40 hours versus a vial filled with only acidic chloride solution.

Figure 4.14 (A) shows an SEM image of a Pd/Cu wire device before being fully submerged in an acidic chloride solution. Figure 4.14 (B) shows an SEM image of a Pd/Cu wire device after being fully submerged in an acidic chloride solution for over 12 hours. The corroded Al pads are Al pads that once were connected to the Pd/Cu wire, thus providing the bimetallic interface. Once corrosion set in and the Pd/Cu wire to Al pad bond is broken, the corrosion spreads to any Al that is connected. One such connection is shown via SEM image in Figure 4.13 (B) by a red line.

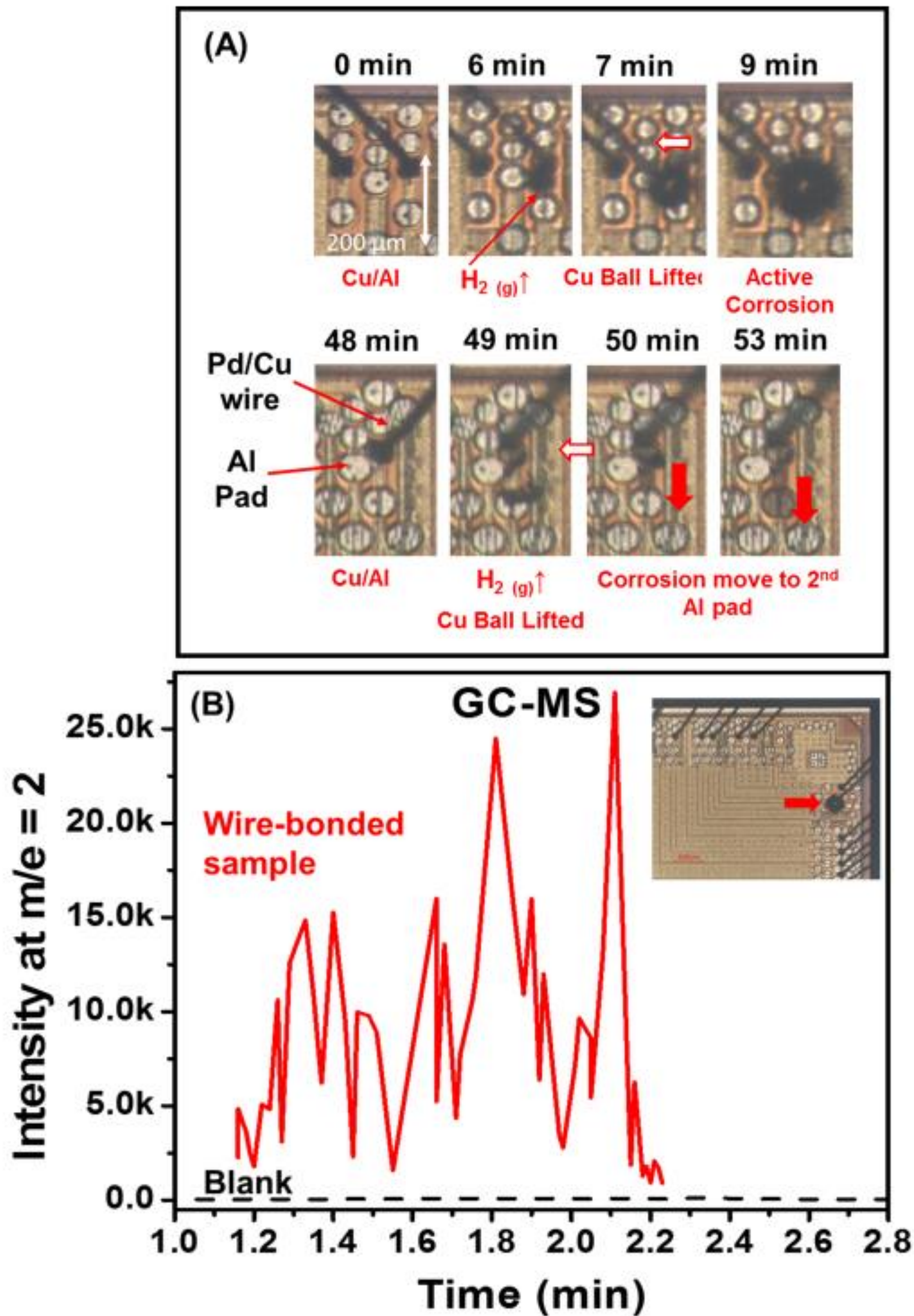

Figure 4.13: (A) Corrosion screening via microscopic time lapse experiment of a Pd-coated Cu wire bonded on Al pad sample fully submerged in a 5ppm Cl^- 5pH solution. (B) Gas Chromatography Mass Spectrometry (GC-MS) analysis in situ of a wire-bonded sample submerged in a 5ppm Cl^- solution at 5 pH for over 42 hours in a closed vial.

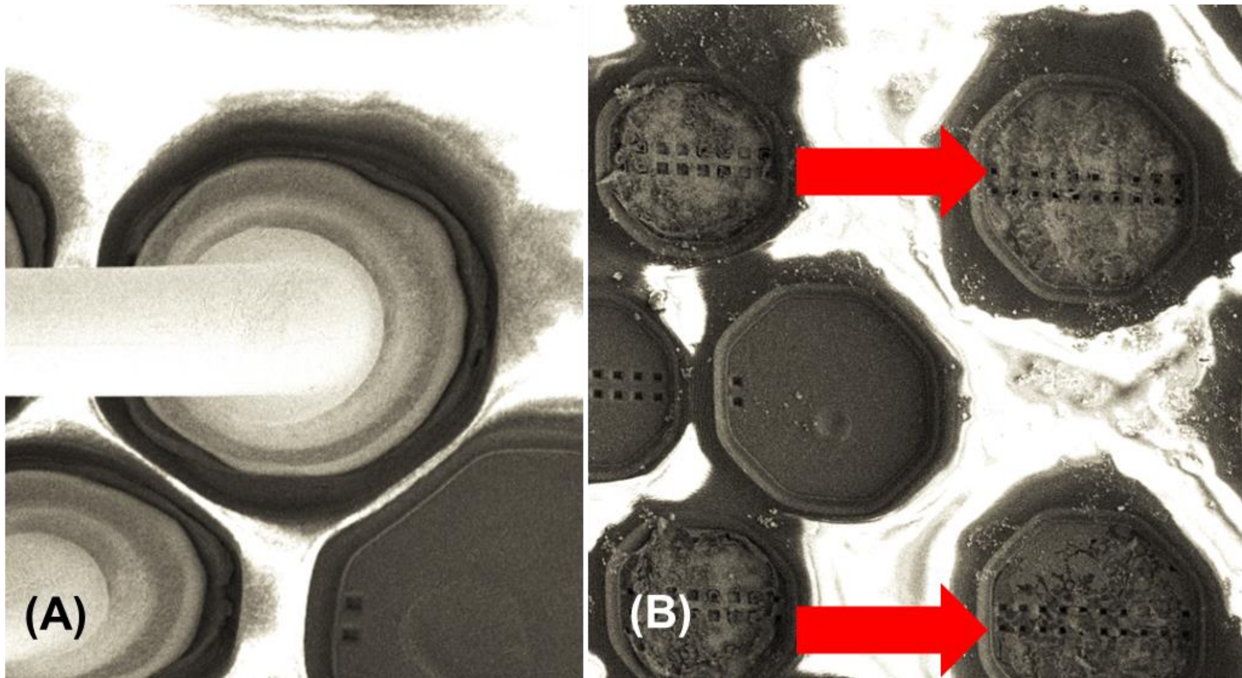

Figure 4.14: (A) As is Pd-coated Cu wire bonded on Al pad. (B) Pd-coated Cu wire bonded on Al pad Corrosion screening via microscopic time lapse experiment in in 5ppm Cl^- 5pH solution for 48 hours.

4.8 Bimetallic Interface versus Intermetallic Compound

Tomohiro Uno mentions that coating the Cu wire with Pd would reduce the corrosion rate.[16,30] Uno's reasoning is the Pd will serve as a diffusion barrier to retard the formation of a corrosive IMC phase. The Pd-coating is oxidation-free and has good bond ability and as well as adhesion to Cu wire.[31] Uno argues that Pd coating promotes a different Cu-Al IMC formation due to Pd being a part of the IMC. Uno also points at his previous work showing that Pd element in Au wire is effective for hindering a Br attack to Au.[32,33] However, the results at the experiment in Figure 4.15 show there is a Pd coated Cu wire bonded to Al pad device where corrosion rate has increased versus the Cu wire bonded device experiment in Figure 4.12.

To back up the claim that bimetallic interface is the starting place for corrosion and not Al/Cu IMC, as shown in Figures 4.10 and 4.11, our sample of 50 nm Cu dot were sputtered on Al

substrate with a PVD system with no additional heating. Thus, there is no Cu/Al IMC present in the samples used for corrosion screening in Figures 4.10 and 4.11 and yet there is severe Al mudcrack formation. Also in Figures 4.12 and 4.13 display two different wires bonded to Al devices will have less than 1 micron thick Cu/Al IMC. This Cu/Al IMC is covered by the Cu ball of the wire and the Cu/Al IMC is not open to the environment. Thus, moisture and Cl^- cannot interact with the Cu/Al IMC without first going through Al pad or Cu wire first. This makes the Al/Cu interface the logical starting place of corrosion in this acidic chloride environment.

4.9 Direct Current Measurements

The graphs in Figure 4.15 (A & B) show bare, pure aluminum and copper micropatterned aluminum electrodes versus platinum. A clear trend of increasing produced corrosion current is seen as chloride levels of the solution are increased. The copper micropatterned samples are also seen to produce significantly higher levels of current than the bare aluminum film. Figure 4.15 (C & D) shows the same studies as Figure 4.15 (A & B), but it substitutes an aluminum alloy (0.5% Cu/wt.) substrate commonly used by IC packaging industry. The same trends are observed, though less exaggerated than what was seen with pure aluminum samples. In addition, it is seen that the initial current are much lower than the pure aluminum samples, which shows that the copper doped aluminum electrodes are more resistant to corrosion than the pure aluminum samples.

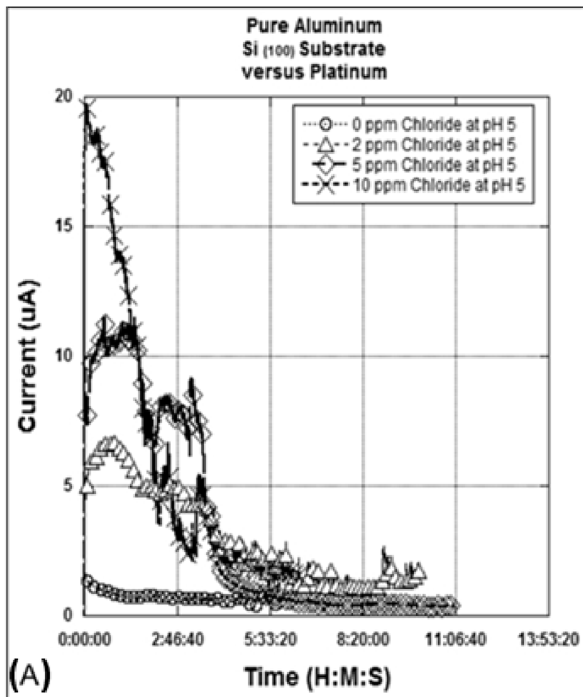

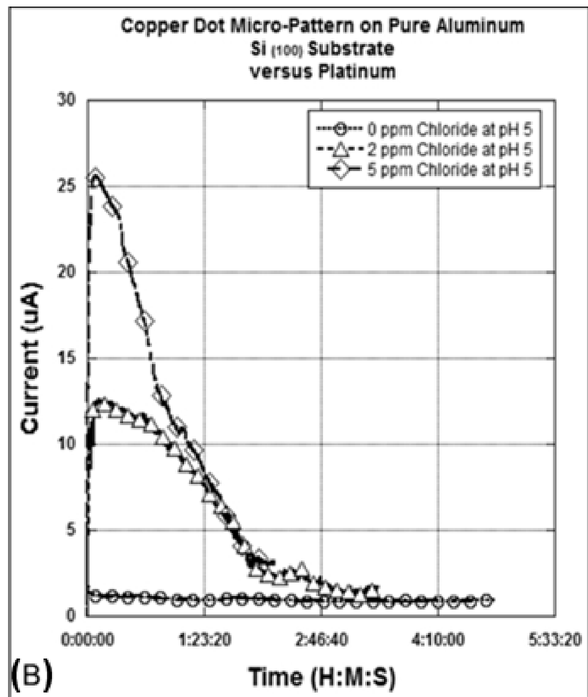

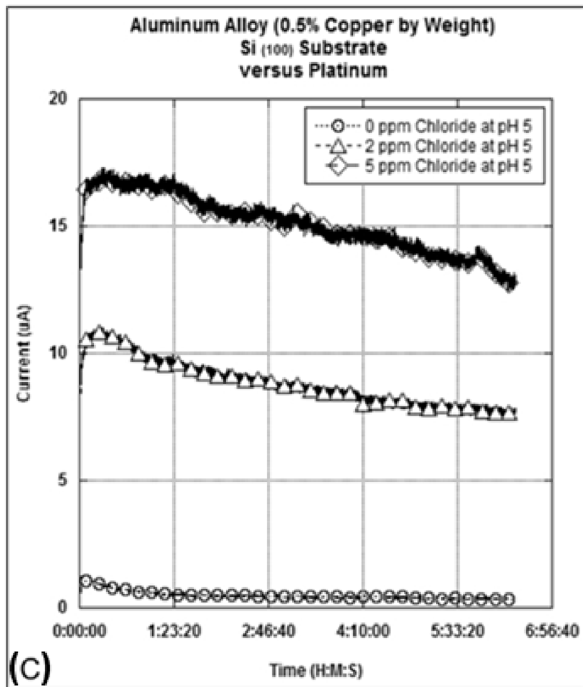

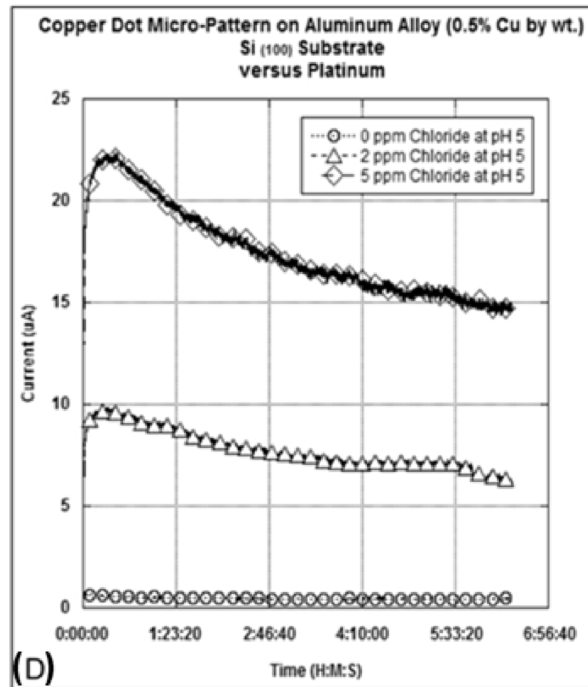

Figure 4.15: DC measurements with using platinum as the anode and (A) Al, (B) 50nm Cu dot on Al (C) Al (0.5% Cu by wt.) (D) Cu dot on Al (0.5% Cu by wt.) samples as the cathodes in varying concentrations of chloride solution, all at pH of 5.

4.10 Linear Sweep Voltammetry (LSV)

Table 4.3 displays E(V) and I (μA) values for Linear Sweep voltammogram (LSV) that is displayed in Figure 4.17.

Substrate	0 ppm Cl^-		5 ppm Cl^-	
	E (V)	I (μA)	E (V)	I (μA)
Al	**1.6**	**232**	**1.6**	**411**
Cu	**1.6**	- [illegible]**.966**	**1.6**	- [illegible]**.547**
Cu dot on Al	**1.6**	- [illegible]**.767**	**1.6**	- [illegible]**.942**

Table 4.3: Linear Sweep voltammograms (LSV) of Aluminum, Copper and Copper dot on Aluminum.

Release of hydrogen gas is observed on the Cu wire-bonded Al pads and on the bimetallic contact of micro-pattern corrosion screening. Electrochemically induced hydrogen evolution provides insight in deciphering the corrosion mechanism.

LSV is used to monitor the potential for hydrogen evolution on Al (0.5% Cu), Cu, and Cu dot on Al substrate in Figure 4.16 (A). LSV of Al in 0 ppm Cl^- shows the highest negative over-potential ($E_{over\text{-}potential}$) for H_2 evolution. This can be explained by the fact that the highly stable Al oxide helps protect the underneath Al from corrosion. However, the LSV of Al in 5 ppm Cl^- shifts the over-potential of H_2 evolution to a more positive potential. This shows that Cl^- ions weaken the Al oxide passivation film and reveal fresh Al underneath the oxide surface. Moreover, Cu dots/Al in 5 ppm Cl^- shifts $E_{over\text{-}potential}$ to much more positive than Al in 5 ppm Cl^-. Cu dots/Al in 5 ppm Cl^- shows the highest H_2 evolution current at -2.0 V (I = -428.1 $\mu A/cm^2$), followed by Al in 5 ppm Cl^- (I = -49.9 $\mu A/cm^2$) and Al in 0 ppm Cl^- (I = -7.2 $\mu A/cm^2$). This is in agreement with the

result obtained from the microscopic studies of micropattern corrosion screening discussed earlier. The increase in corrosion rate and hydrogen bubble formation is correlated with the shift of the hydrogen $E_{over\text{-}potential}$ to a more positive value.

Multiple LSV experiments on the same Al substrate in 5ppm Cl^- 5pH solution is displayed in Figure 4.16 (B). The onset potential for hydrogen evolution on Al (0.5% Cu) sample progressively decreased with multiple LSV experiments. Pre-activated Al accelerates the hydrogen evolution due to less protective oxide in subsequent LSV scans.

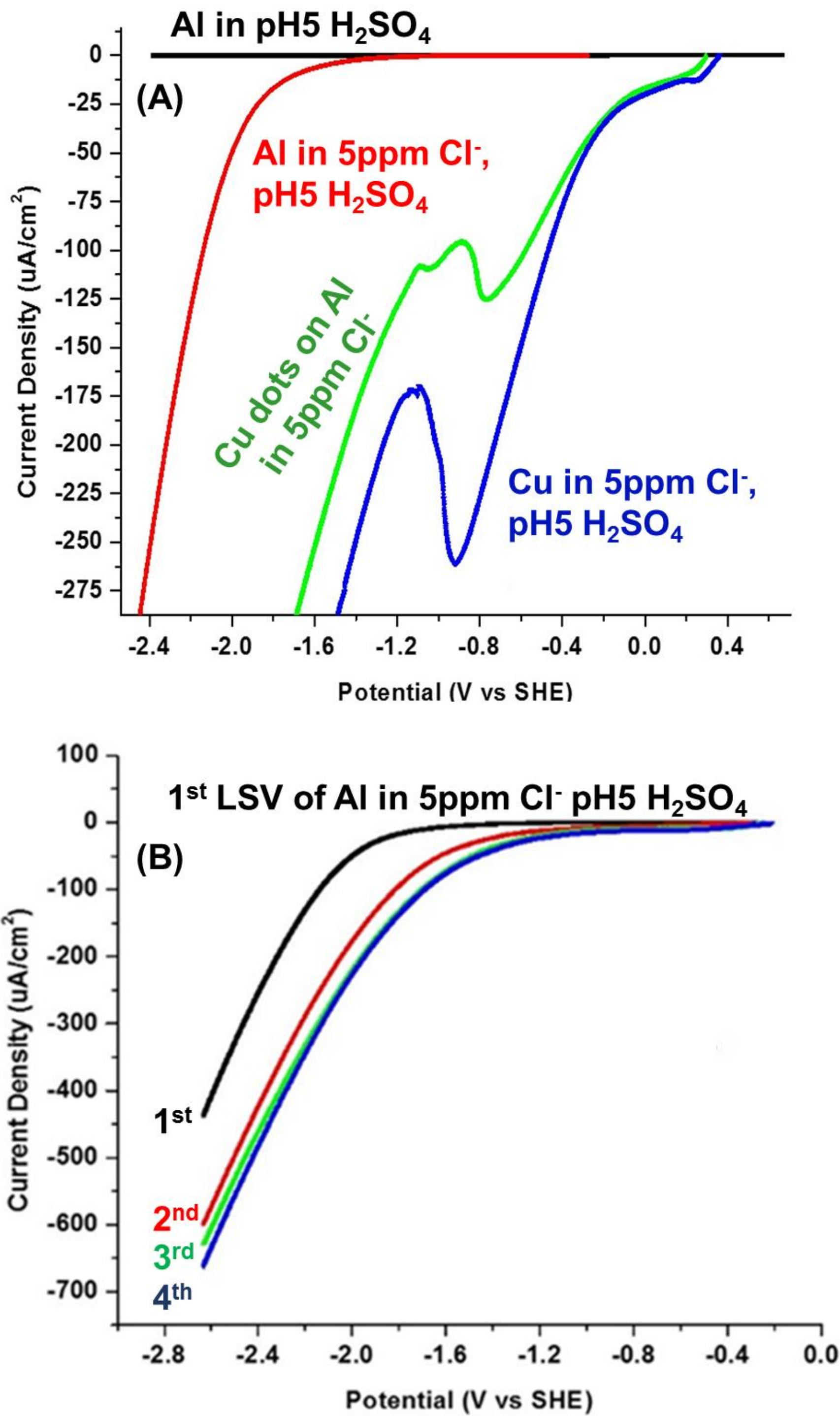

Figure 4.16: LSV with scan rate of 20 mV/s. Polarization curves were cathodic scanned from OCP and stop at potential where the cathodic current was significantly increased. Potential has been converted to SHE. (A) LSV scan of Al (0.5%Cu), 100nm Cu dot/Al (0.5%) and Cu in pH 5 H_2SO_4 solutions (B) Multiple LSV scan of Al (0.5%Cu).

4.11 Tafel Plot

Tafel plot of Al (0.5% Cu) substrate, 100nm Cu dot/Al (0.5% Cu), and 50 nm Cu/Si in a 5ppm Cl^- H_2SO_4 solutions (pH 5) is shown in Figure 4.17. The X-axis for Figure 4.17 is Log(I/A), (with I in μA and A in cm^2). The corrosion current (I_{corr}) and polarization resistance (Rp) can be estimated by crossing extrapolation of cathodic and anodic current curves of the Tafel plot. For example, in Figure 4.17, I_{corr} for Al (0.5% Cu) in 5ppm Cl^- 5pH is 1.78×10^{-9} A/cm^2.

The trend for corrosion potential (E_{corr}) is: $E_{Al,\ 5ppmCl}$ (-0.464V) < $E_{Cu\ dots/Al,\ 5ppmCl}$ (0.406V) < $E_{Cu,\ 5ppmCl}$ (0.414V). Cu dots/Al has a more negative corrosion potential than pure Cu. That suggests Cu dot/Al is more corrosive than Cu in 5ppm Cl^- 5pH. The trend for corrosion current (I_{corr}) is: $I_{Al,\ 5ppmCl}$ (4.72 nA/cm^2) < $I_{Cu,\ 5ppmCl}$ (7.75 nA/cm^2) < $I_{Cu\ dots/Al,\ 5ppmCl}$ (16.32 nA/cm^2). The higher corrosion current corresponds to faster corrosion rate, which in turn, has a higher H_2 evolution current. The 100nm Cu dot/Al (0.5% Cu) sample shows the least amount of corrosion resistance. This result corresponds well with immersion corrosion screening data, which shows H_2 evolution does play a key role in Al pad corrosion.

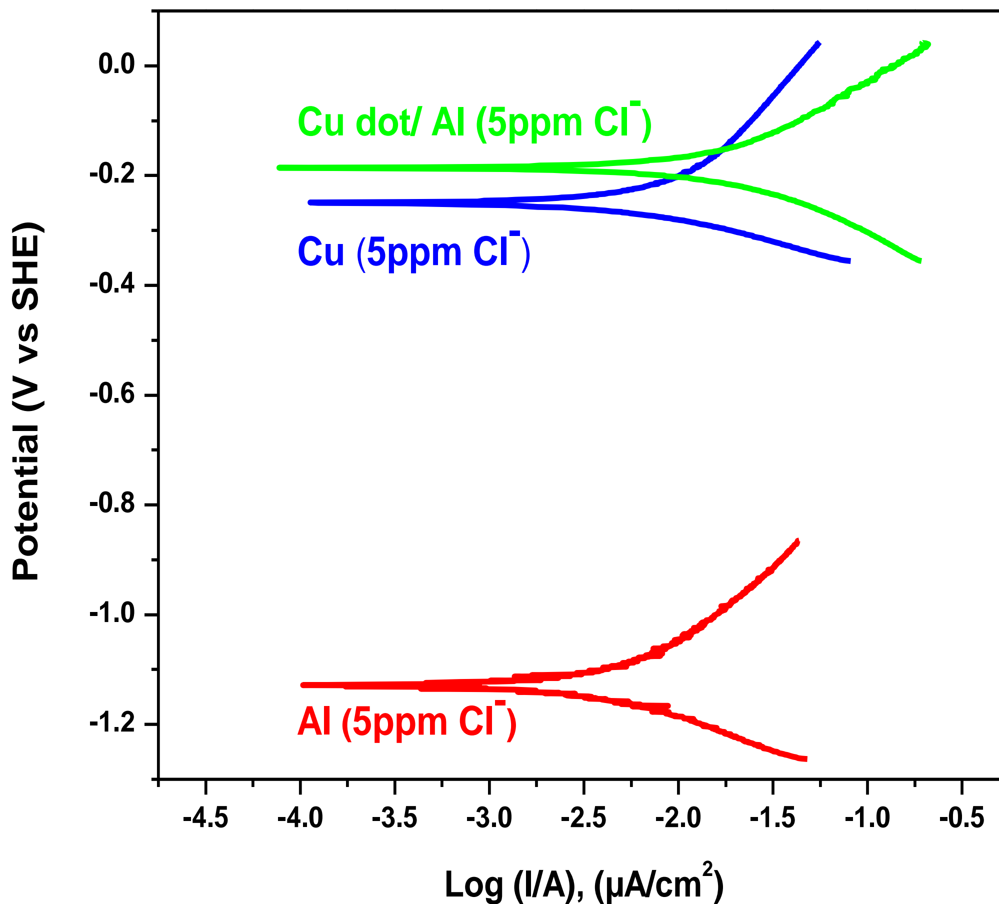

Figure 4.17: Tafel plot of Al (0.5% Cu), Cu dot/Al (0.5% Cu), and 50 nm Cu/Si in a 5ppm Cl^- 5pH solution.

4.12 Cu/Al Bimetallic Corrosion Mechanism

Galvanic/bimetallic corrosion is an electrochemical process, i.e. it relies on electron transfer. Corrosion of aluminum can be split into an anodic and cathodic part. A reaction can occur at separate places on the metal surface provided that they are in electrical contact. Electrochemical potential differences between aluminum and copper in the presence of an electrolyte causes current to flow from cathode (copper) to anode, leading to an oxidation of the anode (aluminum).

Mechanism of galvanic corrosion which occurs when dissimilar metals are connected in an electrolyte, such as chloride ion, has been previously reported.[7,8,19,34-36] Innuzzi *et.al* discussed mechanism of Au-Al bimetallic galvanic corrosion in chloride solution and identified Al as anode and Au acting as a cathode.[35] Al-Fe bimetallic has been also reported to remove carcinogen Cr(VI) with a high efficiency where aluminum acts as anode and iron as a cathode which leads to the reduction of Cr(VI) .[37] Electrochemical potential differences between aluminum and the nobler metal in the presence of chloride ion/electrolyte causes to flow at current from cathode (copper) to anode leading to an oxidation of the anode (aluminum). The importance of surface charge of the aluminum oxide in its interaction with an electrolyte, such as chloride ion has also been reported and is the center for the corrosion initiation.[7,34] Under acidic conditions, McCafferty et.al. reported that the surface charge of aluminum oxide is positive which leads to the attraction of negative ions such as Cl^-.[7,8,34] Goh and his group proposed corrosion reactions on bare Al bond pad in acidic chloride and stated the corrosion reaction exacerbates when Al is bonded to Au or Cu wire due to the additional galvanic corrosion.[19] Below is our proposed reaction mechanism happening at the anode and cathode of the Al-Cu galvanic/bimetallic corrosion in the presence of chloride ion.

Anodic reaction: Oxidation of aluminum metal

$$Al = Al^{3+} + 3e^-$$

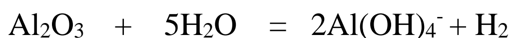

$$Al_2O_3 + 5H_2O = 2Al(OH)_4^- + H_2$$

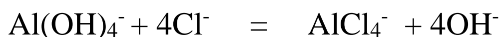

$$Al(OH)_4^- + 4Cl^- = AlCl_4^- + 4OH^-$$

Cathodic Reaction: Reduction through hydrogen gas evolution

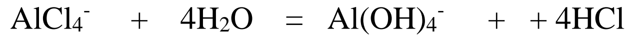

$$AlCl_4^- + 4H_2O = Al(OH)_4^- + + 4HCl$$

$$3H^+ + 3e^- = 3/2\ H_2$$

In Figure 4.18 there is a model of Cu/Al bimetallic corrosion. In aqueous solution, aluminum oxide reacts with water to form aluminum hydroxide. Chloride ion then replaces the hydroxide to make aluminum chloride which leads to a dissolution of the passivating oxide because aluminum chloride has very high solubility in water (46g/ 100mL).[11,18] Hydrolysis of aluminum chloride generates protons that eventually produce hydrogen gas. This is the first time hydrogen gas evolution was observed as the key reaction to accompany the active Al corrosion progression. This hydrogen evolution can cause physical stress on the surface and cause a "volcano explosion" like damage shown in Figure 4.11. The H_2 gas leaves the system, which prevents the reaction from reaching equilibrium. Thus, the reaction is not self-limiting. Another byproduct of $AlCl_4^-$ hydrolysis reaction is an increase in local acidity.[38,39] This increase in acidity will attract the negatively charged Cl^- ions, which will increase the corrosion rate in that area. As the corrosion penetrates the Al surface by Cl^- weakening the top $Al(OH)_4^-$ layer, the Al underneath is converted to $Al(OH)_4^-$ by the oxygen and moisture in the system.[38,39] The reaction of Al undergoing oxidization is increased by the reaction barrier being decreased by electrochemical cell formed between Cu and Al interface. The Al is giving up its electrons to Cu, and the Al is being oxidize in the redox reaction process. This volume expansion from Al to $Al(OH)_4^-$ is what causes the cracks both vertically and horizontally, allowing easier excess to Cl^- and moisture to pristine Al.[29] The pitting or surface roughness is the Cl^- ions attacking the $Al(OH)_4^-$. The dendrite formation is the cracking starting to form due to the Cl^- weakening the top $Al(OH)_4^-$, and the corrosion is starting to penetrate the Al film. Mature mud crack is due to this corrosive penetration effect that is deep

enough to cause a large set of cracks and is easily detectable by 50x magnification microscope. The Cu/Al bimetallic corrosion is thermodynamically favorable due to the energy of the system, aka the standard reduction potential difference between Cu and Al. This reaction is enthalpy negative due to exothermic process, and is entropy positive due to solid film turning into debris and hydrogen leaving the system.

Key driving forces for the dissolution of the passivating layer of Al_2O_3 are as follows; 1. weakening of aluminum oxide by Cl^-, 2. the strong solubility of aluminum chloride, and 3. generation of hydrogen gas.

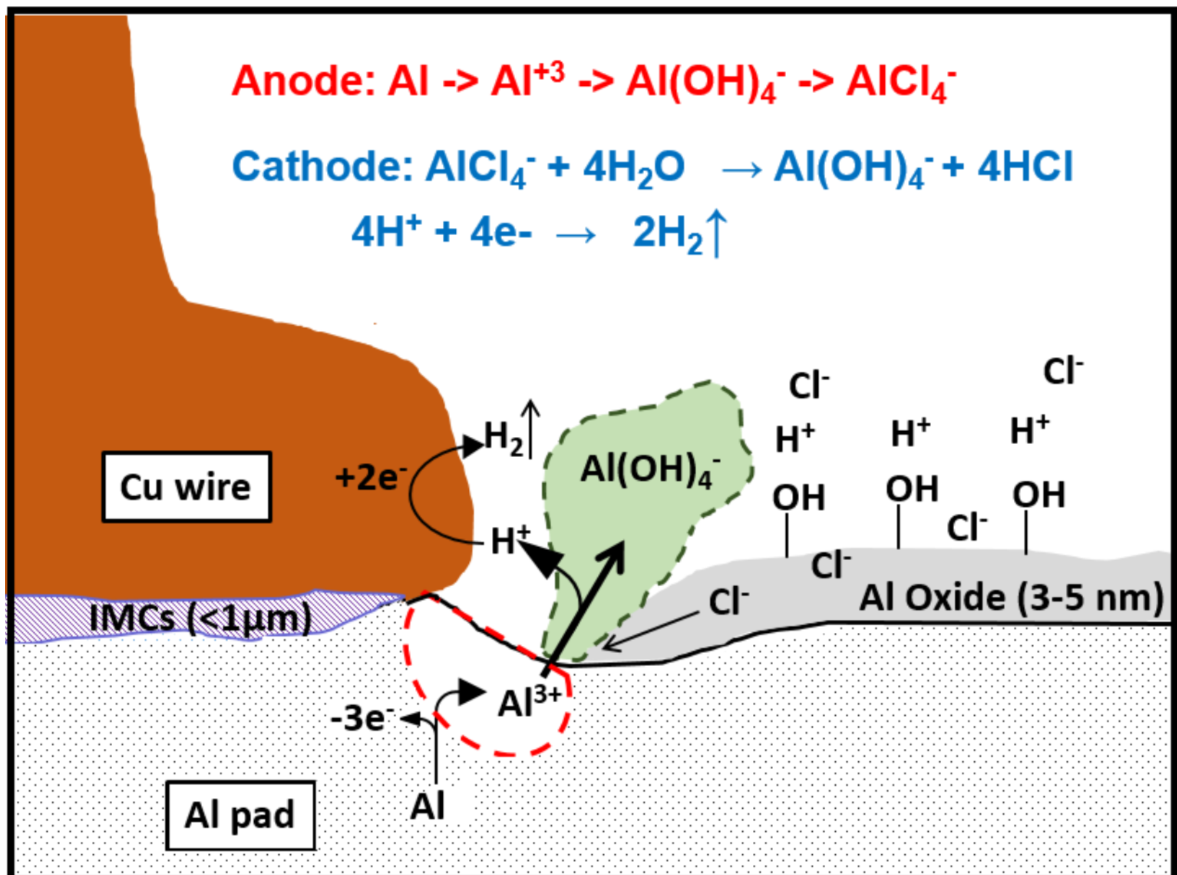

Figure 4.18: Proposed bimetallic corrosion mechanism of Al pad with Cu ball attachment.

4.13 Cu/Al Bimetallic Corrosion Inhibition

The two key points in the mechanism proposed in Figure 4.18 is the hydrogen evolution and the transfer of electrons from Al to Cu via redox reaction. A nitrogen heterocycle that connects with Cu via a -N, -O, -S covalent bond has been proposed to inhibit Ru/Cu bimetallic corrosion, shown in Figure 4.19.[40] An effective corrosion inhibitor, should covalently anchor via -N, -O, -S on Cu/Al surface and also establish strong adhesion by π-π or H-bonding with mold compounds. Such inhibitors where studied via immersion screening.

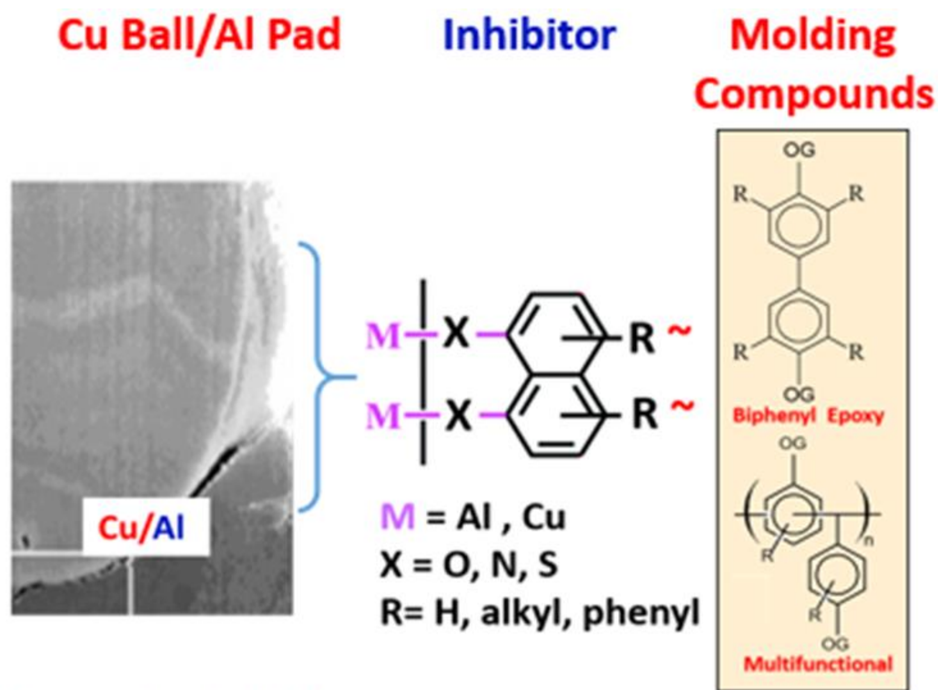

Figure 4.19: Proposed inhibition of bimetallic corrosion of Al pad with Cu ball attachment.

Several inhibitors were screened via immersion screening via Nikon microscope. The inhibitors are dissolved 0.1% into the acidic chloride solutions. One such inhibitor worked well in the Cu/Al bimetallic interface in acidic chloride environment. Benzotrizole (BTA) connects to Cu via a nitrogen covalent bond in an acidic environment. Whereas pyrazole works well in binding to

Cu in basic solutions, BTA binds well to Cu in acidic environments.[40] For example, a Pd/Cu-Al as is Figure 4.20 (A) is 100% corroded within 17 hours in a 5ppm Cl^- 5pH solution, which is shown in Figure 4.20 (B). When the solution has BTA added 0.1% by weight, the Pd/Cu-Al sample still looks like the as is sample when it is submerged in a 5ppm Cl- 5pH 0.1% by weight of BTA solution for 12 days shown in Figure 4.20 (C). Figure 4.20 (C) shows that BTA has greatly inhibited the corrosion due to the fact that 97% of Al pads are not showing any signs of corrosions. This is due to the covalently bonded inhibitor to the Cu and Al metal greatly raises over-potential barrier of H^+/H_2 cathodic reaction to passivate the overall Al corrosion.

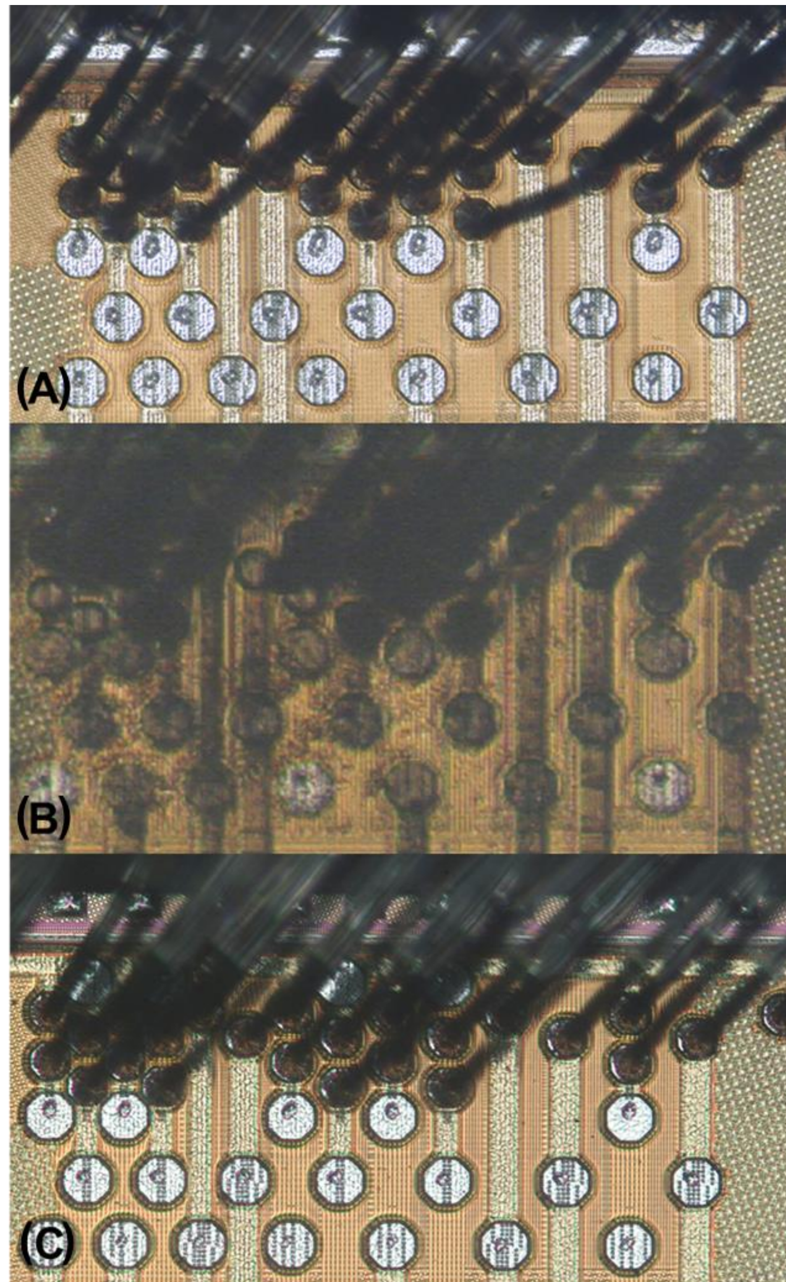

Figure 4.20: Pd coated on a Cu wire which is bonded with an Al pad. (A) as is. (B) in a 5ppm Cl- 5pH solution for 17 hours. (C) 5ppm Cl- 5pH 0.1% by weight of BTA solution for 12 days.

LSV experiments show that BTA inhibits corrosion by increasing the amount of voltage applied before a current change is detected, Figure 4.21. This inhibition is present in both the Al (0.5% wt. Cu) substrate in Figure 4.21 (A) and 50nm thick Cu dot sputtered on Al (0.5% wt. Cu)

substrate via PVD. BTA binds to both Al and Cu to make the electron transfer between Al to Cu and hydrogen evolution more difficult.

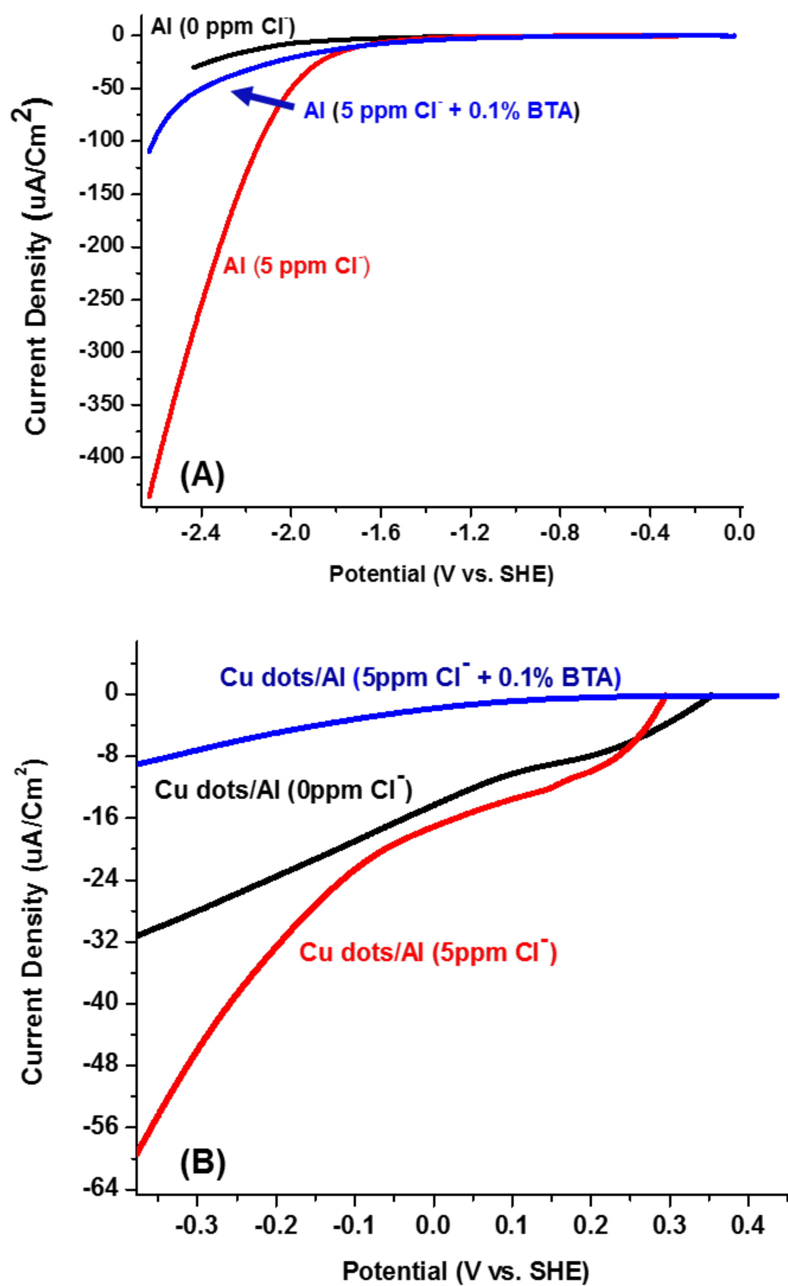

Figure 4.21: LSV with scan rate of 20 mV/s. Polarization curves were cathodic scanned from OCP and stop at potential where the cathodic current was significantly increased. Potential has been converted to SHE. (A) LSV scan of Al (0.5%Cu) (B) LSV scan of 50nm Cu dot/Al (0.5%).

4.14 Au Wire Bonded Devices

Au wire bonded to Al pad devices (Au-Al) tested in the same acidic chloride environments as the Cu-Al and Pd/Cu-Al samples due to Au's well known anti-corrosion properties.[5,16,32,33] First signs of corrosion with an Al pad darkening and bubble formation on the Au-Al sample at the 6 to 7 days mark fully submerged in a 5ppm Cl^- 5pH solution is displayed in Figure 4.22 (B). At the 7 to 8 day mark, 10% of the Al pads have signs of corrosion; however, there is no wire detachment. The first wire detachment did not happen until 41 days submerged in the acidic chloride solution, and then an average of 1 Au wire bond lift off per day. To put this in perspective, it took the Cu-Al sample 2 hours for the first Cu wire to disconnect from the Al pad when submerged in the 5ppm Cl^- 5pH solution. The Al (0.5% wt. Cu) substrate displayed in Figure 4.5 is more than 10% corroded at the 12 hour mark when submerged in the same acidic chloride solution. This brings Cu into suspect that Cu is not an innocent bystander in the corrosion mechanism.

Inhibitor BTA was added by 0.1% weight to the 5ppm Cl^- 5pH solution and was used to submerge an Au-Al sample. The first sign of corrosion was not detected until the 44 day mark. BTA is known to bind to Cu; however, I suspect that BTA will bind to other metals such as Al.[40] Since the corrosion was inhibited by BTA when no Cu is present, there is reasonable proof that BTA also binds to Al.

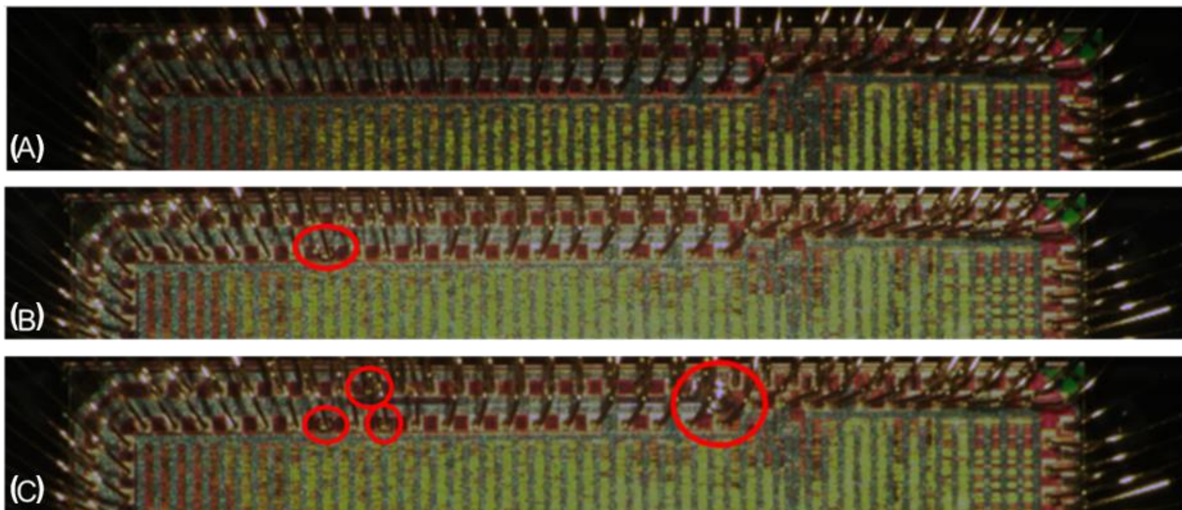

Figure 4.23: Au wire bond to Al pad device (A) as is (B) 6 days 8 hours submerged in 5ppm Cl- 5pH solution (C) 8 days 1 hour in 5ppm Cl- 5pH solution.

4.15 Effect of Fluoride

The effect of fluoride on the same sample sets was studied. Figure 4.23 (A) displays Al (0.5% wt. Cu) submerged in a 5 ppm F^- 4pH solution for 48 hours and Figure 4.23 (C) 50 nm Cu dot on Al (0.5% wt. Cu) submerged in a 5 ppm F^- 5pH solution for 3 days. The type of corrosion displayed by fluoride is significantly different than the corrosion caused by Cl^- shown in Figure 4.23 (B and D). The corrosion caused by fluoride is less aggressive than corrosion caused by chloride. The fluoride corrosion takes a longer amount of time to cause a visible change. Fluoride causes a color change on the Al whereas chloride corrosion causes dendrite formation by penetrating the Al oxide surface. The fluoride corrosion etches the Cu dots whereas corrosion by chloride contamination focuses at Al surface first. When EDX was performed on the Al surface of samples in Figure 4.23 (C and D) the sample submersed in fluoride solution (C) had an aluminum to oxygen ratio of 12:1 whereas (D) had an Al:O ratio of 0.39:1. Thus, the fluoride corrosion does not penetrate like the corrosion caused by chloride.

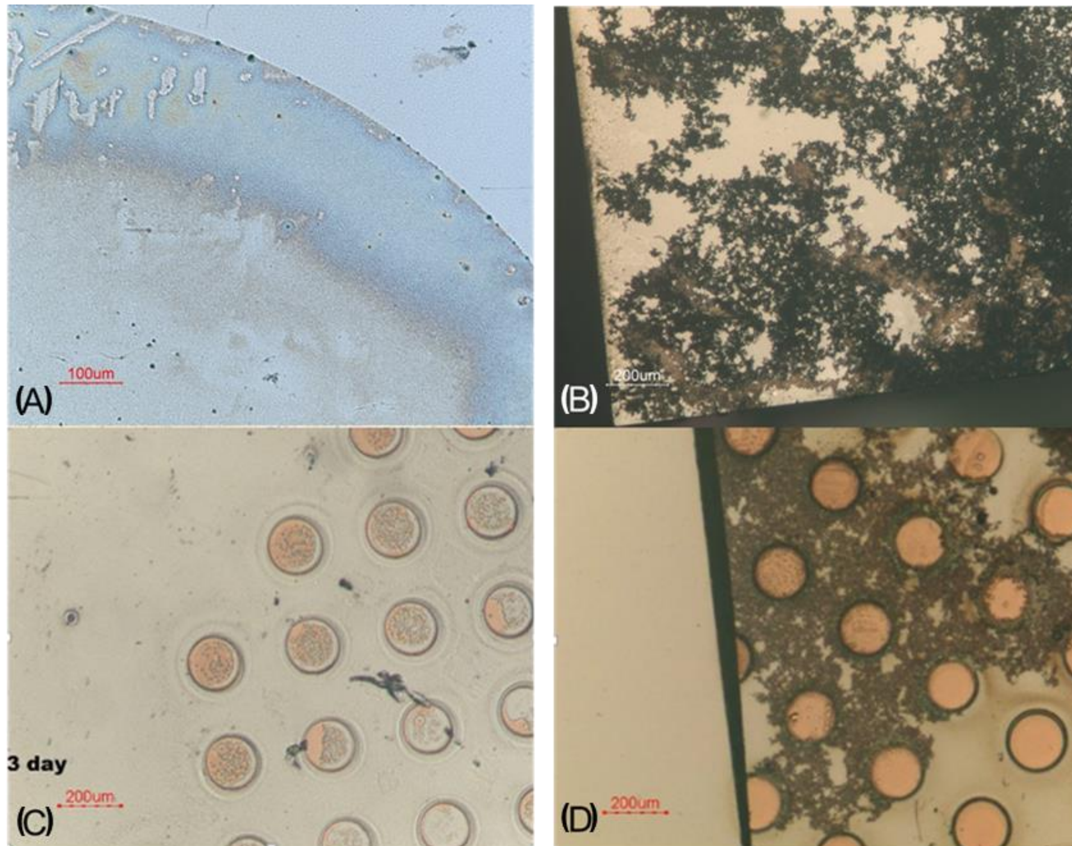

Figure 4.24: (A): Al (0.5% Cu by wt) submerged in a 5 ppm F^- 4pH solution for 48 hours. (B) Al (0.5% Cu by wt) submerged in a 5 ppm Cl^- 4pH solution for 48 hours. (C) 50 nm Cu dot on Al (0.5% Cu by wt) submerged in a 5 ppm F^- 5pH solution for 3 days. (D) 50 nm Cu dot on Al (0.5% Cu by wt) submerged in a 2 ppm Cl^- 5pH solution for 36 hours.

4.16 Conclusion

The corrosion progression morphology of Al alloy under acidic conditions in the presence of chloride is as follows: corrosion starts as surface roughness which then turns into a dendrite corrosion, then, later continues to grow into a mud-crack type corrosion as corrosion penetrates deeper into the Al substrate. SEM analysis of dendrite corrosion on Al (0.5%Cu) shows that early dendrite occurs mostly at the grain boundary. This could possibly be due to defects and/or Cu content at the grain boundary.

Cu micro-pattern screening revealed: corrosion is activated on the Al/Cu interface area, the corrosion rate is higher compared to bare Al, and hydrogen gas evolution. Mechanistic insight of Cu ball bond on Al pad corrosion is explored and found hydrogen evolution has a significant part in Cu/Al bimetallic corrosion mechanism.

Cu dot on Al pad simulated similar corrosion rates as Cu and Pd wire bonded to Al chip samples at a much lower cost. When Cu dots are added to an Al (0.5% Cu) substrate, the hydrogen evolution and corrosion rate increases. Changing the Cu wire to Au for the wire bonded samples and adding benzotrizole to the solution both displayed corrosion inhibition properties. Corrosion caused by fluoride contamination was less destructive than corrosion caused by chloride contamination. Future studies including F^-, Br^-, inhibitor screening, Au, and other metals have been or will be conducted in the Professor Oliver Chyan group by Muthappan Asokan and Alex Lambert.

4.17 References

1. Licata, T. J.; Colgan, E. G.; Harper, J. M. E.; Luce, S. E. Interconnect fabrication processes and the development of low-cost wiring for CMOS products. *IBM Journal of Research and Development* **1995**, *39*, 419-435.

2. Spencer, T.; Osborn, T.; Kohl, P. Materials science. High-frequency chip connections. *Science* **2008**, *320*, 756.

3. Osborn, T.; Gailba, N.; Kohl, P. A. Electroless Copper Deposition with PEG Suppression for All-Copper Flip-Chip Connections. *Journal of the Electrochemical Society* **2009**, *156*, D226-D230.

4. Kim, H.; Lee, J.; Koh, K.; Won, J.; Chpe, S.; Lee, J.; Moon, J.; Park, Y. Effects of Cu/Al Intermetallics Compound (IMC) on Copper Wire and Aluminum Pad Bondability. *IEEE Trans. Comp and Pack. Tech* **2003**, *26*, 367-374-2.

5. Trethewey, K. R.; Chamberlain, J. *Corrosion For Students of Science and Engineering;* John Wiley & Sons: New York, NY 10158, 1988; , pp 382.

6. Ambat, R.; Jensen, S. G.; Møller, P. Corrosion Reliability of Electronic Systems. *ECS Transactions* **2008**, *6*, 17-28.

7. McCafferty, E. *Surface Chemistry of Aqueous Corrosion Processes;* Springer Cham: Heidelberg, New York, 2015; , pp 96.

8. Natishan, P. M.; O'Grady, W. E. Chloride Ion Interactions with Oxide-Covered Aluminum Leading to Pitting Corrosion: A Review. *Journal of The Electrochemical Society* **2014**, *161*, C421-C432.

9. Zhao, W. G.; Wang, J. G.; Zhao, H. L.; Hou, J. Q.; Jiang, Q. C. Corrosion mechanism of the modified casting Al–Cu alloy by the nano-scale PrxOy. *J. Alloys Compounds* **2009**, *479*, L30-L35.

10. Kolics, A.; Besing, A. S.; Baradlai, P.; Haasch, R.; Wieckowski, A. Effect of pH on Thickness and Ion Content of the Oxide Film on Aluminum in NaCl Media. *Journal of The Electrochemical Society* **2001**, *148*, B251-B259.

11. Mol, J.; Hinton, B.; Weijde, D.; Wit, J.; Zwaag, S. A filiform corrosion and potentiodynamic polarisation study of some aluminium alloys. *J. Mater. Sci.* **2000**, *35*, 1629.

12. Moghaddam, M.; Pravizi, R.; Davoodi, A.; Sabzevear, M.; Imani, A. Establishing a Correlation Between Interfecial Microstructures and Corrosion Initiation Sites in Al/Cu Joints by SEM-EDS and AFM-SKPFM. *Corr. Sci.* **2014**, *79*, 148-158.

13. Xue, P.; Xiao, B.; Ni, D.; Ma, Z. Enhanced Mechanical Properties of Friction Stir Welded Dissimilar Al-Cu Joint by Intermetallic Compounds. *Mat. Sci. Eng.* **2010**, *527*, 5723-5727.

14. Galvao, I.; Oliverira, J.; Loureiro, A.; Rodrigues, D. Formation of Distribution of Brittle Structures in Fiction Stir Welding of Aluminum and Copper: Influence of Shoulder Geometry. *Intermetallics* **2012**, *22*, 122-128.

15. Saeid, T.; Zadeh, A.; Sazgari, B. Weldability and Mechanical Properties of Dissimilar Aluminum-Copper Lap Joints Made by Friction Stir Welding. *J. Alloys compd.* **2010**, *490*, 652-655.

16. Uno, T. Bond reliability under humid environment for coated copper wire and bare copper wire. *Microelectronics Reliability* **2011**, *51*, 148-156.

17. Yu, C. F.; Chan, C. M.; Chan, L. C.; Hsieh, K. C. *Microelectronic Reliability* **2011**, *51*, 119-124.

18. Wang, B.; Tang, L.; Qi, J.; Wang, J. Effects of Pulse Electromagnetic Field on Corrosion Resistance of Al-5 % Cu Alloy. *J. Low Temp. Phys.* **2013**, *170*, 418-423.

19. Goh, C. S.; Chong, W. L. E.; Lee, T. K.; Breach, C. Corrosion Study and Intermetallics Formation in Gold and Copper Wire Bonding in Microelectronics Packaging. *Crystals* **2013**, *3*, 391-404.

20. Yu, K. K.; Pillai, K. S.; Nalla, P. R.; Chyan, O. Study of bimetallic corrosion related to Cu interconnects using micropattern corrosion screening method and Tafel plots. *J. Appl. Electrochem.* **2010**, *40*, 143-149.

21. Ross, N.; Goswami, A.; Berhe, S.; Lin, P.; Chyan, O. Study of Bimetallic Corrosion and Its Inhibition Strategy for Cu Interconnect and IC Packaging Using Micro-Pattern Corrosion Screening. *SRC Techcon* **2015**.

22. Lienig, J. Introduction to Electromigration-Aware Physical Design. *ISPD* **2006**, 39-46.

23. Boer, J. H.; Verwey, H. Advances in Colloid Science. In *Advances in Colloid Science*; Mark, E. J. W., Ed.; Interscience Publishers: 1950; Vol. 3, pp Chapter 1, p. 1.

24. Kosmulski, M. Standard enthalpies of ion adsorption onto oxides from aqueous solution and mixed solvents. *Colloids Surf.* **1994**, *A 83*, 237.

25. Larsen, M. H.; Walmsley, J. C.; Lunder, O.; Mathiesen, R. s.; Nisancioglu, K. Intergranular Corrosion of Copper-Containing AA6xxx AlMgSi Aluminum Alloys. *J. Elect. Chem. Soc.* **2008**, *155*, C550-C556-11.

26. Metzger, M. Intergranular Corrosion of Single Phase Aluminium as a Pitting Phenomenon. *Journal De Physique* **1975**, *36*, 387.

27. Zeng, Y.; Bai, K.; Jin, H. Thermodynamic study on the corrosion mechanism of copper wire bonding. *Microelectronics Reliability* **2013**, *53*, 985-1001.

28. Alpem, P.; Lee, K. C. Moisture-Induced Delamination in Plastic Encapsulated Microelectronic Devices: a Physics of Failure Approach. *IEEE Trans Dev Mater Reliab* **2008**, *8*, 478-483.

29. Vrublevsky, I.; Parkoun, V.; Sokol, V.; Schreckenbach, J.; Marx, G. The study of the volume expansion of aluminum during porous oxide formation at galvanostatic regime. *Appl. Surf. Sci.* **2004**, *222*, 215-225.

30. Chong, G.; Uda, H. Comparative Reliability Studies and Analysis of Au, Pd-Coated Cu and Pd-Doped Cu Wire in Microelectronics Packaging. *PLoS ONE* **2014**, *9*, 1.

31. Uno, T.; Terashima, S.; Yamada, T. Surface-Enhanced Copper Bonding Wire for LSI. *ECTC* **2009**, *59*, 1486-1495.

32. Uno, T.; Tatsumi, K. Thermal Reliablility in Gold-Aluminum Bonds Encapsulated in Bi-Phenyl Epoxy Resin. *Microelectronics Reliability* **2000**, *40*, 145-153.

33. Uno, T.; Kimura, K.; Tatsumi, K. Thermal Bond Reliability of High Reliability Gold Alloy Wires for Automotive ICs. *International Society for Hybrid Microelectronics* **2005**, 557-563.

34. McCafferty, E. *E. Corr. Sci.* **2003***, 45*, 1421-1432.

35. Iannuzzi, M. *IEEE Trans. Comp. Hybrids and Manuf. Tech.* **1983***, 6*, 191-201.

36. Wang, B.; Zhang, L.; Su, Y.; Mou, X.; Liu, J. Investigation on the corrosion behavior of aluminum alloys 3A21 and 7A09 in chloride aqueous solution. *Mat. and Design* **2013***, 50*, 15-21.

37. Tang, B.; Dionysiou, D. D.; Cheng, Z.; Fu, F. Fe/Al bimetallic particles for the fast and highly efficient removal of Cr(VI) over a wide pH range: Performance and mechanism. *J. Hazard. Mat* **2015***, 298*, 261-269.

38. Iannuzzi, M. Bias Humidity Performance and Failure Mechanisms of Non-Hermetic Aluminum SIC's in an Environment Contaminated with Cl2. *IEEE* **1982***, 82*, 16-26.

39. Ueng, H. Y.; Liu, C. Y. The Aluminum Bond-Pad Corrosion in Small Outline Packaged Devices. *Materials Chemistry and Physics* **1997***, 48*, 27-35.

40. Goswami, A.; Koskey, S.; Mukherjee, T.; Chyan, O. Study of Pyrazole as Copper Corrosion Inhibitor in Alkaline Post Chemical Mechanical Polishing Cleaning Solution. *ECS Journal of Solid State Science and Technology* **2014***, 3*, P293-P297.

CHAPTER 5

SUMMARY AND PROPOSED FUTURE STUDIES

5.1 Summary of New Research Findings

5.1.1 MIR-IR Characterization of Amorphous Silicon

In the study discussed in chapters 2 and 3, we employed multiple internal reflection infrared spectroscopy (MIR-IR) to characterize chemical bonding structures of boron doped hydrogenated amorphous silicon (*a*-Si:H(B)). This technique has been shown to provide over a hundred fold increase of detection sensitivity when compared with conventional FTIR.[1,2] In chapter 2 MIR-IR analyses reveal an interesting counter-balance relationship between boron-doping and hydrogen-dilution growth parameters in PECVD-grown *a*-Si:H.[1] Specifically, an increase in the hydrogen dilution ratio (H_2/SiH_4) was found to cause the increase in the Si-H bonding and a decrease in the B-H and SiH_2 bonding, as shown by the changes in corresponding IR absorption peaks. In addition, although a higher boron dopant gas concentration was seen to increase the BH and SiH_2 bonding, it also resulted in the decrease of the most stable SiH bonding configuration. The new chemical bonding information of *a*-Si:H thin film was correlated with the various boron doping mechanisms proposed by theoretical calculations to help explain the low doping efficiency of *a*-Si:H films. We propose that the threefold coordination of B (2,1) (a B with two Si and one H neighbors) contributes to the inactive B-doping in PECVD grown *a*-Si:H thin films based on MIR-IR characterization.[1]

In chapter 3, substrate temperature, hydrogen dilution and boron concentration are the variables being focused via MIR-IR and confirmed from collaborators via Raman spectroscopy.[3] The goal for solar cell and sensor industry is to have *a*-Si:H(B) film as organized as possible

without any microcrystals forming. This film type is called protocrystalline-Si:H.[4] MIR-IR and Raman analysis brings chemical bonding information to this area to direct the development of *a*-Si:H(B) for solar cell and sensor applications. Results have found that decreasing either hydrogen dilution or substrate temperature decreased organization of the silicon lattice in the amorphous films. This is shown by a significant increase in intensity of the peaks associated with *a*-$Si:H_2$ via MIR-IR analysis and the increased intensity ratio (I_{TA}/I_{TO}) in Raman analysis.[3] Raman collaboration with MIR-IR shows that films with low SRO and MRO in Raman have a high $[Si:H_2]/[Si:H][Si:H_2]$ ratio in MIR-IR. However, at higher hydrogen dilution the 275^oC substrate temperature *a*-Si:H(B) films can become as organized as *a*-Si:H(B) films made at 365^oC Substrate temperature. This is due to the fact that at lower substrate temperature (275^oC), hydrogen dilution has an increased effect on organization due to less hydrogen dissociation.[3] Lowering the substrate temperature has additional benefits to industry by lowering processing costs and allowing additional substrates, like flexible plastics, to choose from. MIR-IR can use this $[Si:H_2]/[Si:H][Si:H_2]$ ratio and intensity of *a*-Si:H(B) peaks to fine tune *a*- Si:H(B) films by increasing substrate temperature, hydrogen dilution or decreasing boron concentration to receive a more ordered *a*-Si:H(B) film.

5.1.2 Cu/Al Bimetallic Interface Corrosion

To further study the impact of copper on aluminum corrosion, a bimetallic aluminum-copper interface was prepared by sputtering copper microdots on aluminum substrate. Our research aims to utilize immersion corrosion screening metrology as an in situ characterization tool to establish the Al corrosion mechanism and explore prevention strategies directly relevant to Cu wire bonded devices. With additional insights obtained from Tafel plot, scanning electron

microscopy (SEM), electron dispersive X-ray (EDX) and X-ray photoelectron spectroscopy (XPS), a detailed corrosion mechanism at Al/Cu interface can be established. The main achievement of this research is for the first time H_2 evolution was identified as the key cathodic reaction to accompany the active Al corrosion mechanism, Cu/Al bimetallic interface corrosion mechanism, and an organic inhibitor that greatly reduces the corrosion rate on Cu wire to Al pad devices.[5]

The Cu/Al bimetallic interface corrosion mechanism is as follows; In aqueous solution, aluminum oxide reacts with water to form aluminum hydroxide. Chloride ion then replaces the hydroxide to make aluminum chloride, which leads to a dissolution of the passivating oxide because aluminum chloride has very high solubility in water (46g/ 100mL).[6,7] Hydrolysis of aluminum chloride generates protons that eventually produce hydrogen gas. This hydrogen evolution can cause physical stress on the surface and cause a "volcano explosion" like damage. The H_2 gas leaves the system, which prevents the reaction from reaching equilibrium. Thus, the reaction is not self-limiting. Another byproduct of $AlCl_3$ hydrolysis reaction is an increase in acidity. This increase in acidity will attract the negatively charged Cl^- ions, which will increase the corrosion rate in that area. As the corrosion penetrates the Al surface by Cl^- weakening the top $Al(OH)_3$ layer the Al underneath is converted to $Al(OH)_3$ by the oxygen and moisture in the system. The reaction of Al undergoing oxidization is increased by the reaction barrier being decreased by electrochemical cell formed between Cu and Al interface. The Al is giving up its electrons to Cu and the Al is being oxidize in the redox reaction process. This volume expansion from Al to $Al(OH)_3$ is what causes the cracks both vertically and horizontally, allowing easier access to Cl^- and moisture to pristine Al.[8] The pitting or surface roughness is the Cl^- ions attacking the $Al(OH)_3$. The dendrite formation is the cracking starting to form due to the Cl^- weakening the

top $Al(OH)_3$, and the corrosion is starting to penetrate the Al film. Mature mud crack is due to the deep penetration which caused a large set of cracks that is easily detectable by 50x magnification microscope. The Cu/Al bimetallic corrosion is thermodynamically favorable due to the energy of the system, aka the large standard reduction potential difference between Cu and Al. This reaction is enthalpy negative due to exothermic process and is entropy positive due to solid film turning into debris and hydrogen leaving a solid/liquid and leaving the system.

The two key points in the corrosion mechanism proposed is the hydrogen evolution and the transfer of electrons from Al to Cu via redox reaction. A heterocycle based inhibitor that connects with Cu via a -N, -O, -S covalent bond has been proposed to inhibit Ru/Cu bimetallic corrosion.[9] An effective corrosion inhibitor should covalently anchor via -N, -O, -S on Cu/Al surface and also establish strong adhesion by π-π or H-bonding with mold compounds. Such inhibitors were studied via immersion screening. The inhibitors are dissolved 0.1% into the acidic chloride solutions. One such inhibitor worked well in the Cu/Al bimetallic interface in acidic chloride environment. Benzotrizole (BTA) connects to Cu via a nitrogen covalent bond in an acidic environment. Whereas pyrazole works well in binding to Cu in basic solutions, BTA binds well to Cu in acidic environments.[9] Due to BTA being able to covalently bond to the Cu metal, BTA greatly raises over-potential barrier of H^+/H_2 cathodic reaction to passivate the overall Al corrosion, thus, decreasing the corrosion rate.

The Cu/Al bimetallic corrosion project brought the first published data on hydrogen evolution and the Cu/Al bimetallic interface as the main two components to the corrosion mechanism. The Cu/Al bimetallic corrosion mechanism narrowed down which inhibitors to test and displayed that BTA significantly reduced the corrosion rate. The Cu/Al bimetallic corrosion project is continuing by testing fluoride induced corrosion, other metals, and other inhibitors.

5.2 Proposed Future Studies

5.2.1 Deposition of Amorphous Silicon via Hot-Wire Chemical Vapor Deposition (HWCVD)

The effects of substrate temperature, hydrogen dilution and boron concentration on hydrogen dilution and boron doping in *a*-Si:H thin films deposited by plasma enhanced chemical vapor deposition (PECVD) by chemical bonding characterization studies with a FTIR spectrometer has already been successfully studied.[1] The study is twofold: we will use our experience in *a*-Si:H films to study the effects of substrate temperature on *a*-Si:H thin films grown via hot wire chemical vapor deposition (HWCVD) and compare *a*-Si:H films deposited by PECVD vs. HWCVD. Chemical bonding characterization studies with a FTIR spectrometer will be the main analytical tool analyzing the samples in this research.

The focus of the study of *a*-Si:H includes its application with infrared cameras, also known as microbolometers. Currently, PECVD is the industry standard for *a*-Si:H thin film preparation. The HWCVD method is gaining attention mainly due to the several advantages it has over PECVD. HWCVD has extra variables to better fine-tune the *a*-Si:H thin films. Such variables include temperature, oscillating movement, and chemical element of the hot wire. Another advantage of HWCVD is that the hot wire technique produces fewer defects than PECVD as ion bombardment is not a problem in HWCVD.[10,11] The HWCVD method uses thermal energy to catalytically decompose silane while PECVD uses electrical energy with ion bombardment to deposit silane. For PECVD, the plasma surface interactions involve atoms and molecular fragments such as radicals, ions and energetic photons. Electron energies in the plasma have a Maxellian distribution in the 0.1-20 eV range. These energies are sufficiently high enough to excite molecules or break

chemical bonds at the depositing film. Radiative recombination occurs also a problem with films being deposited via PECVD. Radiative recombination is when a free electron combines with a radical atom and emits a photon. For example, $e^- + Ar^+ \rightarrow Ar + h\upsilon$[12], the photon from argon has an energy of 9.3 eV which is enough energy to break chemical bonds in the depositing film.[13] This chemical bond breakage due to ion bombardment and radiative recombination increases defects within the depositing films and needs to be avoided. Instead of ion bombardment, HWCVD has small voltages present in the deposition chamber and any ions produced in the HWCVD chamber, do not reside in the chamber long enough to become sources of particle formation. When an alternating current (AC) voltage is used to resistively heat the filament for HWCVD, any ions that may be produced are swept to the filament ends as well as the chamber walls due to the 60 Hz voltage oscillation.[14]

A HWCVD system includes a vacuum tight chamber, tungsten wire, electronic feed through, gas inlet valve, heater to heat up the substrate, and a thermocouple and vacuum system to make *a*-Si:H thin films, Figure 5.1 (A).[15] The HWCVD method uses thermal energy via the hot metal wire to catalytically decompose silane and hydrogen molecules. Tungsten, tantalum, rhenium, molybdenum and also graphite have been used as filament material. Coiled tungsten wire is most commonly used due to film quality, price, and availability. The hottest region is near the tungsten filament where the filament is heated to 1900K to 2300K.[10] In Figure 5.1, (B) T_1 is a white line to show the tungsten wire is the hottest location of the HWCVD chamber and T_2 represents substrate temperature. During catalytic decomposition, SiH_4 is dissociated into Si and H radical species by the hot filament. These radical species react with each other to produce SiH_3, SiH_2, Si_2H_2, Si and H fragments. These radicals either further react with other gas phase species for film deposition or deposit on the substrate.[10,16]

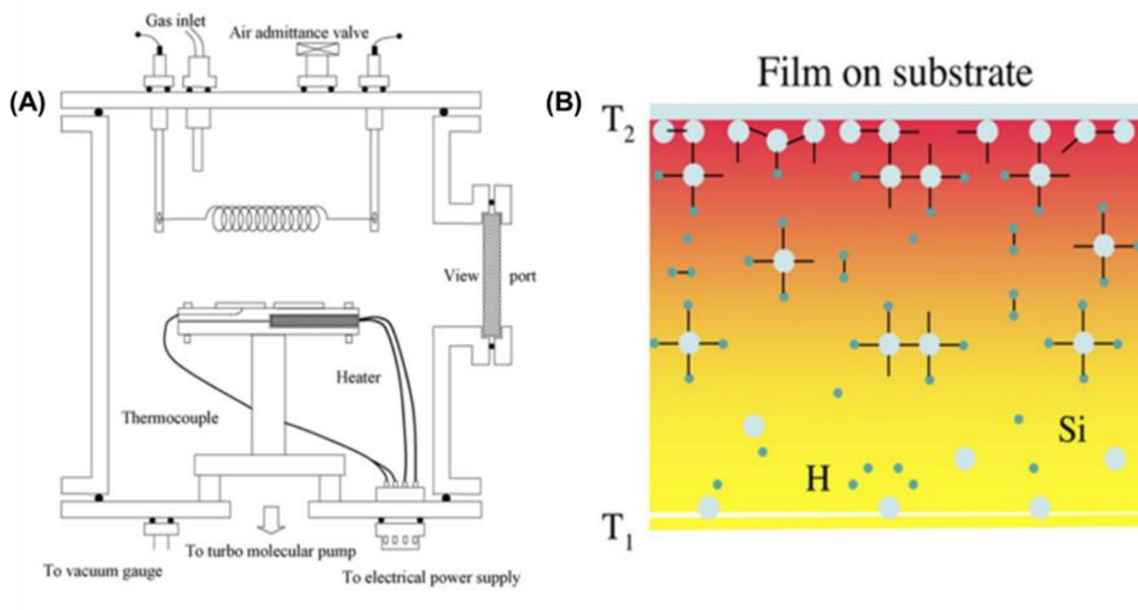

Figure 5.1: (A) Hot-wire Chemical Vapor Deposition (HWCVD) system.[17] (B) Visual representation of silane and hydrogen molecules being catalyzed by a tungsten wire and then depositing on a film substrate.[10]

This research will provide information about *a*-Si:H grown by HWCVD at low temperatures for the goal of more sensitive microbolometers. The outcome of this investigation will provide the military of the United States of America with an invaluable insight of the temperature effect of *a*-Si:H as well as guidance for integration in infrared cameras. Amorphous silicon thin film layers are the backbone of many large area applications such as flexible electronics, microelectromechanical systems (MEMS), solar cells and microbolometers. The knowledge of the chemical properties acquired in this work will support the design and fabrication of more reliable devices in the future. This complete set of chemical properties studied in a comprehensive set of *a*-Si:H thin films opens a path to future studies of the chemical, material, and electrical properties in these structurally complex materials. This research will aid in the

process development of infrared cameras, providing chemical information for future studies and also provide research and education opportunities for students.

5.2.2 Cu-Al Alloy Corrosion Proposed Study

In chapter 4, a Cu ball attached to an Al pad device corrosion mechanism was identified and an organic inhibitor was discovered to significantly reduce the corrosion rate. The Cu-Al bimetallic corrosion research project through Freescale was completed in 2015; however, the Cu-Al bimetallic interface corrosion research project is currently ongoing through a research grant with Texas Instruments (TI) in 2016. Testing other halide ions (F^-) other metals (Au, Ru, Ta, and Pd), other inhibitors that are derivatives of pyrazol, concentration of inhibitors, and testing devices made by TI will be the main points of focus for the continuation of research in this area.

Another area to look into further is a personal proposal to study the Cu to Al percentage on the Al pad. Current and past samples have 0.5% Cu by weight due to electromigration.[18] This 0.5% Cu by weight percentage is for electromigration, but it may not be the optimum percentage for corrosion resistance. For example, in Figure 5.2(A) there is an Al substrate with 0.5% Cu and Figure 5.2(B) has a pure Al substrate. Figure 5.2(A&B) show an increase in corrosion rate for the sample with the pure Al substrate. Figure 5.2(C&D) show there is a larger initial current (μA) for the Cu dot on pure Al substrate versus Cu dot on Al (0.5% Cu by weight) substrate. This is likely due to the difference in standard reduction potential, which is reduced when the Al is mixed with a low percentage of Cu, thus making the Al substrate have a closer standard reduction potential to Cu. It has been mentioned that a 9:4 ratio of Cu to Al is the percentage most likely to undergo corrosion, and 1:2 ratio of Cu to Al is the least likely to undergo corrosion while comparing 9:4,

1:1, 2:3 and 2:1 Cu to Al ratios.[19,20] Information about lower Cu concentration by weight with Al in acidic chloride environments was missing. This can be looked into further by studying Cu-Al alloys via micropattern immersion corrosion screening metrology shown in chapter 4. Cu-Al ratios 9:4, 1:1, 2:3 and 2:1 as well as ratios with lower percentage (close to 0.5% Cu) should be looked into further with the micropattern immersion corrosion screening metrology.

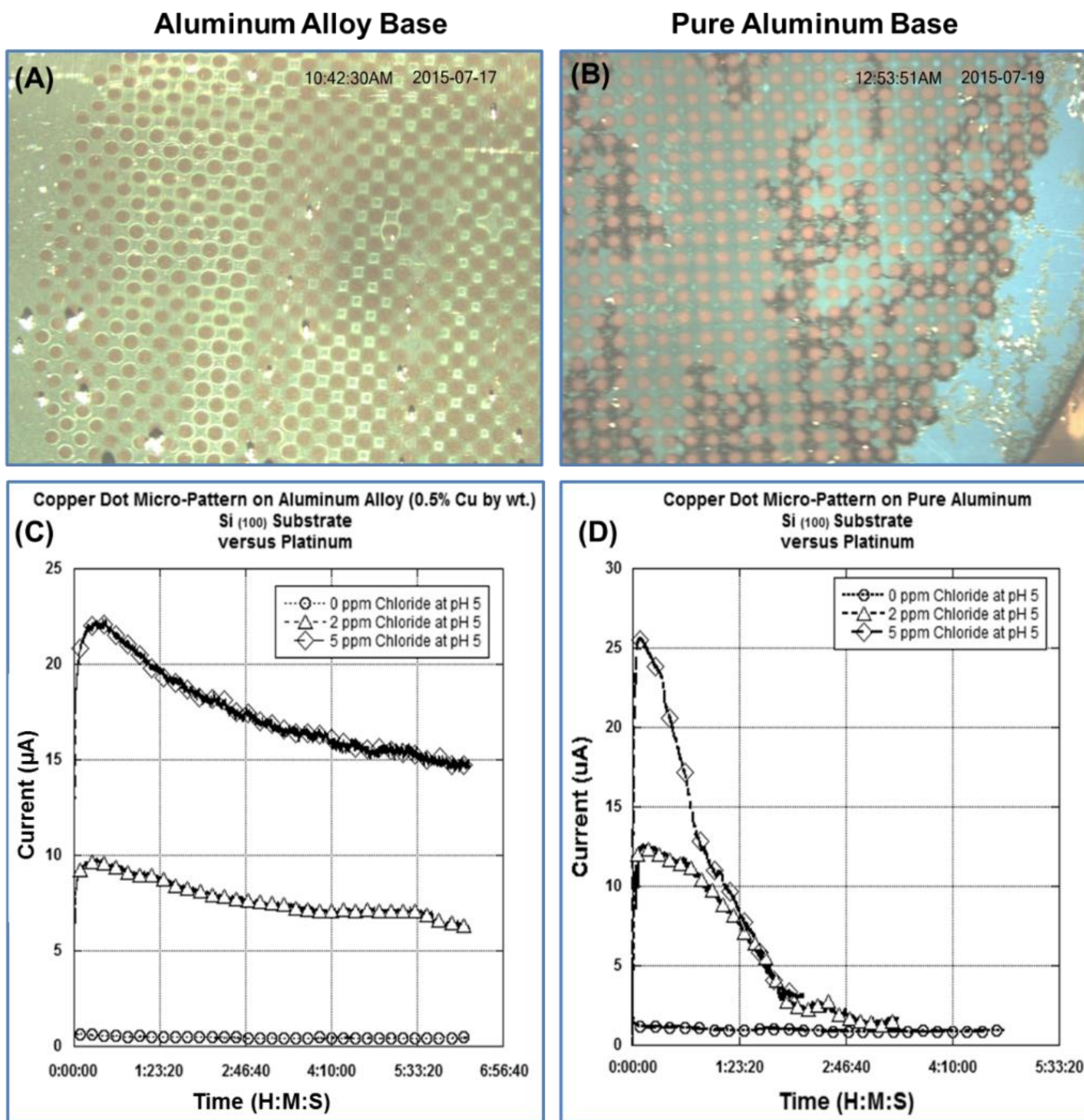

Figure 5.2 (A&B) Images via Powerscope imaging of electrodes after 24 minutes of immersion in 5 ppm chloride at 5pH solution. (A) Micropatterned copper on aluminum alloy base metal and (B) micropatterned copper on pure aluminum. (C) Micropatterned copper on aluminum with 0.5% copper electrodes versus platinum. (D) Micropatterned copper on pure aluminum electrodes versus platinum.

Preliminary research has already been done in this area. Calibration of the physical vapor deposition (PVD) sputtering system has been done to get the proper Cu to Al ratios, Figure 5.3(A-C). The PVD sputtering system will first deposit the desired Cu to Al ratio and then sputter Cu

dots on top of the Cu-Al alloy substrate. This PVD sputtering system coupled with the micropattern immersion corrosion screening metrology is a time and cost effective way to screen for corrosion resistance.

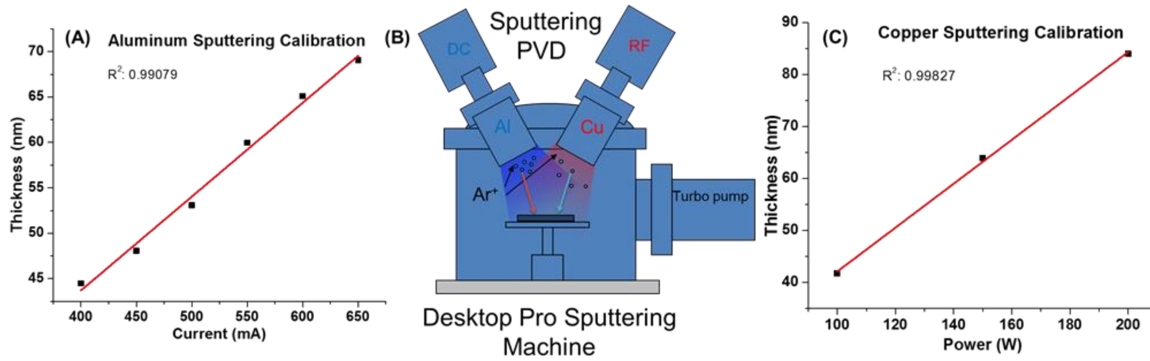

Figure 5.3 (A) Calibration of aluminum thickness (nm) versus current supplied to the direct current target. (B) Physical vapor deposition process used to sputter thin films of metals. (C) Calibration of copper thickness (nm) versus power (W) supplied to the radio frequency target.

The preliminary research has shown that there is a difference in corrosion rate depending on the Cu-Al ratio; however, further work and calibration needs to be done to confirm proper adhesion layer. For example, a titanium, tantalum or some other adhesion layer needs to be placed in between the silicon substrate and the Cu-Al alloy layer. Further calibration needs to be done to discover the proper way to obtain low Cu percentage in the Al. These could possibly be done by sputtering thin Cu dots on an Al substrate then heating the sample to create an alloy. This research proposal could increase corrosion resistance of Cu wire Al pad devices by making a more corrosion resistant Al pad.

5.3 References

1. Ross, N.; Shrestha, K.; Chyan, O.; Littler, C. L.; Lopes, V. C.; Syllaios, A. J. Characterization of Boron Doped Amorphous Silicon Films by Multiple Internal Reflection Infrared Spectroscopy. *MRS Online Proceedings Library* **2013***, 1536*, 127-132.

2. Rimal, S.; Ross, N.; Pillai, K. S.; Singh, K. J.; Chyan, O. Characterization of Post Etch Residues on Patterned Porous Low-k Using Multiple Internal Reflection Infrared Spectroscopy. *ECS* **2011***, 41*, 315-322.

3. Shrestha, K.; Lopes, V. C.; Syllaios, A. J.; Littler, C. L. Raman spectroscopic investigation of boron doped hydrogenated amorphous silicon thin films. *J. Non Cryst. Solids* **2014***, 403*, 80-83.

4. Collins, R. W.; Ferlauto, A. S.; Ferreira, G. M.; Chen, C.; Koh, J.; Koval, R. J.; Lee, Y.; Pearce, J. M.; Wronski, C. R. Evolution of microstructure and phase in amorphous, protocrystalline, and microcrystalline silicon studied by real time spectroscopic ellipsometry. *Solar Energy Mater. Solar Cells* **2003***, 78*, 143-180.

5. Ross, N.; Goswami, A.; Berhe, S.; Lin, P.; Chyan, O. Study of Bimetallic Corrosion and Its Inhibition Strategy for Cu Interconnect and IC Packaging Using Micro-Pattern Corrosion Screening. *SRC Techcon* **2015**.

6. Wang, B.; Tang, L.; Qi, J.; Wang, J. Effects of Pulse Electromagnetic Field on Corrosion Resistance of Al-5 % Cu Alloy. *J. Low Temp. Phys.* **2013***, 170*, 418-423.

7. Mol, J.; Hinton, B.; Weijde, D.; Wit, J.; Zwaag, S. A filiform corrosion and potentiodynamic polarisation study of some aluminium alloys. *J. Mater. Sci.* **2000***, 35*, 1629.

8. Vrublevsky, I.; Parkoun, V.; Sokol, V.; Schreckenbach, J.; Marx, G. The study of the volume expansion of aluminum during porous oxide formation at galvanostatic regime. *Appl. Surf. Sci.* **2004***, 222*, 215-225.

9. Goswami, A.; Koskey, S.; Mukherjee, T.; Chyan, O. Study of Pyrazole as Copper Corrosion Inhibitor in Alkaline Post Chemical Mechanical Polishing Cleaning Solution. *ECS Journal of Solid State Science and Technology* **2014***, 3*, P293-P297.

10. Zheng, W.; Gallagher, A. *Thin Solid Films* **2006***, 501*, 21.

11. Mahan, A. H. *Solar Energy Materials and Solar Cells* **2003***, 78*, 299-327.

12. Ahrenkiel, S. P.; Mahan, A. H.; Ginley, D. S.; Xu, Y. Solid-Phase Crystallization Kinetics and Grain Structure During Thermal Annealing of a-Si:H Grown by Chemical Vapor Deposition. **2001***, 176*, 972-977.

13. Xu, Y.; Nelson, B. P.; Gedvilas, L. M. Improving Narrow Bandgap a-SiGe:H Alloys Grown by Hot-Wire Chemical Vapor Deposition. *Thin Solid Films* **2003***, 430*, 197-201.

14. Schropp, B.; Stannowski, A. M.; Brockhoff, P. A. T. T.; Rath, J. K. Hot-Wire CVD of Heterogeneous and Polycrystalline Silicon Semiconducting Thin Fims for Application in Thin Film Transistors and Solar Cells. *Matter. Phys. Mech* **2000**, *1*, 73-82.

15. Wang, Q. Hot-wire CVD Amorphous Si Materials for Solar Cell Application. *Thin Solid Films* **2009**, *517*, 3570-3574.

16. Gogoi, P.; Jha, H. S.; Agarwal, P. Effect of Silane flow rate on microstructure of Silicon films deposited by HWCVD. *J. Non Cryst. Solids* **2012**, *358*, 1990-1994.

17. Chonga, S. K.; Goha, B. T.; Aspanuta, Z.; Muhamada, M. R. Effect of substrate temperature on gold-catalyzed silicon nanostructures growth by hot-wire chemical vapor deposition (HWCVD) . *Appl. Surf. Sci.* **2011**, *257*, 3320-3324.

18. Lienig, J. Introduction to Electromigration-Aware Physical Design. *ISPD* **2006**, 39-46.

19. Uno, T. Bond reliability under humid environment for coated copper wire and bare copper wire. *Microelectronics Reliability* **2011**, *51*, 148-156.

20. Zeng, Y.; Bai, K.; Jin, H. Thermodynamic study on the corrosion mechanism of copper wire bonding. *Microelectronics Reliability* **2013**, *53*, 985-1001.